TUNGSTEN OXIDE NANOSTRUCTURES AND THIN FILMS FOR OPTICAL GAS SENSORS

Muhammad Usman Qadri

Dipòsit Legal: T 1233-2014

DOCTORAL THESIS

Muhammad Usman Qadri

Tungsten oxide nanostructures and thin films for optical gas sensors

UNIVERSITAT ROVIRA I VIRGILI

Tarragona

2014

Muhammad Usman Qadri

Tungsten oxide nanostructures and thin films for optical gas sensors

DOCTORAL THESIS

Supervised by Prof. Eduard Llobet Valero, Dr. Maria Cinta Pujol and Dr. Josep Ferre Borrull

Department of Electronic, Electrical & Automatic Control Engineering

UNIVERSITAT ROVIRA I VIRGILI

Tarragona

2014

UNIVERSITAT ROVIRA I VIRGILI

Departament d'Enginyeria Electrònica,

Elèctrica i Automàtica

Av. Països Catalans, 26

43007 Tarragona

Tel. 977 559610

Tel. 977 559728

WE STATE that the present study entitled "Tungsten oxide nanostructures and thin films for optical gas sensors", presented by Muhammad Usman Qadri for the award of the degree of Doctor, has been carried out under our supervision at the Department of Electronic, Electric and Automatic Control Engineering of this university, and that it fulfills all the requirements to be elegible for the European Doctorate Award.

Tarragona, 5 June 2014

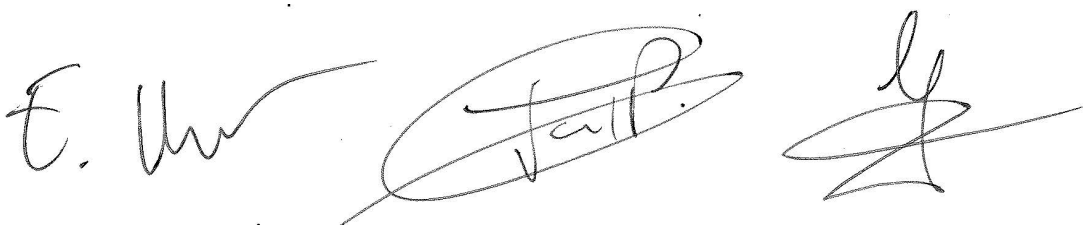

Doctoral Thesis Supervisors

Maria Cinta Pujol Bages
Eduard Llobet Valero
Josep Ferré i Borrull

Acknowledgments

First of all, I would like to thank ALLAH ALMIGHTY because without ALLAH's will this doctoral thesis would not have been possible at all.

I would like to express my sincere gratitude to the management of EMaS and the research goups MiNoS, NePhoS and FiCMA of Universitat Rovira I Virgili (URV) for giving me the opportunity to join as a doctoral student and providing necessary infrastructure and resources to accomplish my doctoral work. I am as much as thankfull to URV and Generalitat de Catalunya for giving me the doctoral scholarship during my study here.

I would like to show my gratitude to my supervisors Prof. Eduard Llobet, Maria Cinta Pujol and Josep Fere Borrul for introducing me to this project work and for their endless and kind support throughout this doctoral work. Especially, I would like to say my special regards to Dra. Maria Cinta Pujol. Without her moral, technical and educational support throughout the project I might not have been able to finish this doctoral work. Whenever I was stuck, she helped and guided me with patience. She is not only a good supervisor but a very good colleague as well. May God bless her and her family.

I also want to thank the other senior members of the FiCMA-FiCNA group: Dr. Joan Carvajal, Dr. Xavier Mateos, Dr. Jaume Massons, and Dr. Rosa Solé and for their support during my stay in this research group. Especially, to Prof. Dr. Francesc Diaz and Prof. Dr. Magdalena Aguiló.

I would like to thank the support of technician staff in FiCMA-FiCNA lab: to Agustí Montero, Nicolette van der Bakker and especially to Laura Escorihuela for her friendship and willingness of support my work during these years. Also, Raul Calavia the tehcnician from MiNoS group for helping me in the gas sening setup and measurements. I would like to say my specail thanks to Tony Stoycheva and Fatima Annanouch for their support in the grwoth of nanoneedles. I thank all the people in In Servei de Recursos Cientìfics i Tècnics at Rovira i Virgili University,

I would like to thank all my FiCMA-FiCNA colleagues. We started out as lab mates and along the way became friends sharing lunches, coffees, birthdays, etc.: Isabel Parreu, Montserrat Galceran, Western Bolaños, Venkatesan Jambunathan, Martha Segura, Raj Kumar, Maria Méndez, Jaume Cugat, William Barrera, Oleksandr Bilosouv, Muhammad Ali Butt, Carla Berrospe, Oleksandr Savchuk, Elena Perez, Mina Moeini,

Airan Rodenas, José Maria Serres, Marc Medina, Josué Mena, Javier Martinez, Eric Pedrol, Mark Isan, Christy, Irene and Josep Maria Serres.

I am grateful to Prof. Alessandro Martucci for the privilege of work in the Dipartimento di Ingegneria Industriale at University of Padova. I thank all the members in the research group of Prof. Martucci in the department of idustrial engineering. Especially, Alex diaz, Michaela Cittadini in helping and introducing me to the gas sensing measurements in their laboratory. Also, Marco Beresani, Laura Brigo and Mauro for the chats during lunch and drinks after the university.

Last, I would like to pay my gratitude to my beloved family my father, Haji Azam Hussain and mother, Shaista bano for all their moral and financial support and to my brother, Muhammad Umer Qadri dear sisters nephews nieces my wife and son, Ghazzali, for loving and missing me especially, those whom I can not see now, just left with their memories. Love you all!

DEDICATED TO ALL MY FAMILY

MY DEAR FATHER HAJJI. AZAM HUSSAIN

&

DEAR MOTHER SHAISTA BANO

MY WIFE
&
SON

Abstract

In this doctoral thesis, WO_3 based thin films and nanostructures have been investigated for optical gas sensing. Three different methods have been implemented namely RF magnetron sputtering, Aerosol assisted chemical vapor deposition (AACVD) and sol – gel modified pechini method for fabricating them. The nano structured material synthesis, device fabrication and their gas sensing properties have been studied.

Thin films of tungsten trioxide, were deposited on quartz substrates by RF magnetron sputtering. Different annealing temperatures in the range from 423 to 973 K were used under ambient atmosphere. The influence of the annealing temperature on the structure and optical properties of the WO_3 thin films was studied. The surface morphology of the films was composed by grains with an average size near 70 nm for the films annealed between 773 and 973 K. Some of the WO_3 thin films were also doped with Pt nanoparticles (NPs) of about 45 nm in size. Spectrometric measurements of transmittance were carried out for undoped WO_3 in the wavelength range from 200 - 900 nm, to determine the effect of the exposure to three different gases namely H_2, CO, and NO_x. Films typically showed fast response and recovery times, in the range of few seconds.

WO_3 nanoneedles have been grown using AACVD. These films were functionalized with Au and Pt NPs using AACVD method the co-deposition of NPs is done in single step along with WO_3. This co-deposition method is demonstrated to be an effective route to incorporate metal NPs or combinations of metal NPs into nanostructured materials, resulting in an attractive way of tuning functionality in WO_3. These nanoneedles were subjected to optical gas sensing test under the effect of NH_3 gas. The films functionalized with Au and Pt showed a reversible change at room temperature. The results of optical gas sensing at room temperature are the first time reported for the WO_3 nanoneedles.

Monoclinic WO_3 nanocrystalline powder was obtained by a simple route of modified Pechini method. DTA and X-ray measurements were used to refine the appropriate calcination temperature. The precursor powder was calcinated at 873 K during 1h till 3h. The size particle and dispersion has been analyzed by electron microscopy, obtaining an average size of the crystallite around 18.58 nm. The active surface area

has been quantified by BET analysis being 8.643 m^2/g. Optical properties of these nanocrystals have been investigated using photoluminescence measurements.

Structural characterization techniques were employed to extract important information of gas sensitive films such as their morphology, chemical composition, crystal structure and orientation. This information helped to better understand the nature of nanostructured material growth and link its characteristics to their gas sensing properties. The results obtained in this doctoral work suggests the possibility of developing a device for detecting multiple gases employing nanotextured WO_3 thin films or nanostructures working on the principles of optics and photonics.

List of Publications

This doctoral work has also resulted in 3 publications and 4th is in preparation listed below.

Paper 1. WO_3 nano-needles by Aerosol Assisted CVD for optical sensing,Muhammad U.Qadri, Toni Stoycheva, Maria Cinta Pujol, Eduard Llobet, Xavier Correig, Josep Ferre Borull, Magdalena Aguiló and Francesc Díaz, Proc. Eurosensors XXV, September 4-7, 2011, Athens, Greece, Procedia Engineering 25 (2011) 761 – 764.

Paper 2. WO_3 thin films for optical gas sensing, Muhammad U. Qadri, Maria Cinta Pujol, Josep Ferré-Borrull, Eduar Llobet, Magdalena Aguiló and Francesc Díaz, Proc. Eurosensors XXV, September 4-7, 2011, Athens, Greece,Procedia Engineering 25 (2011) 260 – 263.

Paper 3. Effect of Pt Nanoparticles on the Optical Gas Sensing Properties of WO_3 Thin Films, Muhammad U. Qadri, A. Diaz Diaz, M. Cittadini, A. Martucci, Maria Cinta Pujol, Josep Ferré-Borrull, Eduard Llobet, Magdalena Aguiló and Francesc Díaz, Sensors 2014, 14(7), 11427-11443; doi:10.3390/s140711427.

Paper 4. Pt-AU/ WO_3 nano-needles by Aerosol Assisted CVD fro optical gas sensing of NH_3, Muhammad U.Qadri,, Fatima Ezahra Annanouch, Maria Cinta Pujol, Eduard Llobet, Xavier Correig, Josep Ferre Borull, Magdalena Aguiló and Francesc Díaz, in preparation.

Table of Contents

CHAPTER 1

INTRODUCTION

1 Introduction

1.1 Need of gas sensors

The ever increasing progress of technology for the human needs, have benefited humanity in all the fields. This progress, which has benefits, also involves serious issues related to our environment. All the industry somehow influences our environment. From the industrial solid waste to the emission of different toxic gases such as CO, H_2, Benzene, NH_3, NO_x and sulfur compounds released from industries and also from automobiles like H_2S, have been polluting our air. Neglecting the facts related to environmental issues is causing serious problems. Exposure of these hazardous gases to human body causes different diseases, shortness of breath, nausea, swelling of tissues in the throat, immunity system and in the worst case death. Another key topic associated to sensors is related to the so called comfort applications, for example in air monitoring inside buildings or cars, where the target gas may not be highly hazardous or toxic, but its detection and elimination from the environment can improve the air quality. There is an urgent need to find the solutions that comply with the requirements needed to the environmental security.

Ability to detect these above mentioned gases in industry and homeland security is important. Recent developments in sensing technology have provided simple yet efficient way to deal with these environmental issues. It is easy to understand that highly sensitive and possibly selective devices are mandatory for these applications; moreover an ideal sensor should also be as much miniaturized as possible, stable in a wide range of temperatures and environments, cheap, user-friendly, long-lasting and it should also allow in situ measurements with the operator being at safety distance from the hazardous source.

A device able to convert a target chemical or physical variation to be monitored into an easily processable signal can be defined as a sensor, the sensing element has to fulfill essentially two different tasks: first, it has to interact with the target gas through various mechanisms like surface adsorption, charge transfer, ionic exchange (receptor task); then this interaction has to be transformed into an easily processable signal, like for example a change in electrical conductivity or in optical transmission (transducer task). A lot of research and development is done to design small and affordable gas sensors which possess high sensitivity, selectivity and stability with respect to a given application. This search comes along with a large variety of sensors based on different

sensing principles, e.g. semiconductor gas sensors, optical sensors, thermal conductivity sensors, mass sensitive devices like quartz microbalance sensors, catalytic sensors, dielectric sensors, electrochemical sensors and electrolyte sensors.

The sensing phenomena in all these devices rely on different chemical and physical changes such as:

- changes in electrical properties (conductivity, impedance, capacitance)
- optical properties (absorption, reflection, luminescence, refractive index)
- physical properties (mass, thermal conductivity, acoustic waves propagation)
- measuring the reaction heat
- analyzing specific electrochemical or biochemical recognition.

1.2 An overview on conductometric gas sensors

The first and at the moment more established sensors are based on a conductometric interface. The gas detection is through change of electric conductivity of an active material. These type of devices, without any doubt have been the most intensly studied in the last two decades. The active material is comonly based on semiconductor metal oxides. These type of devices consist mostly of three components:

- the active material;
- a heating system;
- electrodes for signal transmission.

The use of semiconductors as sensors for gases dates back to 1952, when Brattain and Bardeen first reported gas sensitive effect on bulk Germanium [Brattain 1952]. Later, metal oxides were used as gas sensing material by Seiyama [Seiyama 1962]. The bulk semiconductors sensors based on metal oxides was developed on industrial scale for the first time by Taguchi [Taguchi 1970, Taguchi 1972]. Since then, different types of metal oxides were investigated and identified to be sensitive towards different gases. It is commonly known that these materials can have either n- or p-type of conductivity [Korotcenkov 2007]. These materials donate and accept negative charges when exposed to oxidizing and reducing gases, respectively. This translates into an increase (decrease) in resistance of the devices that employ n-type materials when exposed to oxidizing (reducing) gases. In contrast, their p-type counterparts experience a decrease (increase) of resistance when exposed to these similar gases.

Metal-oxide (MOX) based gas sensors have been studied over the last few decades extensively, they show good properties in a number of ways:

- highly sensitive
- easy to be included in a measuring system
- cost-effective and respond to a wide spectrum of oxidizing and reducing gases
- possibility of low cost production on industrial scale.

Like general semiconductors, MOX layers can be n – or - p type if their main charge carriers are electrons or holes, respectively. The functionality of the MOX layers is oxidation / reduction reactions of the target gas that adsorbs on its surface. For example, when an oxidising gas reaches the surface of an n-type active material, it chemisorbs and takes electrons from the conduction band. A depletion layer is formed by the adsorption of these negatively charged ions on the surface and the free electrons are confined in the center of MOX grains. In such a way, the resistance of the MOX layer increases in the presence of oxygen. Simmilarly, in the presence of a reducing gas, the gas atoms react with oxygen adsorbed at the surface of MOX. So that, the concentration of the adsorbed oxygen is reduced and accordingly, width of depletion the layer is reduced and hence, the resistance decreases. In short, we can consider that upon oxygen adsorption, at the grain boundaries a shottky barrier develops. The height of the barrier depends on the amount of oxygen absorbed species (it inceases or decreases with the number of oxygen ions).

Table 1.1 Known semiconductor metal oxide based conductomeric gas sensors [Korotcenkov 2007]

Metal oxides	Gas optima for detection	Operating temperatures [K]
SnO_2	Reducing gases (CO, H_2, CH_4, etc)	473 – 673
WO_3	O_3, NO_x, H_2S, SO_2	573 – 773
Ga_2O_3	O_2, CO	873 - 1173
In_2O_3	O_3, NO_x	473 - 673
MoO_3	NH_3, NO_2	473 - 723
TiO_2	O_2, CO, SO_2	623 - 1073
ZnO	CH_4, C_4H_{10}, O_3, NO_x	523 - 623
CTO	H_2S, NH_3, CO, VOC	573 - 723
Fe_2O_3	Alcohol, CH_4, NO_2	523 - 723

In table 1.1 some of the well known metal oxide semiconductors with good gas sensing properties are shown with their operating temperatures with the main gases they can detect. In table 1.1 we can see that for all these materials their operating temperatures are above 473 K. The advantage of having high operating temperatures is that it allows the use of the sensors in harsh environments such as car engines and machines. There are some limitations associated with these sensors, such as the fact that their poor selectivity (they cannot be made specific for the detection of a given target species) and long-time stability (they generally show some baseline and response drift associated to poisoning).

A detailed description of all the conductometric devices is not the purpose of this thesis, and so only a brief overview of the sensing material is presented.

1.3 An overview on optical gas sensors

Optical gas sensors are refered to as the devices that detect target gas by the change in the optical properties of the active material. The development of such devices is relatively new. The idea behind is, to take advantage of the reduced cost in optical components driven by the large commercial telecommunication and optoelectronic markets. Which creates opportunities in the implementation of the technology for sensing applications. Optical signals have many advantages over electrical signals (e.g. immunity to electrical interferences and noise) thus it offers vast opportunity to the researchers to explore its potential in the sensing applications. The advantages of optical devices over conventional electricity-based gas sensors are as follows [Yang 2002, Zhuang 2005] :

- high immunity to electromagnetic noise
- fire resistance
- inactivity in flammable environments
- capability of remote sensing and information transfer through optical fibers network.

Furthermore new potential applications in multi-gas detection can be achieved using differences in the intensity, wavelength, phase and polarization of the output light

signal. The other advantage of optical sensors is their higher selectivity as compared to conductometric sensors. The development of optical sensor is perhaps limited by the availability of materials with chromic properties.

At the beginning, it was assumed that the metal oxides used as conductometric sensors could be used as sensing material in optical sensors too. However, when the nature of the interaction between gas molecules and the sensing layer became increasingly well understood, the deployment of different metal oxides for different gas sensing applications neede to explored and confirmed. So, metal oxides with excellent conductivity response towards certain gases do not necessarily show the same performance in their optical response [Korotcenkov 2007, Deb 1992].

The sensing performance of metal oxide gas sensors is based on some independent factors such as material properties, variability of sensor construction and transducer function. The ability of the metal oxide surface to interact with gas depends on its material properties and the transducer function provides the ability to convert the signal caused by the chemical interaction of the metal oxide surface into a reliable (electrical or optical) signal [Yamazoe 2005]. The surface of the sensing material is responsible for receptor function of the gas sensor, the enhancement of the surface properties by depositing nanostructured metal oxides should considerably improve the sensor's performances. In the nanometer scales, surface to atom ratio is dramatically increased, which increases the effective number of sites available for reactions with target molecules. Based on the available information and knowledge, this Phd work is based on WO_3 nanostructures for optical gas sensing. A detailed overview of WO_3 will be provided in the next section.

An optical sensor based on WO_3 thin films sensitive towards H_2 was first published in 1984 by Ito and coworkers [Ito 1992]. It was an optical fiber coated with metal oxide film sensitive towards H_2 or hydrogen containing gases Like NH_3. This metal oxide films were combined with a catalytic layer of noble metals, i.e. palladium (Pd) and platinum (Pt). The gas molecules are absorbed on the surface of the metal, this metal acting as a catlyst dissociates the gas into its ions and electrons [Ito 1992]. Further these ions diffuse into the metal oxide layerand as a result the change in its optical properties is observed. The absorbance of the films changed with the increase in the concentration of H_2. The observed response was at 1400 nm wavelength. Based on the results by Ito a variety of optical sensors have been developed. Hamagami and coworkers [Hamagami 1993] reported that their sputtered molybdenum trioxide (MoO_3) films coated with Pd showed a change in transmittance on the exposure to H_2. Pt/ WO_3 was

deposited on the tip of an optical fiber by Sumida et.al [Sumida 2005] and test for H_2 of 1 % and N_2 using time domain optical reflectrometry (OTDR).

Gas sensing can be divided into two main groups, direct techniques which monitor the physical parameter of the target gas and indirect techniques which use chemical reaction in the gas sensitive material to indicate the concentration of the analyte [Goepel 1990]. They are further divided into two domains i.e. electrical and optical. In current works indirect optical spectroscopy techniques by deploying gas sensitive metal oxide layer have been adopted. Using an optical spectroscopy system for sensing is convenient due to its simplicity, low cost, high selectivity and sensitivity with the use of a suitable catalysts [Tabib-Azar 1995]. The main advantages are well established deposition techniques for metal oxide sensitive layer, and measurements can be performed in suitable wavelength ranges (VIS/NIR) using a spectrophotometer or inexpensive optical components such as LEDs, optical fibers as well as silicon photodiodes.

Optical spectroscopy techniques used commonly for gas sensing are based on absorbance/transmittance, reflectance, refractive index, photo or chemi-luminescence and surface plasmon resonance (SPR). In this Phd work, absorbance/ transmittance spectroscopy is used for gas sensing being less complicated and the output signal is directly related to the gas concentration. The optical absorption or transmittance measurements are derived from Beer-Lambart law, this law together with the spectrophotometer used in this thesis are introduced in Chapter 2. In short, the absorbance response of the sensing layer is due to the change of the material electronic states when it interacts with the dissociated gas ions. The gas sensing mechanism in metal oxide nanostructured thin films based on the film's optical response will also be explained in the next section.

1.4 WO_3 gas sensors

The discovery of electro-chromic (EC) effect in transition metal oxides opened a new window for research and development employing such material. WO_3 is a material of high interest in the transition metal oxides not only for EC devices but in many other related applications. Tungsten oxide or tungsten trioxide (WO_3) is a chemical compound which has oxygen and transition metal tungsten. It is found in the form of hydrates in the nature. It has been of great interest during the last few years due to its enormous attractive structural, optical and electrical properties.

The material ability to sustain reversible and persistent changes of its optical properties under the action of a voltage was discovered in 1969 by Deb [Deb 2008]. The coloration of WO_3 from transparent to dark was shown in highly disordered thin films [Deb 2008]. Since then, extensive studies have been carried out for WO_3 in smart window applications. The first reported gas sensor based on WO_3 was presented in 1967 [Shaver 1967]. They demonstrated Pt/ WO_3 gas sensor which, on the exposure of H_2 showed the change in conductivity. Since then, WO_3 has attracted constant research interest due its promise in a wide range of future applications as active material for gas sensing. However, the first reported work of WO_3 as an optical gas sensor was presented in 1992 by ITO and coworkers[Ito 1992]. The gasochromic response of the films towards H_2 by Ito, has been suggested to be analogously similar to the electrochromic phenomenon in WO_3 [Deb 2008]. Recently, WO_3 based thin films loaded with Pt for optical H_2 sensing has been demonstrated by Yaacob et.al. [Yaacob 2009], which proves that WO_3 is an excelent material for gaschromic applications. Therefore, WO_3 has been studied for its optical gas sensing properties in this doctoral thesis. First, we will discuss its chemical and physical properties.

The crystalline phase of WO_3 transforms from monoclinic to triclinic, monoclinic, orthorombic and tetragonal with the change in temperature from < 123 K to 1013 K respectively as shown in table 1.2 [Lassner 1999]. However, the crystal formation at the subzero temperature is very rarely found except in the laboratory and thus, monoclinic crystals normally refers to the ones that exist at room temperature. The monoclinic crystal structure with phase group $P2_1/n$ is the one most commonly found in WO_3. Despite the fact that WO_3 transforms in different crystalline phases it is unable to retain these phases and returns to monoclinic phase at room temperature [Zheng 2011].

WO_3 is a wide bandgap n-type semiconductor with crystals that have perovskite-like atomic configurations based on corner-sharing WO_6 octahedra. In agreement with the behavior of most perovskites, WO_3 single crystals structurally transform depending on the temperature [Zheng 2011].

Table 1.1 The crystal structure of tungsten trioxide depending on temperature [Lassner 1999].

Crystal structure	Temperature [K]	Space group	Lattice constant [Å]	Lattice angles[º]
Tetragonal	< 123	*P4*/nmm-D^7	a=5.272 c=3.920	-
orthorhombic	123 - 290	*P*mnb-D^{16}	a=7.340 b=7.546 c=7.728	-
Monoclinic	290 - 603	$P2_1$/n	a=7.302-7.306 b=7.530-7.541 c=7.690-7.692	β=90.83-90.88
Triclinic	603 - 1013	*P*1-C^1	a=7.30 b=7.52 c=7.69	α=80.85 β=90.82 γ=90.95
Monoclicnic	1013	*P*c-C^2	a=5.275 b=5.155 c=7.672	β=91.7

The structural model of WO_3 is well explained by Kuzmin [Kuzmin 1998]. He suggested two different situations present in an ideal WO_3 surface, when it is under electrically neutral conditions. Assuming, the surface along the (100) crystallographic plane half of the W atoms in valence state W^{+6} are connected to terminal oxygen ions, this leads to the transfer of their electron to the nearest W ion thus forming a W^{5+} state. In the second part W atoms at the surface change their valence state to W^{5+} and then the surface is represented by $W^{5+}O_{20}$ shown in the figure 1.1. In both situations the reaction of W^{5+} with oxidizing atmosphere of air, leads to the formation of W^{6+}-OH bonds in humid conditions.

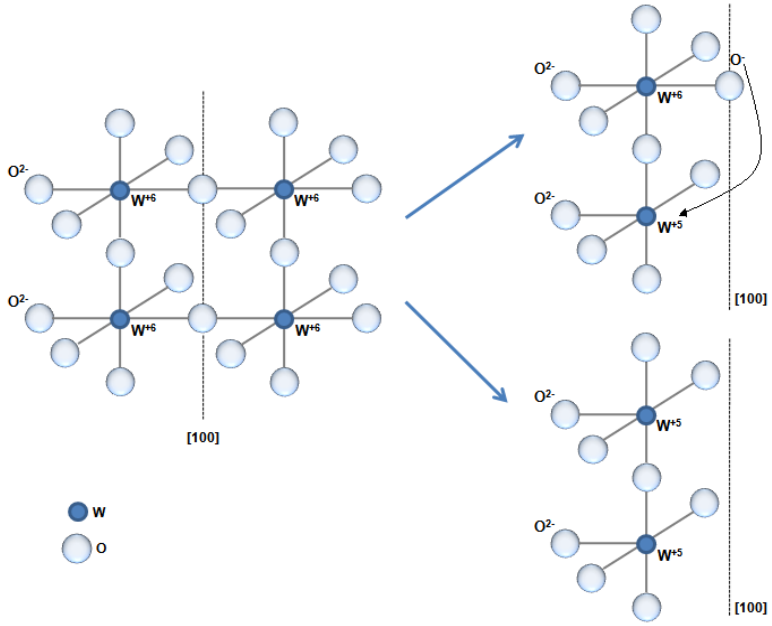

Figure 1.1 Structural model of monoclinic WO_3 grain surface along (100) with two possible states demonstrated on the right

The formation of W oxidation state leads the way for the gas-solid interaction on the surface of thin tungsten oxide films and other structures. This property explains its good sensitivities for gaseous species. Especially, for the environmental pollutants, like NO_x, CO, O_3, NH_3, and also to H_2. As other metal oxide based gas sensors, WO_3 is mostly used in the air at atmospheric pressure. In these conditions, it is believed that most of the gaseous species are detected via their influence on the adsorbed oxygen species. In particular, the investigations have shown that the key reaction of the gaseous species detection involves oxygen ions adsorbed on the surface of the sensor [Moseley 1987]. Thus, at operating temperatures between 473 K and 773 K only O- species which are the most stable at the surface of the metal oxide react with the gases from the enironment [Hellegouarc'h 2001].

Interest in the use of WO_3 for chromic applications arose from its optical properties in the visible wavelengths region, which are dominated by the absorption threshold. The threshold is defined by the bandgap energy (Eg) of WO_3 nanostructures, which ranges from 2.60 – 3.25 eV [Zheng 2011]. These properties make the WO_3 films generally transparent in nature. Nevertheless, light yellowish films were reported for the samples having Eg at the low end due to some absorption of the blue spectrum and light greenish films were observed for non stoichiometric WO_x samples [Hjelm 1996]. The color shift in the transparent WO_3 to dark bluish films (tungsten bronze) can be initiated by applying voltage (electrochromic) or exposing to reducing gas like H_2 (gasochromic).

The electrochromic phenomena in WO_3 is not to be covered in detail as it is beyond the scope of this research. The coloration efficiency of the films is said to be highly influenced by the surface morphology. The high surface area of the WO_3 nanostructured thin films is expected to interact strongly with the gas molecules and as a result, large optical response is observed. Furthermore, the open structure improves the molecules desorption rate from the surface and thus, lower response time than in their bulk structures. This creates opportunity to confirm the optical response of the different WO_3 nanostructured films developed for the gasochromic applications. Investigation should be carried out to determine the influence of the surface morphology for the WO_3 nanostructured films interaction with gas molecules instead of electrolyte (liquid) as in the electrochromic experiments.

The first model introduced for coloration in WO_3 is described by Faughnan et al. [Faughnan 1975]. They suggested a double interjection model where coloration proceeds by double injection of protons/electrons reducing W^{6+} to W^{5+} and as a result, the formation of tungsten bronze takes place. An alternative model is based on the concept of polaron formation introduced by Landau when he argued that displacing atoms or ions in a material from their carrier free equilibrium position produces a potential well that will bind a charge carrier by self trapping [Deb 2008]. In an oxygen vacancy model such as the one accepted for metal oxide gas sensing materials, the coloration process is believed to be due to the defects in the metal oxide films, which contain positively charged oxygen vacancies formed during the preparation explained and shown in figure 1.1. In this doctoral thesis, the gasochromic response has been explained employing a double injection model and by expanding it to the restoration of the films to the transparent state upon the exposure to oxygen. The mechanism is developed on the absorbance response. Being a wide band gap semiconductor, the sensing mechanisms of WO_3 sensors lie in the tungsten multiple oxidation states, the W^{6+} ions can be reduced to W^{5+} during the exposure to different gases such as reducing gases like H_2 or CO [Yaacob 2009]; oxidizing gases usually are chemically adsorbed at the surface of the WO_3 film removing electrons from its conduction band. The result of these chemical reactions can be visualized in the change of the optical absorbance, serving as a base mechanism for the future optical gas sensor device.

1.5 Previously developed sensors in URV

The Department of Electrical and Electronics Engineering of Universitat Rovira i Virgili (URV) have been focusing on the development of semiconductor gas sensors. This

includes the development of new semiconductor materials, their characterization, as well as the testing behavior of the gas sensor devices. In the URV, the semiconductor gas sensors developed, including thin films and thick films have consisted of active layers of metal oxides namely, SnO_2, WO_3, TiO_2, ZnO and Nb_2O_5 on different substrates like ceramic, silicon or silicon micro hotplates.

The working principle of these sensors is based on the change of electrical resistance due to changes in the gases present in their environment. For the thin film sensor reported in [Bittencourt 2002], its active layer consists of WO_3 deposited on a silicon substrate. Thick film sensors with SnO_2 and Pt-SnO_2 as active layers have been reported by [Ivanov 2004]. The sensors on the porous surface such as nano porous alumina via anodic formation with the active layers consisting of the metal oxides especially WO_3, have also been developed in the past years. In one of them, anodic films were employed as a support material for sputtering-deposition of thin films in view of exploiting their gas sensing properties [Gorokh 2006].

Previously in URV, WO_3 devices have also been developed using anodic aluminum on porous silicon. Anodic films were employed as a support material for sputtering-deposition of a thin WO_3 film. These WO_3 sensing layer columns on anodic alumina prepared by RF sputtering were selective to NO_2, ammonia and ethanol at the temperature range from 423 to 573 K [Gorokh 2006]. Also the same material (WO_3) has been used in the detection of other gases such as, NO_x [Gorokh 2006, Vallejos 2007], O_3, H_2S, and SO_2. The sensor device is shown below in Figure 1.2.

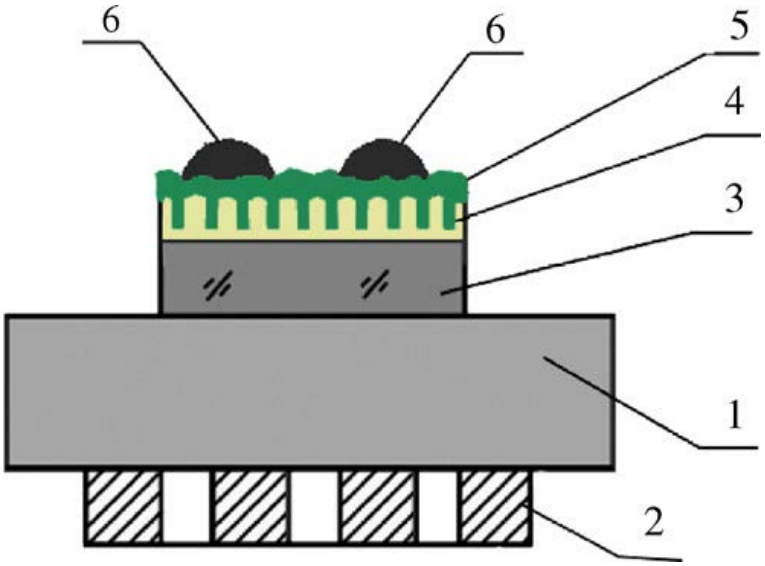

Figure 1.2. Schematic view of a test sensor prepared from a porous alumina film clad with a sputtering deposited sensing layer: 1, ceramic substrate; 2, Pt heater; 3, piece of oxidized Si wafer; 4, porous alumina support; 5, WO_3 active layer; 6, electric contacts [Ivanov 2004]

Recently, Aerosol assisted chemical vapor deposition (AACVD), a new technique of growth for metal oxides has been developed and used in the MiNOS group of URV. This method is used for the direct in-situ growth of intrinsic and metal nanoparticle functionalised nanostructured WO_3, as well as SnO_2-based devices for gas sensing applications. The nanostructured material synthesis, device fabrication and their gas sensing properties have been studied. Using the AACVD method pure and Au or Pt decorated WO_3 nanoneedles have been grown both onto classical alumina or microhotplate gas sensor substrates. These nanostructures were initially grown on the alumina hot plate used for sensor measurements shown in the figure 1.3.

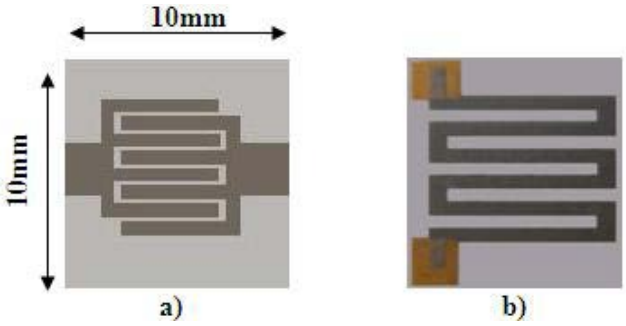

Figure 1.3. Front view images of the traditional alumina substrate with screen-printed inter digitated Pt electrodes on the topside (a) and Pt heater on the backside (b)

Alumina sensor substrates, ready for active layer deposition, were composed of inter-digitated Pt electrodes on the topside and Pt heater on the backside with ~200 µm inter-electrode gap.

The second type of gas sensor substrate used was realized by using micromachining silicon technology. To fabricate such substrates, the materials and functional elements have been chosen and designed by CNM (National Center of Microelectronics), Barcelona, Spain. By using this technology the micro hotplate gas sensor substrate chip, comprises a Pt heater, an insulating layer and Pt electrode deposited and patterned on micromachined membrane.

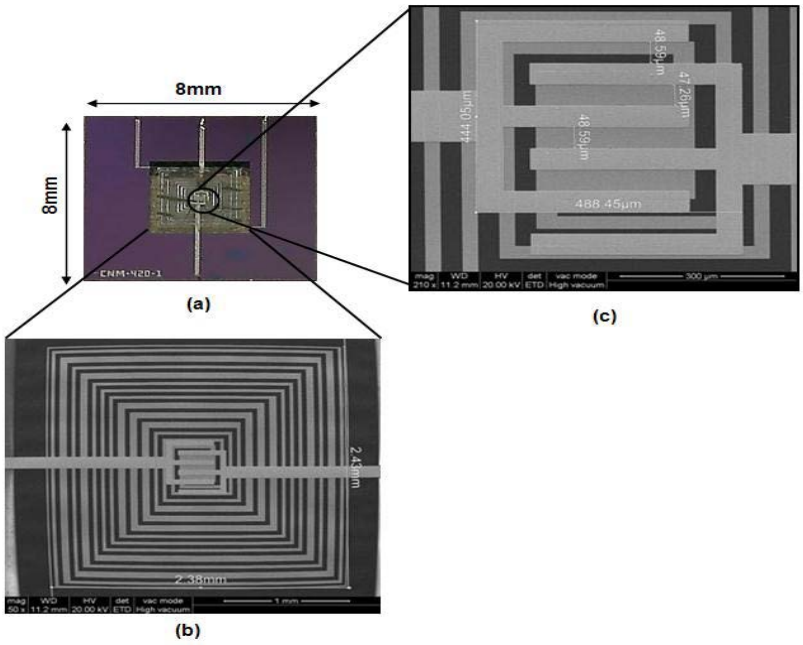

Figure 1.4. The front view images of microhotplate gas sensor substrate: microhotplate chip (a),Pt heater (b) and Pt electrodes (c)

Microhotplate substrates were used to verify the applicability of the deposition method in micromachined gas sensors and to improve the power consumption properties. The gas sensor characterization was achieved by measuring the change of the electrical resistance of the active layer when the gas sensor was exposed to various concentrations of the test gases and at the different operating temperatures. Sensors fabricated with the above mentioned technique and coated with WO_3 or SnO_2 sensing layers have been shown to be useful for sensing a number of gases such as NO_2, H_2, CO, H_2S, benzene (C_6H_6) and ethanol (EtOH). [Navio 2011, Vallejos 2011, Vallejos 2013].

1.6 Main Objective of this doctoral thesis

The aim of the thesis is to get the basis for developing an optical gas sensor employing thin films and nanostructures based on WO_3. Given the state of the art and the previous work done at the URV on WO_3-based gas sensors. The main objectives of the thesis are as follows:

- investigation of the semiconducting metal oxides with gasochromic properties
- deposition or synthesis of the metal oxide nanostructured and thin films onto suitable optical substrates
- selection of a suitable technique to grow the metal oxides nanostructures, among those that are available or can easily be implemented at the university (CVD, AACVD, sputtering, sol-gel)
- comprehensive study of the micro-nanocharacteristics of the nanostructured metal oxides to understand their influence on the optical sensor performance
- investigation of the optical sensing performances (static and dynamic) of the developed sensors towards different ambient pollutants like CO, NH_3, NO_x and H_2
- to understand and explain the gas sensing layer interaction mechanism of these optical sensors
- design or choose the optical measurement techniques, which will be deployed to investigate the gasochromic response of the developed sensors towards the above mentioned gases.

1.7 Important results and main conclusion

In this research work three different technique have been used named as RF sputtering for WO_3 thin film deposition, AACVD for the deposition of pure and Au/Pt WO_3 nanoneedles and WO_3 nanocrystals synthesise using modified Pechini sol – gel method. WO_3 thin films with thicknesses around 550 nm, grown by RF sputtering have been investigated for optical gas senisng using absorbance spectroscopy. These films were doped with Pt and subjected to optical gas sensing under to influence of H_2, CO and NO_x. These films showed fast response and recovery under the influence of mentioned gases. The response and recovery time is in the range of seconds. The undoped WO_3 also shows a detectable optical response to NO_x. The films doped with Pt shows a response to H_2 at room temperature.

Simmilarly, the gaschromic reponse of WO_3 nanoneedles was investigated upon the exposure to NH_3. The nanoneedles decorated with Au and Pt shows optical response when exposed to NH_3 gas at room temperature. The first time reported work of optical response of these nanoneedles at room tempreature is presented in this doctoral thesis. Simmilar to thin films nanoneedles have also shown a fast response and recovery time in the range of seconds.

In summary, this PhD research program successfully fulfilled its objectives to investigate and develop novel WO_3 optical sensors based on nanostructures and thin films. During the work author had successfully implented this material for optical sensing of mentioned gases like NH_3, CO, NO_x, and H_2. The evaluation based on these results made WO_3 a good candidate for future devices.

CHAPTER 2

EXPERIMENTAL METHODS

2 Experimental methods

In this chapter , all the experimental techniques used in this Phd project will be presented. This includes the sample preparation from nanostructures to thin film growth and different characterization techniques used to evaluate WO_3 for optical gas sensing. Detailed description of the results obtained from these techniques will be discussed in the following chapters. Three different techniques have been used to obtain the active materials, namely preparationof thin films, the growth of nanoneedles and the synthesis of WO_3 nanocrystals. The technique used to grow WO_3 thin films was radio frequency (RF) magnetron sputtering. WO_3 nanoneedles were grown by employing aerosol assisted chemical vapor depositon (AACVD) and WO_3 nanocrystals were synthesized using the modified sol-gel Pechini method. The different characterization techniques used were X-ray powder diffraction (XRPD), Atomic force microscopy (AFM), Environmental scanning electron microscopy (ESEM), Transmission electron microscopy (TEM), Micro Raman spectroscopy and, VIS/UV spectroscopy.

2.1 Deposition and synthesis of nanostructured materials

In this chapter the detailed deposition and synthesis of nanostructured WO_3 sensing layer will be discussed. The discussion will also include the deposition methods of the catalytic metals (Pt and Au).

Nanostructured materials are defined as the materials with at least one dimension in the nano scale range (<100 nm). Depending on the dimensions nanomaterials can be categorised into a few classes:

- Zero dimension: nanoparticles and nanocrystals;
- One dimension: nanowires and nanorods;
- Two dimensional: thin films.

The nanomaterials have demonstrated different mechanical, optical, electronic and magnetic properties then their bulk counterparts. The reason is high surface to volume ratio, different surface energy and comparable dimensions with Debye length.

The two most common approaches to fabricate the nanostructured thin films are bottom-up and top-down [Cao 2004]. In the bottom-up approach material is built-up from the bottom atom-by-atom, molecule-by-molecule or cluster-by-cluster [Cao 2004].

It is also refers to controlled or directed self-assembly of atoms and molecules into nanostructures [Zribi 2009].

The top-down approach is considered when the bulk dimensions of a material are reduced until nanometer size features are achieved [Zribi 2009]. Usually, this approach consists of at least one etching step to create nanostructures. The bottom up approach has shown the potential to obtain nanostructures with less defects and more homogeneous chemical composition [Zribi 2009]. It is also preferable because nanostructures with smaller dimension are normally achieved as compared to the top down approach [Chattopadhyay 2010].

2.2 Physical Vapor Deposition (PVD) processes for thin film deposition

Physical vapor deposition processes (often just called thin film processes) are atomistic deposition processes in which material is vaporized from a solid or liquid source in the form of atoms or molecules and transported in the form of a vapor through a vacuum or low pressure gaseous (or plasma) environment to the substrate, where it condenses. Typically, PVD processes are used to deposit films with thicknesses in the range of a few nanometers to thousands of nanometers; however, they can also be used to form multilayer coatings, graded composition deposits, very thick deposits, and freestanding structures [Macleod 2001]. Also, the substrates can range in size from very small to very large, for example the 3 × 3 m glass panels used for architectural glass. The substrates can range in shape from flat to complex geometries such as watchbands and tool bits. Typical PVD deposition rates are 10–100 Å per second. In general one can refer to, PVD and CVD process atomistic deposition process. In these proceses overlay material is deposited atom-by-atom. The resulting film can range from single crystal to amorphous, fully dense to less than fully dense, pure to impure, and thin to thick. The main categories of PVD processing are vacuum deposition (evaporation), sputter deposition, arc vapor deposition, and ion plating, as depicted in Figure 2.1.

2.2.1 Vaccum deposition

In vaccum deposition the material from a thermal vaporization source reaches the substrate with little or no collision with gas molecules in the space between source and substrate. In vaccum deposition the typical pressure is set in between the range of 10^{-5} Torr to 10^{-6} Torr. Vacuum deposition is used to form optical interference coatings, mirror coatings, decorative coatings, permeation barrier films on flexible packaging

materials, electrically conducting films, wear resistant coatings, and corrosion protective coatings [Mattox 2010].

2.2.2 Arc vapor deposition

In arc vapor deposition a high current and low voltage arc is used to vaporize a cathodic electrode (cathodic arc) or anodic electrode (anodic arc) and deposit the vaporized material on a substrate. Arc vapor deposition is used to deposit hard and decorative coatings.

2.2.3 Ion plating

In ion plating which is also refered to as ion-assisted or ion vapor deposition utilizes concurent or periodic bombardment of the depositing film by atomic size energetic particles to modify and control the properties of the depositing film. Ion plating is used to deposit hard coatings of compound materials, adherent metal coatings, optical coatings with high densities, and conformal coatings on complex surfaces.

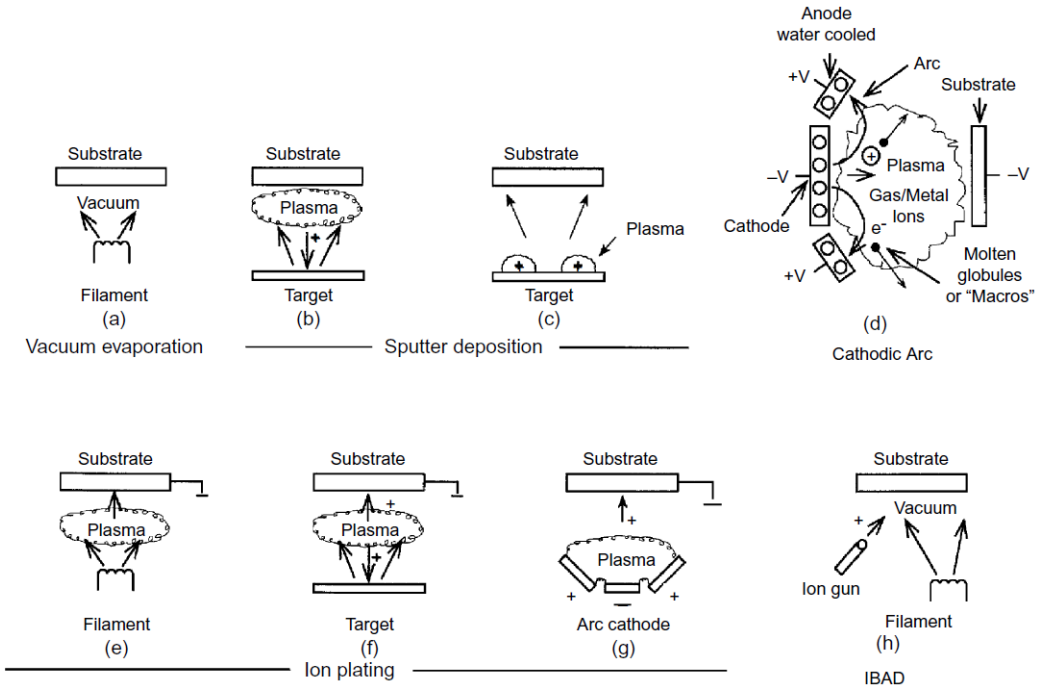

Figure 2.1 PVD Processing Techniques: (a) Vacuum Evaporation, (b) and (c) Sputter Deposition in a Plasma Environment, (d) Sputter Deposition in a Vacuum, (e) Ion Plating in a Plasma Environment with a Thermal Evaporation Source, (f) Ion Plating with a Sputtering Source, (g) Ion Plating with an arc Vaporization Source, and (h) Ion Beam-Assisted Deposition (IBAD) with a Thermal Evaporation Source and Ion Bombardment from an Ion Gun [Mattox 2010]

2.3 Sputtering preparation technique

Sputtering is a mechanism by which atoms are dislodged from the surface of a material as a result of collision with high-energy particles. Thus, PVD by Sputtering is a term used to refer to a physical vapor deposition (PVD) technique wherein atoms or molecules are ejected from a target material by high-energy particle bombardment so that the ejected atoms or molecules can condense on a substrate as a thin film. Sputtering has become one of the most widely used techniques for depositing various metallic films on wafers, including aluminum, aluminum alloys, platinum, gold, TiW, and tungsten.

Sputtering as a deposition technique may be described as a sequence of these steps:

1. ions are generated and directed at a target material;
2. the ions sputter atoms from the target;
3. the sputtered atoms get transported to the substrate through a region of reduced pressure;
4. the sputtered atoms condense on the substrate, forming a thin film.

Sputter deposition of films was first reported by Wright in 1877 [Wright 1877] and at that time, it was feasible because only a relatively poor vacuum is needed. Edison patented a sputter deposition process for depositing gold on wax phonograph cylinders in 1904. Sputter deposition was not widely used in industry until the need developed for reproducible, stable, long-lived vaporization sources for production, and the advent of various types of magnetron sputtering. Planar magnetron sputtering, which uses a magnetic field to confine the motion of secondary electrons to near the planar target surface, is presently the most widely used sputtering configuration.

Sputter deposition can be performed by energetic ion bombardment of a solid surface (sputtering target) in a vacuum using an ion gun or low pressure plasma (< 5 mTorr) where the sputtered particles suffer few or no gas phase collisions in the space between the target and the substrate.

Sputtering can also be done in a higher plasma pressure (5–30 mTorr) where energetic particles sputtered or reflected from the sputtering target are thermalized by gas phase collisions before they reach the substrate surface. The plasma used in sputtering can be confined near the sputtering surface or may fill the region between the source and the substrate. The sputtering source can be an element, alloy, mixture, or a compound

and the material is vaporized with the bulk composition of the target. The sputtering target provides a long-lived vaporization source that can be mounted so as to vaporize in any direction.

2.3.1 Magnetron sputtering

Magnetron sputtering is a plasma coating process whereby sputtering material is ejected due to bombardment of ions to the target surface. The vacuum chamber of the PVD coating machine is filled with an inert gas, such as argon. By applying a high voltage, a glow discharge is created, resulting in acceleration of ions to the target surface and a plasma coating. The argon-ions will eject sputtering materials from the target surface (sputtering), resulting in a sputtered coating layer on the products in front of the target. Magnetron sputtering is somewhat different from general sputtering technology. The difference is that magnetron sputtering technology uses magnetic fields to keep the plasma in front of the target, intensifying the bombardment of ions.

In RF magnetron sputtering, the electrodes between which the substrate is placed, are driven by an RF power source, which generates plasma and ionizes the gas (e.g., argon) between them. A DC potential is used to drive the ions towards the surface of one of the electrodes (the target) causing atoms to be knocked off the target and condense on the substrate surface. A strong magnetic field is applied to contain the plasma near the surface of the target to increase the deposition rate. The process is typically performed on one side of the substrate at a time a typical RF magnetron sputtering schematic view is shown in the figure 2.2.

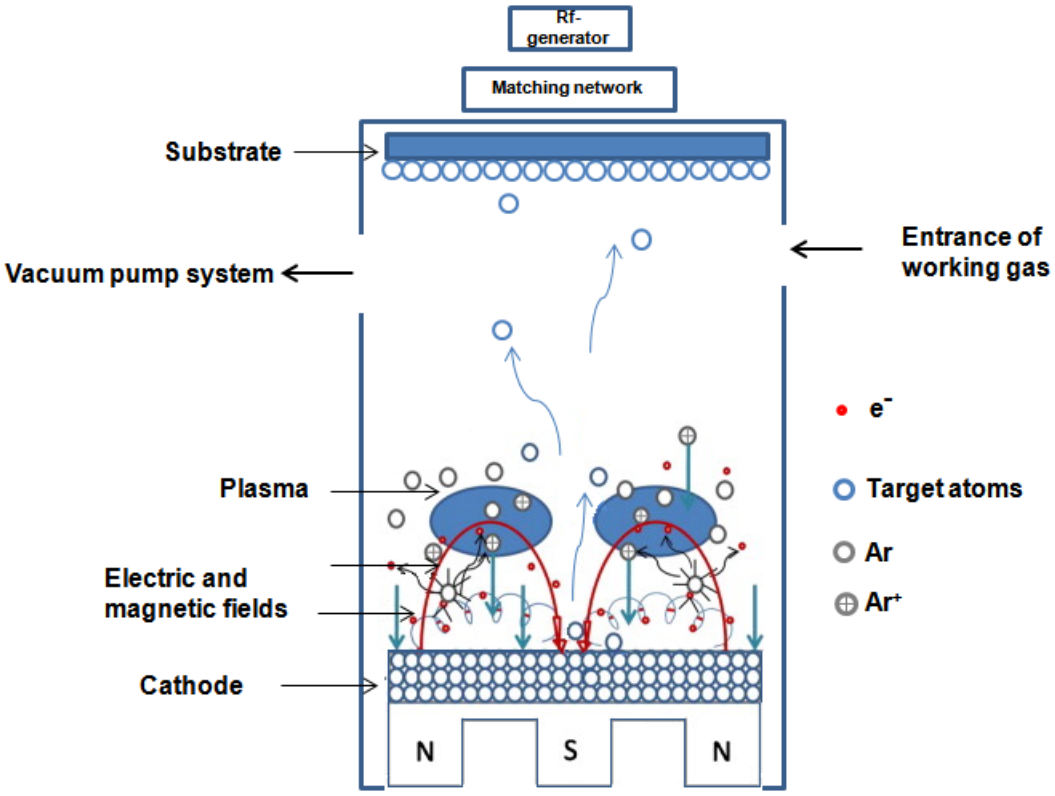

Figure 2.2 A schematic illustration of the typical RF sputtering system

Here, magnets are used to increase the percentage of electrons that take part in ionization events and thereby increase the probability of electrons striking the Argon atoms, increase the length of the electron path, and hence increase the ionization efficiency significantly.

In this work, the nanostructured WO_3 thin films deposited onto quartz (fused silica) substrate were preduced in an ESM100 Edwards RF magnetron sputtering system with a planar magnetron cathode and a rotatable substrate holder. The sputtering process of the thin films was performed in UPC (Polytechnical University of Catalonia), Barcelona, Spain.

2.4 Growth of nano-needles

2.4.1 Chemical vapor deposition (CVD)

Chemical vapor deposition (CVD) is a process in which the chemical constituents react in the vapor phase near or on a heated substrate to form a solid deposit. The conventional CVD processes are based on thermally activated CVD, which uses inorganic precursor sources. The deposition process is initiated by thermal energy and

can occur at atmospheric pressure, low pressure or ultrahigh vacuum. The deposition often requires relatively high temperatures (typically 773–1673 K) depending on the type of inorganic precursor (e.g. halides, hydrides, etc.) used. The factors controlling a CVD process are [Pierson 1999]:

- Thermodynamic, mass transport, and kinetic considerations;
- The chemistry of the reaction;
- The processing parameters of temperature, pressure, and chemical activity.

As CVD is a generic name for a group of vapour-processing-based deposition methods. The variants of CVD-based method differ in processes used, architecture of the reactor chamber, heating method, pressure and temperature ranges, type and transport of the precursor-solvent solution. The other variants of CVD may require special reactor at lower pressure (typically 1.3–1333 Pa) to generate the plasma (PECVD) or the chemical reaction will occur only on the base of the metal-organic precursor (MOCVD). The other variants like Aerosol Assisted CVD (AACVD), Atmospheric Pressure CVD (APCVD) and Low Pressure CVD (LPCVD) are more flexible and can be performed at atmospheric or reduced pressure. Still, the main difference between them is the value of the pressure and the type of the reactor used.

CVD is a widely used material-processing technology. The majority of its applications involve applying solid thin-film coatings to the surface, but it is also used to produce high-purity bulk materials and powders, as well as fabricating composite materials. It is an extremely versatile process that can be used to process almost any metallic or ceramic compound. Some of these include: elements, metals and alloys, carbides, nitrides, borides, oxides, intermetallic compounds.

In the last years CVD became very popular for deposition of layers. Nowadays, they are used in a wide range of applications:

1. Coatings;
2. Semiconductors and related devices;
3. Dense structural parts – components that are difficult or uneconomical to produce using conventional fabrication techniques;
4. Optical fibres;
5. Composites – production of ceramic matrix composites;
6. Powder production;
7. Catalysts;

8. Nanomachines – application in silicon microfabrication technology.

In general a CVD proces requires the following steps for the deposition of solid materials, as shown in figure 2.3 [Choy 2003]:

1. Generation of active gaseous reactant species;
2. Transport of the gaseous species into the reaction chamber;
3. Gaseous reactants undergo gas phase reactions forming intermediate species:
   a) a homogeneous gas phase reaction can occur at a high temperature above the decomposition temperatures of intermediate species inside the reactor. The intermediate species undergo subsequent decomposition and/or chemical reaction, forming powder and volatile by-products in the gas phase. The powder will be collected on the substrate surface and may act as a crystallisation centre.
   b) Diffusion/convection of intermediate species occurs across the boundary layer at temperatures below the dissociation of intermediate phase. These intermediate species subsequently undergo steps (4)–(7).
4. Gaseous reactants adsorb onto the heated substrate and the heterogeneous reaction occurs at the gas-solid interface (i.e. heated substrate), resulting in producing the deposit and the by-product species;
5. Both the diffusion of the deposit on the heated substrate forming crystallisation centers and the growth of the film take place simultaneously;
6. Removal of gaseous by-products by diffusion or convection;
7. The by-products and the unreacted gaseous precursors are transported away from the deposition chamber.

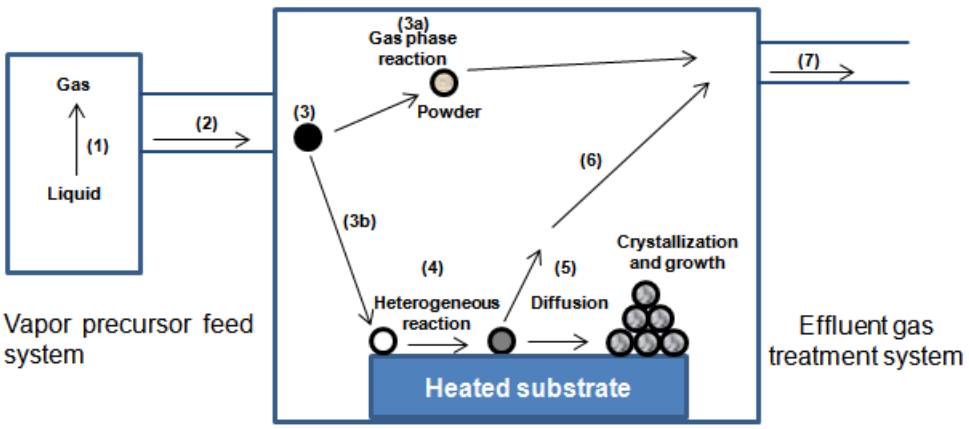

Figure 2.3 A schematic diagram of CVD coating [Choy 2003]

2.4.2 Aerosol assisted chemical vapor deposition (AACVD)

AACVD processes, as a variant of conventional CVD processes use aerosol as a delivery system. It involves the atomization of a liquid precursor solution into the fine sub-micrometer-sized aerosol droplets that are distributed throughout a gaseous medium. In Figure 2.4 a simple scheme is presented related to an AACVD-based process.

The use of aerosol assisted deposition was first reported by J.Akedo et al [Akedo 1999], in 1999 for the preparation of dense ceramic films at room temperature. Later aerosol has been used widely as a material source for the deposition of thin films. The advantages of using aerosols as a delivery system are relatively low equipment costs and wider options for precursor materials. These open atmosphere processing methods offer advantages of a relatively low processing temperature and a simple and flexible technique for preparing coatings without the use of a sophisticated reactor or a vacuum system. Key process parameters such as deposition temperature, properties of the precursor, solvents employed, etc... can be varied to control the microstructure, porosity, grain size and composition of the coatings and deposits.

The four steps involved in the the AACVD process as shown in the Figure 2.4 are: The starting solution (1) can be a pure liquid, single-source precursor or a mixture of several liquid chemicals. The criteria for the selection of solvents for the atomization process is high solubility of the precursors, low vapour pressure and low viscosity [Hubert-Pfalzgraf 1998]. The atomization or converting into aerosol droplets (2) of the starting precursor solution can be carried out using various types of aerosol generators. Carrier gases are used to assist the generation of aerosol and transport the aerosol to the reaction zone. Argon and nitrogen are the most common inert carrier gases. After atomization, the precursor aerosol is transported to the heated zone (3), where evaporation of solvent and vapourization of precursor take place prior to the major chemical reactions (4). For pure precursor, the vapourization can occur directly from the aerosol droplets. As the vapourization of precursor is the key feature of AACVD, differing from other aerosol processes for material synthesis, the selection of the starting precursor and the control of processing parameters are very important to ensure the true CVD process.

We have used an AACVD process to grow nano-needles of WO_3 on quartz substrate. The method has traditionally been used when a conventional atmospheric pressure

CVD (APCVD) precursor proves involatile or thermally unstable. However, by designing precursors specifically for AACVD, the restrictions of volatility and thermal stability are eliminated and the range of molecules suitable for use as CVD precursors is broadened.

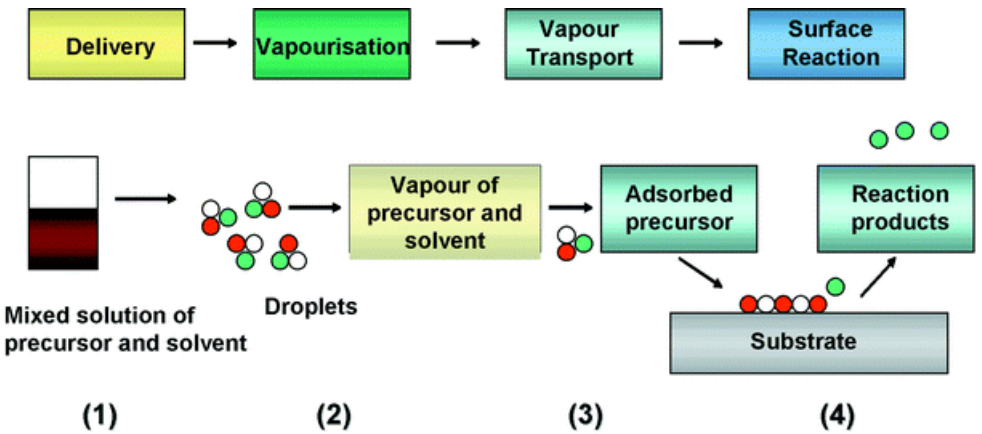

Figure 2.4 Schematic illustration of the AACVD based process [Stoycheva 2011]

2.4.2.1 AACVD system

A cylindrical AACVD reactor chamber was fabricated from stainless steel by our technical services. It consists of two cylindrical pieces, with 95 mm diameter and height of 20 mm each, used as the base (bottom) and the cover (top) of the reactor. A detailed scheme of the reactor chamber is presented in Figure 2.5. The bottom part contains a square placement for the substrate with dimensions 10 x 10 mm, two heater cartridges (8mm - diameter, 23,45 W/cm^3 WATLOW) parallelly embedded below the substrate placement and a type K thermocouple (1.6 mm - diameter and 152 mm - length, WATLOW) introduced vertically under the substrate placement. The cover was positioned parallel to the substrate and 7 mm above it. The reactor inlet was positioned horizontally, while the exhaust was positioned vertically to the substrate. To control the temperature of the deposition process a PID power controller (EUROTHERM, model 3216) and temperature controller (single-phase thyristor unit, EUROTHERM, model 7100A) were connected to the deposition system. The design of the deposition system was made with the potential to increase the temperature up to 923 K.

The generation of the aerosol solution, i.e. a fine mist of liquid droplets, was performed in a commercial piezoelectric ultrasonic atomizer (frequency ~ 1.5 MHz, CHICCO). The formation of an aerosol is required for the delivery process mechanism of a liquid and gas mixture through tube connections. The aerosol mist was formed from a liquid precursor solution contained in a round flask (250 ml capacity, Afora). This flask was immersed in a tank of the ultrasonic atomizer (500 ml capacity), containing water (300 ml). The bottom of the round flask was placed over the centre of the ultrasonic mist generator, which was the most effective position for the generation of fine aerosols.

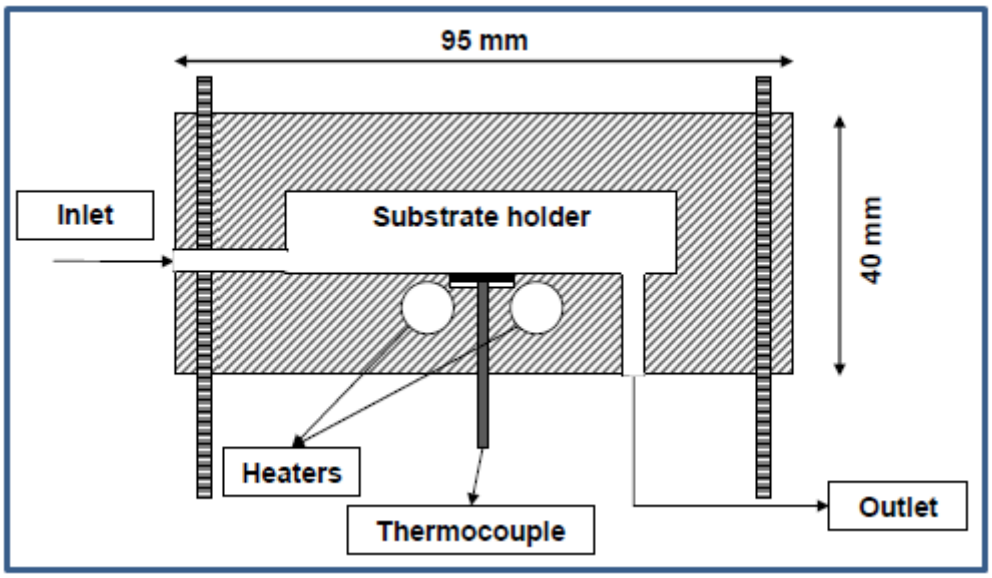

Figure 2.5 Schematic view of AACVD reactor chamber.

The produced fine mist was then transported by the aid of the carrier nitrogen gas (N_2 Premier, Carburos Metálicos) into the heated reactor chamber, which held the sample substrate. The flow-rate (0.5 L/min) of nitrogen gas was controlled by using the needle valve on a gas flow meter (KeyInstruments, model 3A14), with measuring range of up to 5 L/min ±4%. All gas-handling lines were made of the PTFE (Teflon) material and have had 3.45 mm internal and 6.35 mm external diameter. All the experiments were performed inside the fume-cupboard. The experimental setup is shown in the figure 2.6.

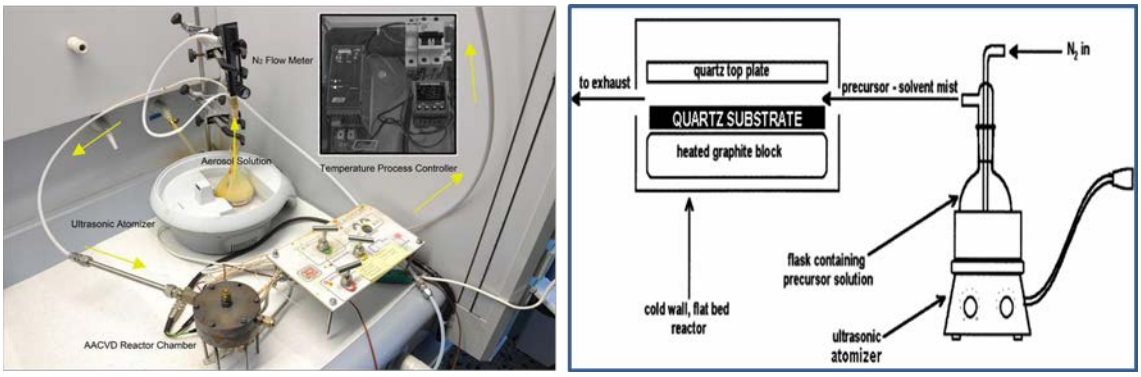

Figure 2.6 Experimental set up of the AACVD procedure

2.5 Synthesis of nano-crystals

2.5.1 Sol-Gel method

The sol-gel is a wet chemical method used for fabrication of materials typically metal oxides. A sol is a fluid colloidal dispersion of solid particles in a liquid phase where the particles are sufficiently small to remain suspended by Brownian motion. A gel is a colloidal suspension of a liquid in a solid, an interconnected polymeric network formed by assembly of the sol [Brinker 1990].

A simple description of the sol-gel synthesis route is that a sol is prepared by dissolving metal ion complexes in a suitable organic solvent, and then by hydrolysing, the sol forms as a colloidal metal oxide/hydroxide precipitate. After heating, the sol is transformed into a gel in which the metal oxide or hydroxide particles form a poly-meric network enclosing the solvent. Then, the gel is heated at higher temperatures and the organic compounds are evaporated or decomposed, allowing the inorganic solid to crystallize. All the proposed synthetic methodologies in preparing Sol-Gel films can be traced back to three fundamental stages:

1. Preparation of liquid solutions of suitable precursors;
2. Sol transformation and gel formation;
3. Thermal treatment of the gel (in bulk or film configuration) to obtain the final solid.

This general and highly versatile method presents some fundamental advantages:

1. Most of the synthetic steps can be carried out at room conditions;
2. Materials composition can be easily and precisely controlled;

3. Homogeneous coatings on suitable substrates can be made;
4. The purity of the final material can be very high.

The preparation of multicomponent glasses by the sol-gel process dates back to the 50's. Della and Rustum Roy [Roy 1955] prepared numerous compositions from silicon tetraethoxide and metal nitrate salts primarily for phase equilibrium studies where homogeneous samples are essential. This new method gave products which, when melted just once, gave a more homogeneous glass than the best glasses obtained after three successive melting and crushing operations of samples prepared in the conventional manner from individual oxides. Nowadays sol-gel methods are synthetic routes for preparing inorganic powders at low temperature.

2.5.2 Sol-gel modified Pechini method

The Pechini method, developed by M. Pechini, is a variant of sol-gel methodology [Pechini 1967]. It is an alternative to the conventional sol-gel method, which is based on the ability of certain weak acids to form metallic complexes by a complexation reaction using α-polycarboxylic acid, generally citric acid. The metal cations are chelated by the carboxyl groups and remain homogeneously distributed in the polymeric network. Then, these chelates react with a polyalcohol such as ethylene glycol (EG) that is added to the solution. When the solution is heated, the polymeric resin is formed by a sterification reaction, leading to a dehydration reaction of a-polycarboxylic acid and ethylene glycol. The dimeric product of the ester contains one alcoholic hydroxyl group (HO-) and one carboxyl acid group (-COOH). This reaction occurs in sequence to obtain a polymeric network.

The principle of the Pechini method is to obtain a random polymeric resin precursor in which the cations are uniformly distributed, as is schematically shown in figure 2.7. Heating of the polymeric resin at 573 K causes the polymer to break down. Later, during the pyrolysis,the cations are segregated because of low cation mobility in the branched polymer.

In the modified Pechini method, ethylene diamine tetraacetic acid (EDTA) was used to replace citric acid due to its strong chelating power. EDTA has four carboxylic acid groups (citric acid has three) and can react with EG to form a more branched polyester thus giving a more homogeneous sol [Kakihama 1996]. P. A. Lessing has discussed the polymeric chain, which can be formed between EDTA-EG, EDTA-EDTA and EGEG

[Lessing 1989].The last stage in the synthesis of the nanocrystals is the total calcination of the precursor powder. The calcination temperature and time must be controlled.

In this work, the modified Pechini method was used to obtain WO_3 nanocrystals. In the first step a precursor powder of WO_3 has been obtained. Then this precursor powder has been subjected to a calcination process. The calcination procedure was performed in a vertical furnace using a Kanthal AF resistance heating wire (1 mm Ø wire) made in the laboratories of FiCMA-FiCNA. The temperature was controlled by a Eurotherm 902-904 controller/program, which was connected to a thyristor to control the power furnace. The details of WO_3 nanocrystal synthesis are dexcribed in the next chapter.

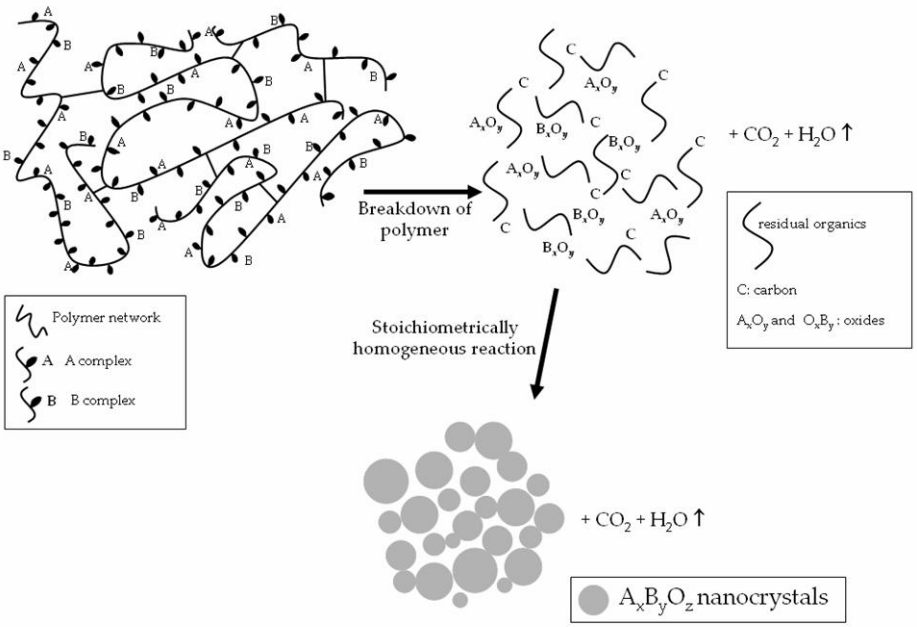

Figure 2.7 schematic illustration of polymeric precursor method [Galceran 2011].

2.6 Structural characterization techniques

2.6.1 X-Ray powder diffraction (XRPD)

The XRPD technique is an analytical technique which gives us information about the crystalline structure, structural phase mixing, etc. By observing the scattered intensity of an X-ray beam hitting a sample as a function of incident angle the information about

the crystallographic structure, is obtained. The principle of X-ray powder diffraction is based on Bragg's diffraction law.

$$2d_{hkl}\sin\theta = n\lambda$$

Here λ is the wavelength of incident ray and d_{hkl} is the spacing between the planes in the atomic lattice, and θ is the angle between the incident and scattered rays.

X-ray powder diffraction (XRPD) measurements were made using a Bruker-AXS D8-Discover diffractometer. equipped with an open Euler ring working with Schulz geometry with parallel incident beam (Gobel mirror) and a vertical goniometer. The system was also equipped with a collimator for the X-ray beam of 500 μm and a General Area Detector Diffraction System (GADDS) detector. The GADDS detector was 30 × 30 cm^2 with a 1024 × 1024 pixel CCD detector. Cu (λ = 1.54056 Å) radiation was obtained from a copper X-ray tube operated at 40 kV and 5 mA. This equipment is available in the Servei de Recursos Científics i Tècnics of URV. The angular range was between 10º and 70º for 2θ data was collected with an angular step 0.050º, 3 s per step and sample rotation. Also X-ray powder measurements were done using slow conditions with angular range between 10º and 70º and the data was collected with an angular step 0.02º, 16 s per step. With the data obtained from slow conditions, unit cell parameters were refined using program Fullprof [Rodriguez-Carvajal 1998], in which Rietveld method [young 1995] is used.

The calculation for the grain size was done using Scherrer's formula [Patterson 1939] in which FWHM of the XRPD performed with slow conditions is used. The Scherrer's formula for calculating the grain size D, is as follows,

$$D = \frac{k\lambda}{B\cos\theta}$$

Where B is the FWHM is measured in radians of 2θ, λ= 1.5405Å is the diffractometer wavelength, θ is the Bragg angle of the peak and K is a constant equal to 2(ln2/π)1/3≈0.9 [Patterson 1939].

2.6.2 Raman spectroscopy

The Raman spectroscopy technique is used to study the vibrational, rotational and low frequency modes in molecules and crystalline structure.

Raman spectroscopy is the study of the interaction between light and matter in which the light is inelastically scattered: a process called the Raman Effect. Photons interacting with matter most commonly scatter elastically. This is called Rayleigh scattering as shown in Figure 2.8. Rayleigh scattered photons have the same wavelength as the incident light. However, approximately 1 out of a million photons are inelastically scattered, this is: the wavelength of the emitted photon and is slightly different than that of the incident photon. Raman scattering is created by irradiating a sample with a light source at one specific wavelength. Today, this monochromatic light source is usually in the form of a laser. In order for this to work, the laser has to be at a wavelength so as not to be absorbed by the matter. Light from the illuminated spot (where the laser is subjected) is collected with a lens and sent through a monochromator. Wavelengths close to the laser line, due to elastic Rayleigh scattering, are filtered out while the rest of the collected light is directed to a detector [Ferraro 2003].

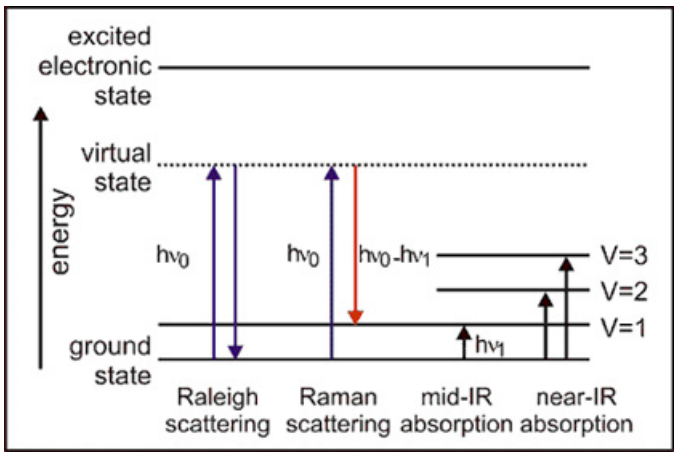

Figure 2.8 Description of different scatterings in energy levels

Raman microscopy is based on the principle of Raman Effect with standard optical microscope, and adds an excitation laser, a monochromator, and a optical sensitive detector such as a charge-coupled device (CCD), or photomultiplier tube, (PMT).

In the current work we have used an inVia Raman microscope of Reinshaw Inc. This state-of-the-art microscope is available in the research equipment unit of Servei de Recursos Científics i Tècnics of URV. We measured the Raman shift for the WO_3 thin film. We used a 785 nm diode laser, a holographic grating 1200 l/mm and DM 2500 Leica microscope with spectral resolution of 0.2 to 0.5 cm^{-1}. The data output is collected through the computer using software named Wire3 specifically developed for inVia Raman microscope. We also did the measurements at different temperatures higher than, and also equal to room temperature.

2.7 Electron Microscopy characterization techniques

Electron microscopy is an extremely important technique for examining particle size, size distribution and the degree of sample homogeneity.

The electron microscope uses electrostatic and electromagnetic lenses to control the electron beam and focus it to form an image. These electron optical lenses are analogous to the glass lenses of a light optical microscope. In an electron microscope, the high energy electrons are generated from a filament by using a large accelerating voltage; electrons interact much more strongly with matter than photons. Beams of these fast-moving electrons are focused on an object and are absorbed or scattered by the object so as to form an image on an flourescent screen and camera.

2.7.1 Environmental Scanning Electron Microscopy (ESEM)

In the current work we have used environmental scanning electron microscopy for the structural morphology and topographical analysis. The working principle of ESEM is the same as conventional electron microscopy (SEM), i.e. the high–energy electrons are used to generate a variety of signals at the surface of the solid specimens. These signals include secondary electrons (to produce the SEM image), back scattered electrons and diffracted back-scattered electrons. The secondary electrons are used to image the specimen; they are valuable for showing the topography and morphology of the specimen. The diffracted back-scattered electrons illustrate contrast in the multiphase of the specimen. In most of the applications data is collected over a selected area of the specimen and two dimensional images are generated that display spatial variations of the specimen. One advantage of using the ESEM is that, it operates in wet mode. So, it is not necessary to make nonconductive samples conductive. Material samples do not need to be desiccated and coated with gold or palladium, for example, and thus their original characteristics may be preserved for further testing or manipulation. We may image the sample, modify the sample, and image the sample again, without destroying its usefulness by having coated it to make it conductive. We can also perform dynamic experiments with the ESEM in wet mode; from high temperatures uptill 1700 K.

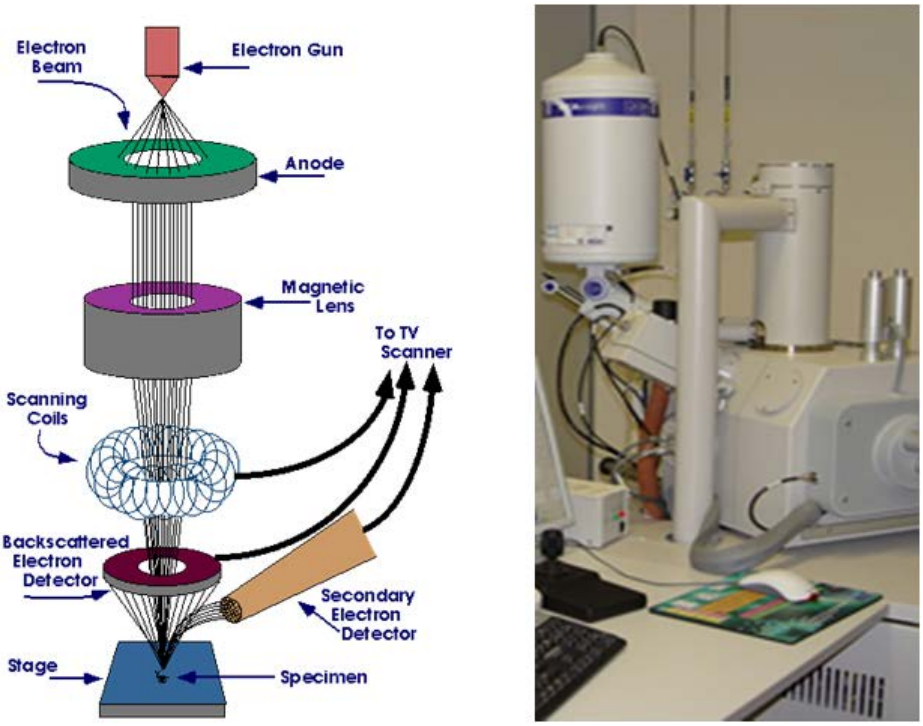

Figure 2.9 ESEM equipment (Left: layout and working principle, Right: photograph of the equipment available at Servei de Recursos Científics i Tècnics of URV).

In this study we used a FEI QUANTA 600 ESEM. The schematic view of the ESEM and a picture of the equipment used are shown in Figure 2.9. This equipment is available at the Servei de Recursos Cientifics i Tecnics, Universitat Rovira i Virgili, Tarragona.

2.7.2 Transmission Electron Microscopy (TEM)

Transmission electron microscopy (TEM) is a microscopy technique where a beam of electrons is transmitted through an ultra thin specimen, interacting with the specimen as it passes through. An image is formed from the interaction of the electrons transmitted through the specimen; the image is magnified and focused onto an imaging device, such as a fluorescent screen, a layer of photographic film, or to be detected by a sensor such as a CCD camera. The main use of this technique is to examine the specimen structure, composition or properties of sub-microscopic details so that this technique is significantly employed in numerous fields such as material science, chemistry, biological components etc. TEM offers the most powerful magnification with high quality images, and provides information on element and compound structure. These are able to yield information of surface features, shape, size and structure.

TEM utilizes a focused beam of electrons instead of light, which increases greatly the resolving capabilities. In this TEM system, there are essentially three types of lenses used to obtain the final image. These are condenser, objective, and projector lenses. The function of condenser lenses is to concentrate and focus the beam of electrons coming from the filament on to a sample to a uniformly illuminate it. The objective lens and its associated apertures are the heart of the TEM. These are used to form the initial enlarged image of the illuminated portion of the specimen in a plane that is suitable for further enlargement by the projector lens. When the electrons pass through the sample, some of them passes through the dense atoms and only few are deflected. These scattered electrons generally make their way down in the column and contribute to the image. So, in order to eliminate these scattered electrons to form the image, an aperture is placed at the objective lens. Smaller apertures are used to form the image. Finally the projector lens is used to magnify the image on the phosphor screen. For higher magnifications the intermediate lenses can also be used to obtain an image. TEM produces high resolution with two dimensional images at a maximum potential magnification of 1 nm resolution. We used a JEOL model-1011 TEM equipment with a current accelerating voltage of 100kV. This equipment is available at the Servei de Recursos Cientifics I Tecnics,URV, Tarragona.

2.8 Atomic force microscopy (AFM)

Atomic force microscopy (AFM) is a very high resolution scanning probe microscopy. The working principle of all AFM microscopes is based on measuring the interaction forces between the specimen surface and a tip or probe placed much closer very close to it. The difference with other microscopes with AFM is in imaging that with AFM, we can have three-dimensinal representation of the sample surface topgraphy. Especially, it can achive the resolution of fractions of a nanometer and unlike the other microscopes it can image the specimen both in liquid and air.

AFM works on a simple principle. It consists of a cantilever with a sharp tip (probe) on its end which scans over the surface. When the tip comes in contact with the sample surface, forces between the tip and the sample surface leads to the deflections as consequence of mechanical forces such as, van der Waals forces, capillary forces, chemical bonding, electrostatic force etc… The cantilever deflection is measured using a laser spot reflected from the cantilever top surface into an array of photodiodes. AFM operates mainly in three different modes, contact mode, or constant force mode, in the

deflection of the cantilever is kept constant by the feedback system, so that the height is mapped. In non-contact mode, the cantilever is oscillated near its resonant frequency so that the height between the sample and the tip can be kept constant by keeping constant the oscillation freqency. Finally, in tapping mode, the oscillation amplitude is one order of magnitude bigger than for non-contanct mode and what is kept constant is the oscillation amplitude.

In this work AFM measurements were carried out in tapping mode using, Pico SPM II (Pico+) AFM equipment. This is available at Servei de Recursos Cientifics i Tecnics, URV, Tarragona.

2.9 Optical characterization techniques

2.9.1 Transmittance and absorption measurements

Absorption is the fraction of incident electromagnetic radiation absorbed by electrons, ions or molecules in the material over spectral ranges of light such as ultraviolet (UV), visible and infrared (IR). The Beer-Lambert law is an empirical relationship that relates the intensity of light to the absorption properties of the material through which the light is traveling

$$I = I_0 \exp(-\alpha d)$$

where I is the intensity of the emerging radiation, I_0 is the incident light intensity, α is the absorption coefficient and d is the thickness of the sample. Experimentally, we measure the optical density (OD) using a double beam spectrophotometer.

$$I = \log(I_0/I)$$

Transmission is the property of a substance to permit the passage of light, with some or none of the incident light being absorbed in the process.

Transmission and absorption studies were carried out in a Varian Cary 5000 scan spectrometer, available at the FiCMA and FiCNA. This is a double ray spectrophotometer with an effective spectral range from 0.25 to 3 μm and allows to measure optical densities from 0 to 10. This spectrophotometer has two monochromators with a 1200 l/mm grating in the UV- visible region and a 300 l/mm grating in the IR region. The light sources of the spectrophotometer are a deuterium lamp for the UV range and a quartz halogen source in the visible-IR range.

2.9.2 Photoluminescence measurements

Photoluminescence is the spontaneous emission of light from a material under optical excitation. When light of sufficient energy is incident on a material, photons are absorbed and electronic excitations are created. Eventually, these excitations relax and the electrons return to the ground state. If radiative relaxation occurs, the emitted light is called photoluminescence. This emitted light can be collected and analyzed to yield a wealth of information about the photoexcited material. The photoluminescence spectrum provides the transition energies, which can be used to determine electronic energy levels. The luminescent intensity gives a measure of the relative rates of radiative recombination.

The samples were excited with Nd:YAG laser in the UV range (290-330 nm). For detection, the emission was collected at an angle of 90º to minimize the influence of the laser pump and was dispersed by a JOBIN YVON-SPEX HR 460 double monochromator with a focal length of 460 mm and a spectral resolution of 0.05 nm. The detectors used waere a cooled Hamamatsu R55092-72 NIR photomultiplier for the infrared range and Hamamatsu PMTR928 for the visible range. The detectors were connected to the lock-in amplifier process (Perkin Elmer DSP-7265).

2.10 Gas Sensing set -up

Tests for gases detection were studied at the Department of Mechanical Engineering-Materials of the Padova University during this doctoral project: it can hold up to 6 gas cylinders. Samples were tested by making optical absorbance measurements using a Harrick gas flow high temperature cell Shown in the figure 2.10 Permits spectroscopy studies of solid samples at temperatures ranging from ambient to in excess of 500°C (www.harricksci.com/high-temperature-cell), coupled with a Jasco V-570 spectrophotometer.

Figure 2.10 High temperature gas flow cell for Optical measurements in spectrophotometer.

The cell is provided with a heater in Tests were exposed to following different gases

Hydrogen (H_2): 1% v/v

Carbon monooxide (CO): 1% v/v

Nitrogen Oxide (NO_x): 1000 ppm

The concentration of the gases was calibrated in the gas cylinders attached to the spectrometer. All gasses were balanced in the dry air, at a flow rate of 0.4 l/min and at temperature ranging from room temperature (RT) to 573 K. the substrate size was approximately 1 cm x 2cm and covering a 6 mm x 1.5 mm section area.

The tests were performed with the following procedure: first, subsequent absorption spectra over the whole desired wavelength range are collected under different atmospheres. Then, the response intensity is evaluated using the optical absorbance change parameter during the exposure to air, $\Delta Abs = Abs_{gas} - Abs_{air}$.

The Δ Abs curve as a function of the wavelength allows to indentify the wavewelength where the response is maximum, or where one gas is not interfering with another: once these wavelengths have been chosen, time resolved tests are performed at a single wavelength varying the gas composition and concentration in the test cell over time.

To analyze the dynamic behavior of the samples, response and recovery times were calculated as the time needed to reach 90% of the total response, or to recover 90% of the baseline, respectively.

CHAPTER 3

NANOSTRUCTURED DEPOSITION OF TUNGSTEN OXIDE AND SYNTHESIS

3 Nanostructured deposition of Tungsten Oxide and synthesis

In this doctoral thesis, the author deployed different deposition techniques based on the bottom up approach like sputtering (RF), sol-gel synthesis and AACVD. The different deposition and synthesis techniques create different nanostructure morphologies. In this doctoral thesis above mentioned three different techniques have been deployed in order to achieve different metal oxide nanostructures especially for WO_3 which is the main candidate for the sensing layer due to its excellent chromic properties [Granqvist 2000]. The main characterization techniques used in this doctoral thesis for structural and morphological analysis are XRPD, Raman, UV-Vis-NIR spectroscopy, ESEM, EDX and AFM. These techniques provide useful information on the morphology, crystalline structure, stoichiometry and composition of the developed nanostructures and thin films. The main results obtained using these techniques for the characterization of structural and morphological analyses are also discussed in this chapter.

3.1 Growth of WO_3 thin films

3.1.1 Growth of WO_3 with RF magnetron sputtering

Sputtering is a popular and well-known technique to deposit metal oxide films. In this technique, the WO_3 nanostructured thin films were deposited onto the substrates due to the oxidization of the W atoms ejected from the metal target resulting from the collision with the ionised gas particles in the vacuum chamber at a suitable pressure. The gas ionisation in the sputterer can be generated either in direct current (DC) or radio frequency (RF) modes. As studied in the literature [Khatko 2007], that the different deposition conditions (e.g. annealing temperature, annealing time and substrate temperature during deposition) for the preparation of WO_3 using Sputtering technique influence the sensitivity and selectivity of the sensor. The substrate type and film thickness are also some important factors. Herein, we will discuss briefly different experimental parameters influencing growth of WO_3 thin films studied in literature.

Starting from the substrate temperature, it plays a vital role in surface area (grain size) and sensitivity of WO_3. The sensitivity and surface area increase has been reported with the increase in the deposition substrate temperature [Kim 2000].

Oxygen percentage in the sputtering gas has strong influence on gas sensing as reported by [Bendahen 2004]. Also previously done work in our department of Electrical engineering, the sensors fabricated with 50% of O_2 showed the highest responses and a decrease in grain size and an increase in roughness in comparison with films deposited with 18 % and 65% of O_2 [Vallejos 2007].

In this project, the RF sputtering is mainly used because it is more common for oxide films deposition and flexible fabrication parameters as compared to the DC. A 99.95% tungsten target which was 4 inches in diameter was utilized for the deposition. The modification of the nanostructured WO_3 deposited onto quartz substrate was performed in an ESM100 Edwards RF magnetron sputtering system with a planar magnetron cathode and a rotatable substrate holder. In the current work we used following optimum conditions studied in the literature and our previously done work. These conditions are described in the table 3.1 thin films with the thickness of 550 nm has been grown.

Tabla 3.1. Experimental parameters used during the growth of WO_3 thin films with Rf magnetron sputtering

No	Parameter	Specification
1	Target to substrate distance	7.0 cm
2	Sputtering power	200 W
3	Process gas	O_2 / Ar (1:1)
4	Process pressure	0.5 Pa
6	Substrate temperature	Room temperature

The annealing process aims to stabilize the structure, optical and electrical properties of WO_3 thin films. All the as-deposited WO_3 thin films went through the annealing procedure. The full annealing process was performed into furnace from Carbolite model GHA, max.temp.1473 K. The temperature of the annealing process was slowly raising with a rate of 293 K/min until it reached the desired annealing temperature. This temperature was held for 2 h in order to complete the oxidation process. It was then slowly cooled down until reaching the room temperature with natural convection. WO_3 functional properties may be significantly enhanced by structuring film morphology and by improving crystallographic texture of the film grains [Blackman 2005, Ashraf 2008].

It was observed that WO_3 films are amorphous in the temperature range from 423 to 573 K. It has been already reported an improvement of crystallinity and increase of grain size in WO_3 films when annealed at 773 K by several authors [Depero 1996, Gorokh 2006, Washizu 2003]. WO_3 films were then annealed in ambient atmosphere for 2 h to different temperatures starting from 423 to 973 K.

The deposition of Pt nanoparticles (NPs) on the WO_3 thin films has been performed using the spin coating technique. The Pt NPs, with average diameter of 10 nm, have been synthesized with the polyol method [Herricks 2004]: a solution 80 mM of Chloroplatinic acid hydrate (H_2PtCl_6) in ethylene glycol was added to a solution of poly(vinyl pyrrolidone) 30mM and Sodium nitrate ($NaNO_3$) with a ratio $NaNO_3$/ H_2PtCl_6 of 9 in ethylene glycol, at 433 K. Then NPs were dispersed in ethanol leading to a 30 mM solution. Pt NPs deposited samples were heated after the deposition at 473K during 30 min.

3.2 Structure, morphology and microscopic characterization of WO_3 thin films

3.2.1 Crystalline structure of WO_3 thin films

3.2.1.1 Phase Identification

We have investigated structural properties of WO_3 by XRPD to identify the crystalline phase and degree of crystallinity and its possible phase modifications, due to the temperature of annealing. The XRPD patterns are shown in Figure 3.1; as it can be observed the crystalline phase is obtained when the temperature of annealing is 773 K.

The binary W-O system is rather complex with a large number of stoichiometric compositions. The trioxide, WO_3 can crystallize in many polymorphs with various crystal structures [Depero 1996]. It can be found in literature, that the most stable WO_3 crystallographic phase at room temperature is the monoclinic structure ($P2_1/n$), but this phase transforms to triclinic, orthorhombic or a tetragonal phase at higher temperatures [Salje 1975]. At annealing temperatures higher than 623 K, usually is expected to crystallize in the monoclinic phase [Salje 1975]. Increase of crystallinity and increase of grain size were observed at 773 K by several authors [Washizu 2003, Patel 2009, Joraid 2007]. In our current study, improvement in the crystallinity was observed for temperatures higher than 623 K.

The crystalline phase observed belongs to the monoclinic system with the space group $P2_1/n$, taking into account the presence of the peaks (002), (200), (020) as shown in Figure 3.1. This can be identified using the ICCD 83-0950 pattern ($P2_1/n$, unit cell of this pattern: a = 7.300 Å, b = 7.538 Å, c = 7.689 Å, β = 90.892º). The peaks mentioned above most probably belongs to monoclinic crystalline structure but looking into the details of other ICCD patterns, such as ICCD-020-1323 (WO_3,P-1, unit cell of this pattern: a = 7.300 Å, b = 7.52000 Å, c = 7.69000 Å, α = 88.83º, β = 90.91º,γ = 90.93º) and ICCD-05-0388 (WO_3, P4/*nmm*, unit cell of this pattern: a = 5.25000 Å, c = 3.91000 Å, z = 2), as the possibility of mixture of different crystalline phases has been reported by A. G. Souza-Filho et al. [Souza-Filho 2000]. This could be the case in our thin films In order to confirm this, we anneal the films to 873 K and 973 K in order to see any phase transformation but as clear from the figure 4.1 there is no change in the phase observed.

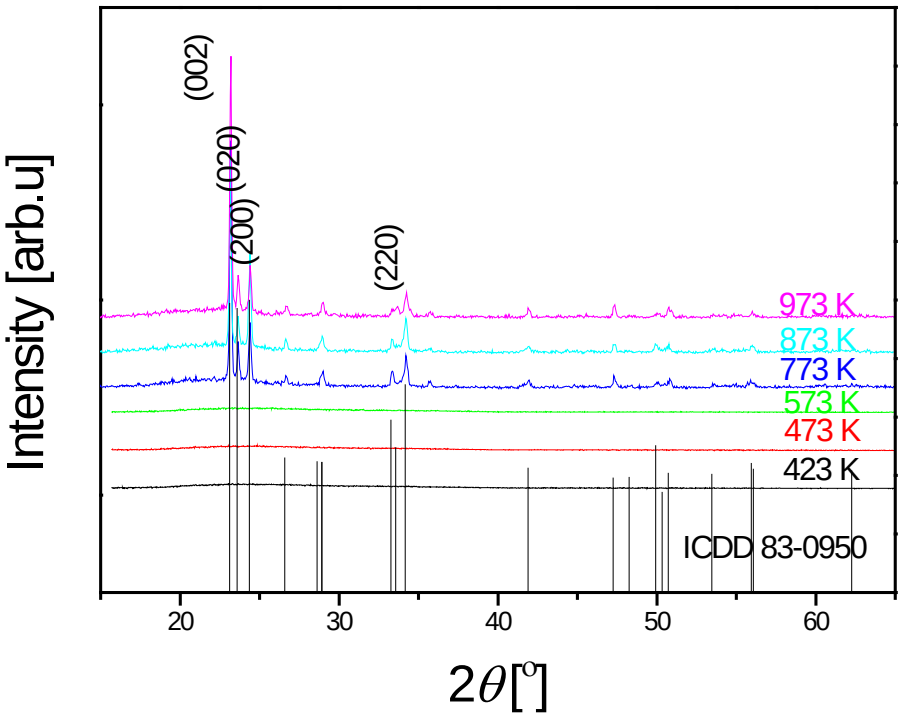

Figure 3.1. X-ray powder diffraction patterns of the WO_3 films annealed at the temperatures ranging from 423 K to 973 K.

It can be also pointed out the absence of texturing in the film, no preferential orientation, as expected due to the amorphous nature of the substrate. The WO_3 films annealed in the temperature range from 423 to 573 K are amorphous.

The structural characterization of WO_3 thin films decorated with Pt were conducted in the same way as mentioned above. Due to the small size (below 100 nm) and low concentration of Pt there is no noticeable peak in XRPD graphs so they are the same shown in the figure 4.1 for the samples annealed at 773 K and above.

3.2.1.2 Unit cell parameters and grain size

As mentioned, the crystalline phase observed belongs to the monoclinic system with the space group $P2_1/n$, taking into account the presence of the peaks which can be identified using the ICCD 83-0950 pattern. Unit cell parameters of WO_3 crystalline films obtained have been refined using program Fullprof [Rodriguez-Carvajal 1998], in which Rietveld method [Young 1995] is used. The parameters obtained using Fullprof program are a = 7.3110(16) Å, b = 7.543(18) Å, c = 7.694(16) Å and β = 90.925(84)°.

The grain size was estimated using Scherrer's equation and assuming spherical particles [Cullity 1978] in the three crystalline samples using the diffraction peak (002); the value obtained is around 70 nm of grain size in undoped WO_3 thin films.

3.2.1.3 Vibrational modes study

In order to understand the detail crystalline structure, Raman spectroscopy has been used in which μ-raman shift has been taken for the thin film of WO_3 samples annealed at 773 K. In the Raman spectra of WO_3, for the temperature range for the measurements is set from 373 K to 673 K as shown in figure 3.2, the phonon peaks may be grouped in a set of two ranges: high at 600–900 cm^{-1} and low at 30–400 cm^{-1}.

The transformation of the phase from monoclinic to tetragonal structure can be observed following the evolution of the low frequency bands (up to 100 cm^{-1}) of the Raman spectra; they correspond to lattice modes of vibrational nature and are particularly responsive to the transitions between the low symmetry phases of WO_3, which involves mainly collective reorientations of the basic WO_6 octahedral units. The phase transition can be monitored, in particular, by following the relative intensity decrease of the 34 cm^{-1} peak (typical of the monoclinic phase) and the simultaneous increase of the 41 cm^{-1} peak (typical of the triclinic phase) [Cazzanelli 1999]. Due to the possible mixing of different crystalline structures as discussed in section 3.2.1.2, no peaks had been observed below 100 cm^{-1}. So, we clearly rule out the possible multiple crystalline phase present in our WO_3.

Table 3.2 shows the phonon modes of tungsten observed with µ-raman. Raman bands of the transition metal (W) oxide in the range 950 - 1050 cm^{-1} can be assigned to a symmetric stretching mode of short terminal W=O bands, υs (M=O terminal). The W=O terminal stretching belongs to the W-O bonds at the free surface of internal grains. Relative intensity of the double W=O bond, typical of non bridging oxygen, is caused by the absorbed water molecules and is frequently seen in sputtered or evaporated films deposited at lower temperatures [Weckhuysen 2000, Daniel 1987].

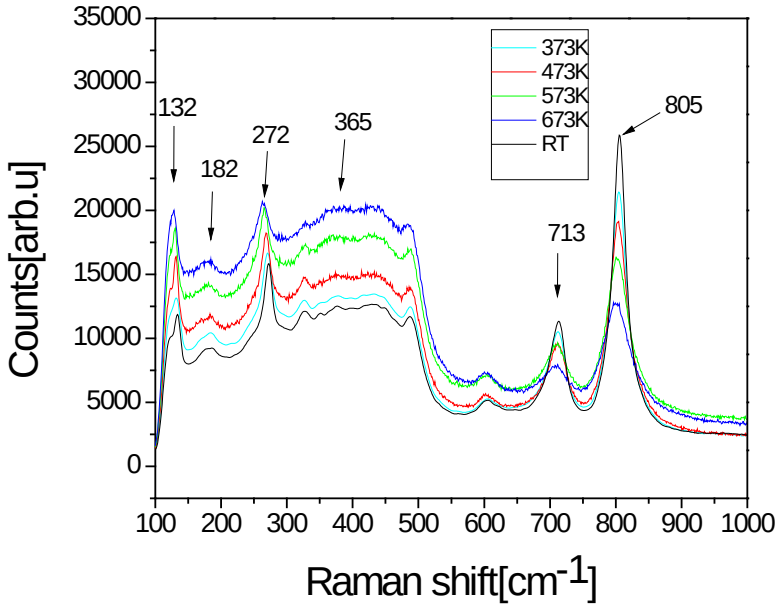

Figure 3.2. µ-Raman shift taken in the temperature range from 273 K to 673 K.

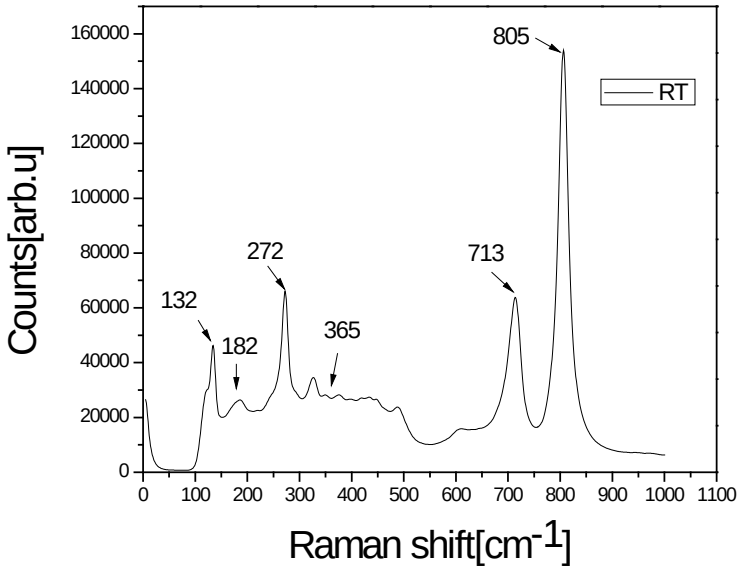

Figure 3.3 μ-Raman shift extended below 100 cm^{-1}.

The bands in the range 750 - 950 cm^{-1} are attributed to either the antisymmetric stretch of W-O-W bonds (i. e., υ_{as} [W-O-W]) or the symmetric stretch of (-O-W-O-) bonds (i.e., υ_{s} [-O-W-O-]) [Weckhuysen 2000]. Raman bands at 805 and 713 cm^{-1} corresponding to the stretching vibrations of the bridging oxygens, were also recorded by Daniel *et al.* [Daniel 1987]. The peak located at 806 cm^{-1} is typical Raman peak of crystalline WO_3 (monoclinic-phase), which corresponds to the stretching vibrations of the bridging oxygen [Tagstrom 1999]. This peak is assigned to W-O stretching (υ), W-O bending (δ) and O-W- O deformation (γ) modes respectively [Daniel 1987, Shigesato 1991].

Table 3.2 Raman modes for WO_3 film prepared with RF magnetron sputtering.

Raman shift [cm^{-1}]	Assignment	References
805	υ (O-W) δ (W-O) γ (OW- O)	[Daniel 1987, Shigesato 1991]
713	υ	[Nishide 1995]
365	δ	[Nishide 1995]
272	υ (O-W-O) δ (O-W-O)	[Daniel 1987]
182	-	[Bange 1999]
132	-	[Nishide 1995]

Stretching vibrations (υ), in-plane bending vibrations (δ) and out-of plane wagging (γ) modes

The Raman band centered at 346 cm^{-1} can be ascribed to the n(W-OH_2) vibrations. The band at 270 cm^{-1} can be assigned to δ (O-W-O) vibrations. The Raman peaks at 143 cm^{-1}, 643 cm^{-1} and 680 cm^{-1}, which are characteristic of the low temperature monoclinic phase, have not been observed [Nishide 1995, Bange 1999].

3.2.2 Surface morphology of WO_3 thin films

The surface and structural morphology of WO_3 thin films were examined by AFM. A porous surface with small grain size is recommended for better gas sensitivity [Shimizu 1999]. For sensing purposes, polycrystalline and small grains are advantageous because they lead to films with high surface area for the gas to interact with [Moseley 1987]. On the other hand, a free smooth surface is desirable to obtain better optical response.

3D AFM images of the crystalline films annealed at temperatures ranging from 773 K to 973 K are presented in figure 3.4. The surface is made up of grains and voids with dimensions in the range of nanometers. The presence of these voids within the film structure is favorable because they provide direct conduits for gas molecules to flow in from the environment. It can be observed that the grain size of the WO_3 was found to depend on the annealing temperature this effect was also reported by joraid at al. [Joraid2007]. By increasing the annealing temperature, the surface roughness is increased as indicated by a higher RMS value of the roughness shown in the table 3.3, these roughness values are in the range of 40-90 nm. The average grain size found with AFM of three different samples is 67 nm, which agrees well with the value obtained by XRPD. The growth of crystallites, observed to be vertical, could be related to the low rate of atom mobility on surface of the substrates.

Table 3.3 Surface morphological analysis of different samples annealed on different temperatures using AFM.

Sample	I	II	III
Annealing temperature [K]	973	873	773
RMS [nm]	90.66	44.76	42.17
Average roughness [nm]	85.01	43.23	40.32
Average height [nm]	96.44	53.55	49.20

Furthermore, different regions of the sample annealed at 773 K were observed in order to analyze the homogeneity of the sample. This can be seen in figure. 3.4 b, showing the AFM images of three different regions of the sample; it can be observed that the samples are quite homogeneous.

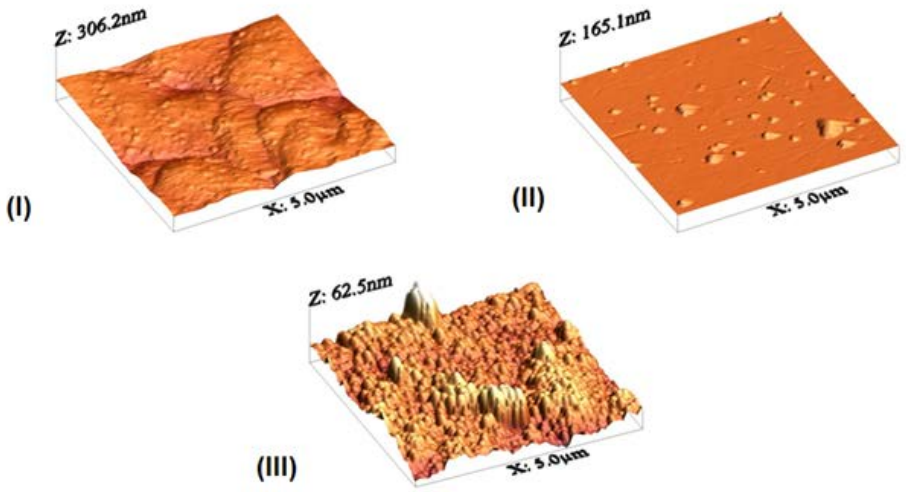

(a)

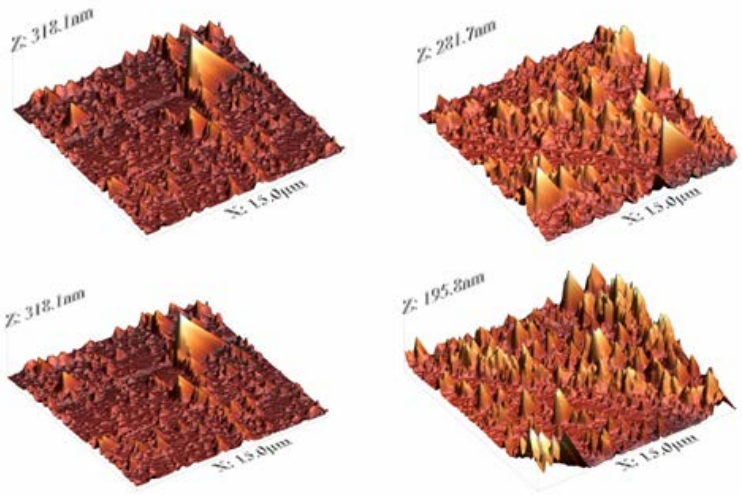

(b)

Figure 3.4. (a) AFM micrographs of three different samples annealed from 773 K to 973 K temperatures I. annealed at 973K, II. annealed at 873 K and III. annealed at 773K, (b) AFM image of the sample III taken for the different zones.

3.2.3 Surface morphology of Pt/WO_3 thin films

Surface morphology has been studied using ESEM microscope the images shown in the figure 3.5 (a) shows the compact and homogeneous morphology. The samples decorated with Pt shows nano-particles in the range of nanometers. The nano-particles are visible as bright spots in the images. When particles are spherical, the size aspect usually considered is the diameter. In the Figure 3.5 (b) from the ESEM images the size of the nano-particles has been estimated using the software iTEM. The nano particles are expected to yield lognormal size distributions [Granqvist 1976, Soderlund 1998]. The size histograms of our nano particles on WO_3 thin films are well represented by a lognormal distribution. We fit the log distribution by the lognormal function given by distribution by the lognormal function given by:

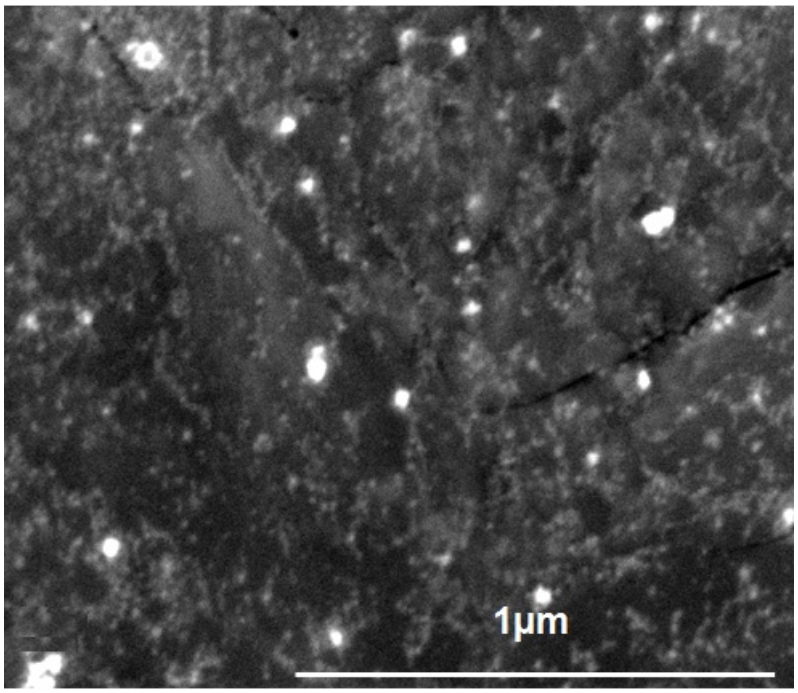

Figure 3.5 ESEM images WO_3 films coated with Pt deposited via spin coated and synthesize using polyol method.

$$N(d) = A \exp [-(\log d - \log d_0)^2 / 2\sigma^2] \qquad (3.1)$$

where N(d) is the number of particles with a determined width(d), A is the amplitude of the mode, d_0 is the mean of the studied parameter (width), and σ is the standard deviation of the mode (2σ is the dispersion of the mode). The fits were done directly on the histogram data, and the results are summarized in figure 3.6. As from the figure 3.6

we have an average size of 44 nm for the Pt nano-particles with the standard deviation of 0.43.

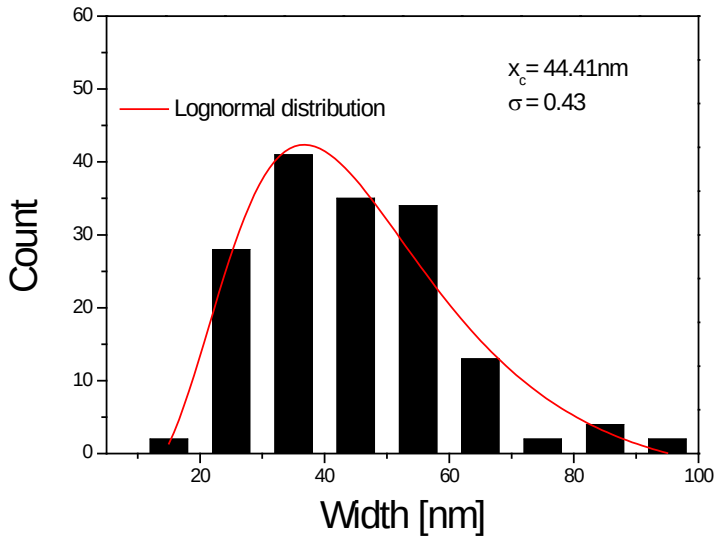

Figure 3.6. The particle size distribution of Pt nano particles on WO_3

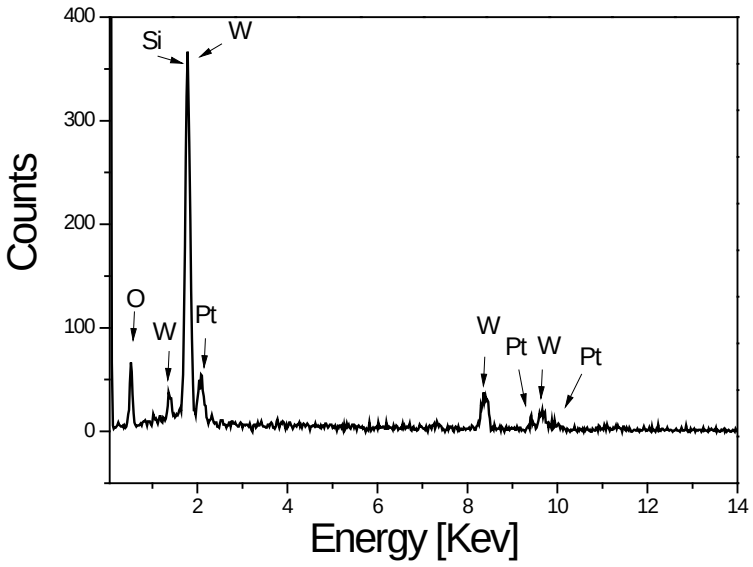

Figure 3.7. EDX spectrum of the WO_3 films decorated with Pt NP's.

EDX analysis of the Pt/WO_3 films on quartz substrates verified the presence of the elements on the films. Strong peaks of W and O indicated that films mainly consisted of WO_3. Low intensity peaks of Pt clusters are in agreement with their small amount deposited on the films shown in figure 3.7. The presence of silicon (Si) is caused by the

quartz (SiO_2) substrates, respectively. The EDX analysis also indicates the overlapping peaks for W and Si elements.

3.3 Growth of WO_3 nanocrystals by Sol-Gel: the modified Pechini method

3.3.1 Preparation of the precursor polymeric resin

The modified Pechini method was used to synthesize WO_3 nanocrystals. The experimental method is represented in a schematic diagram in figure 3.1.

Stoichiometric amounts of the $(NH_4)_2WO_4$ were first converted to their nitrate forms by dissolution in concentrated HNO_3. Later, the excess solution was removed to obtain nitrate precipitates by slow heating. It was dissolved in concentrated HNO_3. Afterwards, the nitrate solution totally evaporated. Throughout this step, the elements were mixed atomically.

The precipitate was then dissolved in concentrated EDTA solution (99.9%), governed by the C_M ratio. We then added ethylene glycol to produce a sterification, governed by the C_E ratio. The resin formation takes place at 363 K; during this reaction the resin becomes a gel. Afterwards, going on with the heating, the resin is dried.

3.3.2 Preparation of the nanocrystals

Herein we demonstrate the synthesis of WO_3 powder prepared by the modified Pechini Method, as described previously for other oxide, transparent materials. The starting oxide reagent was $(NH_4)_2WO_4$. The W^{6+} cation is having the same charge than in WO_3, desired product. EDTA was using as a chelate agent, with a ratio C_M=1. The PEG was used as a polymeric agent, with a C_E= 2. A flow chart of the procedure for preparing the WO_3 using the modified Pechini method is shown in Figure 1. The Pechini method uses the ability of organic acids to form polybasic acid chelated with several cations. Chelation, or the formation of complex ring-shaped compounds around the metal cations, then takes place in the solution. EDTA was used as the chelating agent. Metals W^{6+} ions are chelated by the carboxyl groups and remain homogeneously distributed in the polymeric network.

The time and temperature of the calcination procedure affects the size of the grain. Powders prepared at the lowest temperature have the smallest crystallite size. At higher temperatures, the rates of crystal growth and molecular diffusion are enhanced,

which fuses the small aggregated crystallites. This leads to the formation of well-defined crystals. By controlling the temperature and duration of the calcination it is possible to control the crystallite size and crystalline phase of the obtained powder.

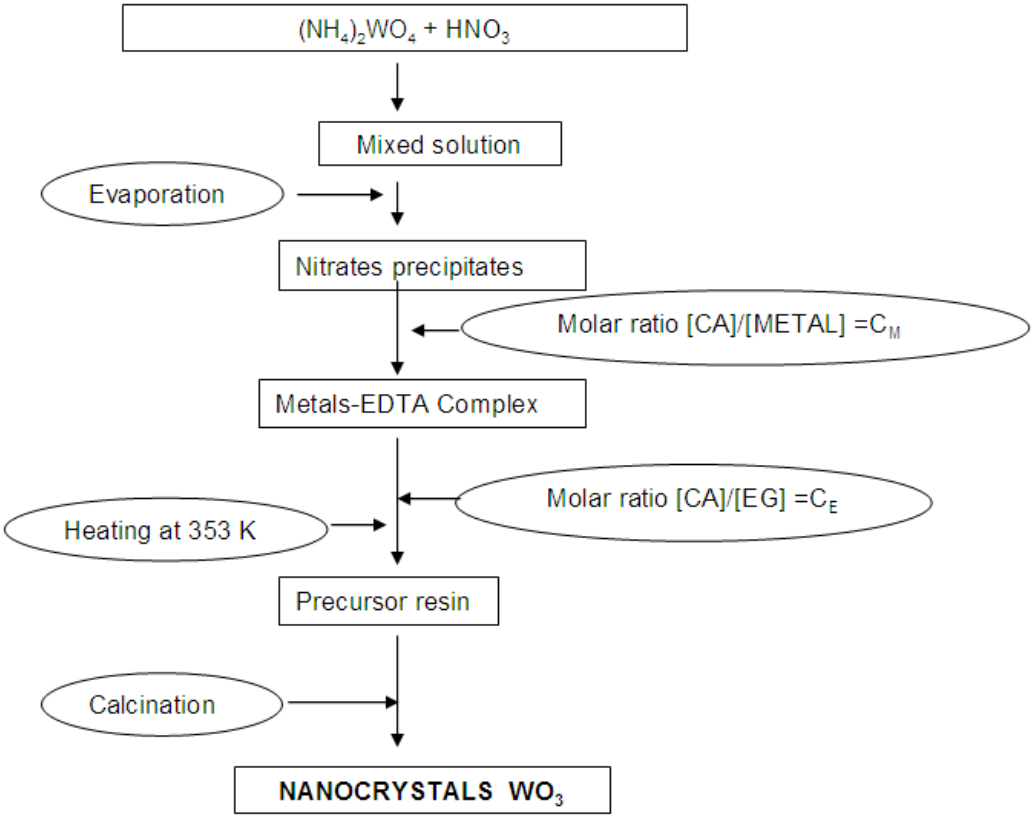

Figure 3.8. Process flow chart of different steps involved in the synthysizing of WO_3 nanocrystals by modified pechini method

3.4 Structure, morphology and microscopic characterization of WO_3 nanocrystals

3.4.1 Crystalline structure of WO_3 nano-crystals

The WO_3 nanocrystals grown with Sol-gel modified Pechini method were characterized the same way as other samples. First, to study the crystalline phase development as the calcination temperature and time increase, the precursor powder was calcinated at

air atmosphere and at various temperatures up to 823 K. Crystalline phase analysis was then carried out using XRPD.

Figure 3.9 shows the XRPD patterns of the precursor powder after the calcination step at 873 K temperature at different times. The crystalline phase of the crystallites has been checked by X-ray diffraction, confirming that they belong to the monoclinic phase, space group $P2_1/n$ (the peaks have been indexed according to the monoclinic WO_3 phase, ICCD 83-0950). According to this approach, the optimum calcination temperature must be between 723 K and 1003 K. At around 873 K, the WO_3 powder crystallized without any important secondary phase. We can see that the crystallinity of the nanocrystals improved, through the sharpness of the diffraction peaks, when the calcination temperature increases. On the other hand, an increase in calcination temperature led to an increase in the size of the nanoparticles.

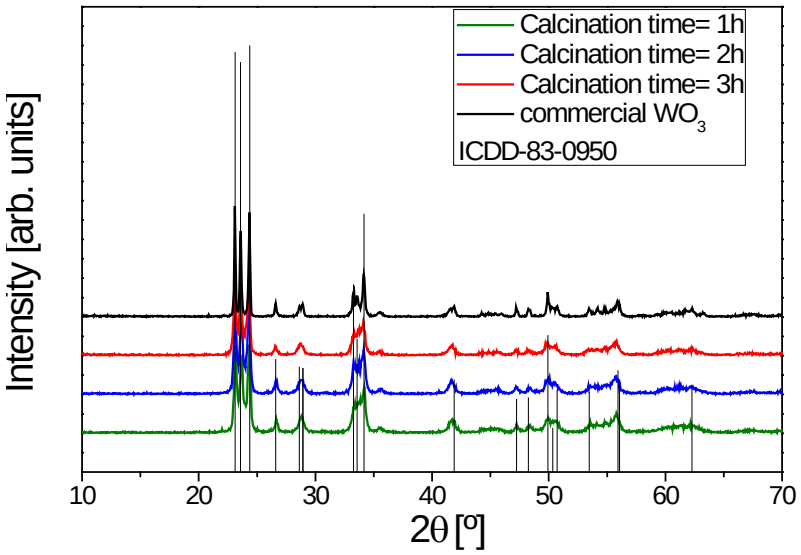

Figure 3.9 X-ray powder diffraction of the obtained WO_3 nanocrystals.

3.4.2 Morphological study of WO_3 nano-crystals

The morphology, homogeneity, and particle size were observed by electronic microscopy. It can be observed that the nanocrystals display an irregular shape and good homogeneity, but they build aggregates. During the calcination procedure, most of the particles aggregated into these large-size particles (tens or hundreds of nanometers). This may be due to the strong Van der Waals surface interactions among

the nanoparticles due to their high surface energy. Figure 3.10 a-c shows a collection of ESEM images of the nanocrystals with increasing the time of calcination at 873 K. Apparently the increase from 1h to 3h of calcination time does not imply an important increase of the particle size, on the contrary there is a slight improvement in the homogeneity of the size of the nanocrystals. Figure 3.10 d shows the image of WO_3 commercial powder (Fluka, 99.9%) as a reference for comparison.

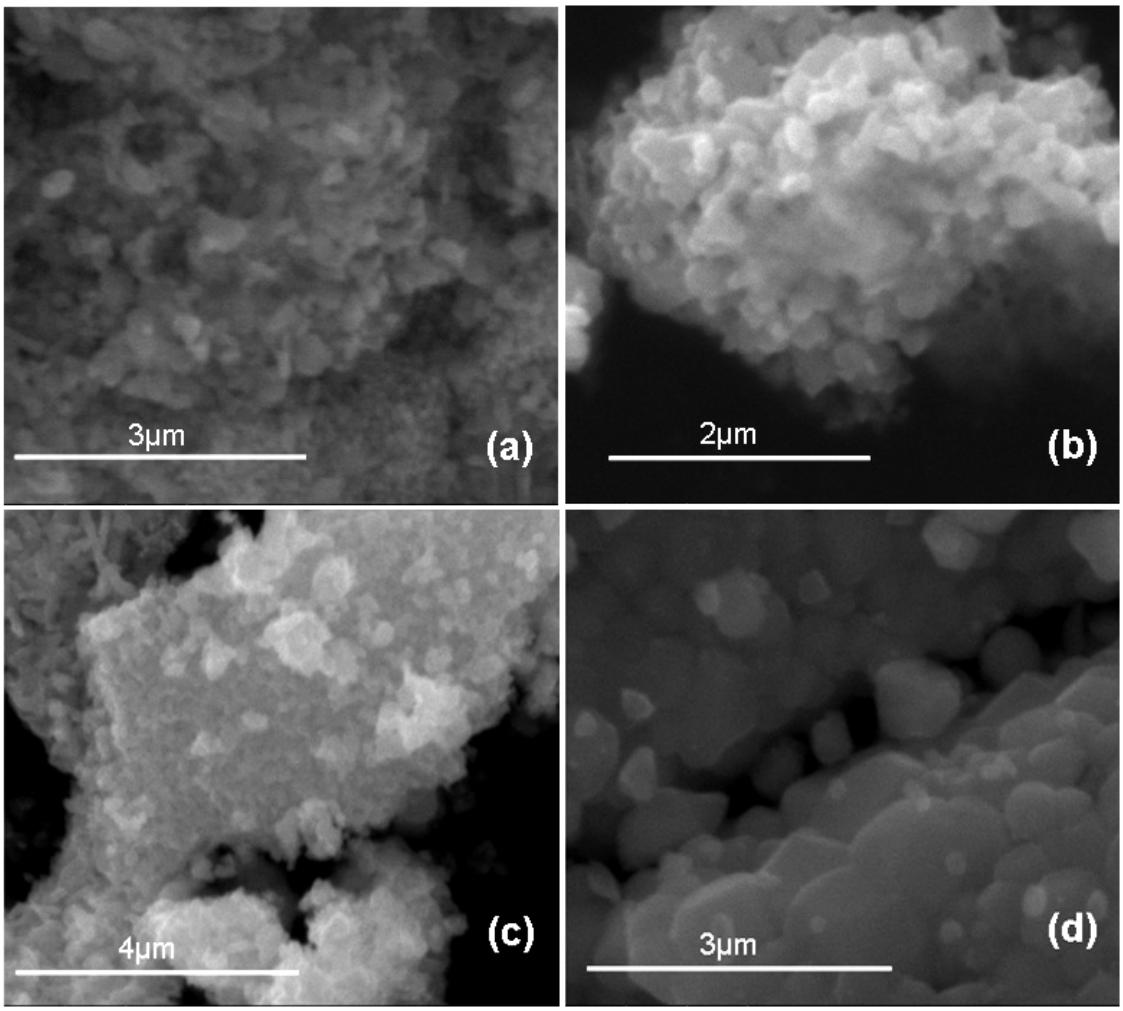

Figure 3.10 ESEM images of the obtained nanocrystals.

Information about the modified Pechini process for nanocrystal synthesis can be obtained by plotting particle size histograms. The size distribution for a collection of particles is based on a single aspect of the size, and, ideally, it must be related to the application [Feller 1992]. When particles are spherical, the size aspect usually considered is the diameter. Figure 3.11 (a) shows The TEM images of the obtained nanocrystals. In our case, we have used the nanocrystal width since they are generally

irregularly shaped. Nanocrystals formed by nucleation, condensation, and particle growth are expected to yield lognormal size distributions [Granqvist 1976, Soderlund 1998]. The size histograms of our nanocrystals are well represented by a lognormal distribution. We fit the log distribution by the lognormal function given by equation 3.1 from the section 3.2.3 obtained graph of the fit is shown in the figure 3.11 (b).

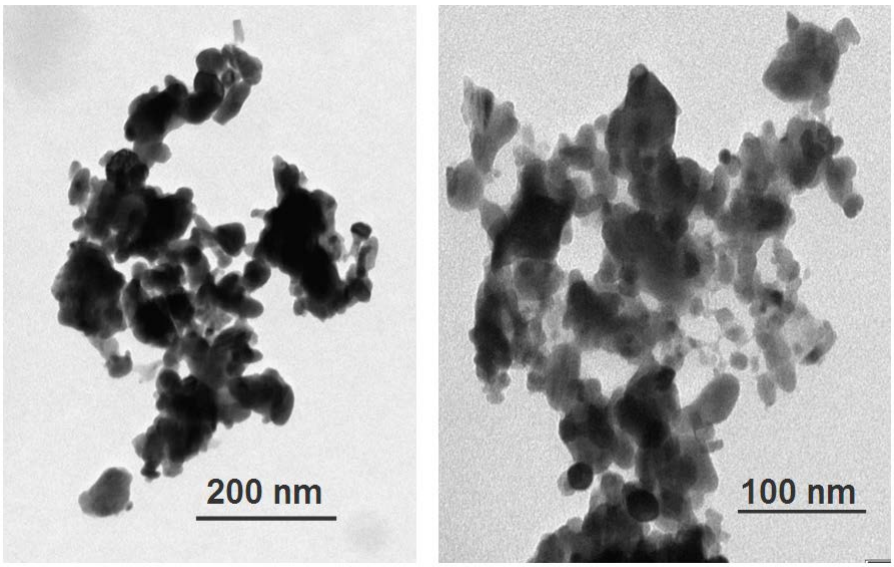

(a)

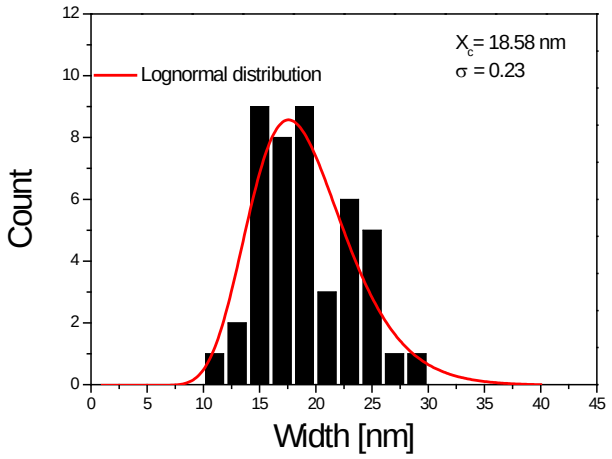

(b)

Figure 3.11 (a) TEM images of the obtained nanocrystals, (b) Histogram of the nanocrystals obtained

3.4.3 Specific area and porosity of WO_3 nanocrystals

The basic methodology to determine the surface area implies the determination of the quantity of an inert gas, usually N_2, required for forming a monolayer on the surface of a sample, at cryogenic temperature. The final area of the sample is calculated using an already known are to be occupied by a molecule of N_2 under the same conditions.

Some results that it can be found in literature for WO_3 nanocrystals prepared by sol Gel method: Brunauer–Emmett–Teller (BET) surface area measurement was that the specific surface area of WO_3-NC is 33.2 m^2g^{-1} and that of commercial WO_3-Aldrich and commercial WO_3-Alfa is 2.2 m^2g^{-1} and 1.2 m^2g^{-1}, respectively [Joshi 2011].

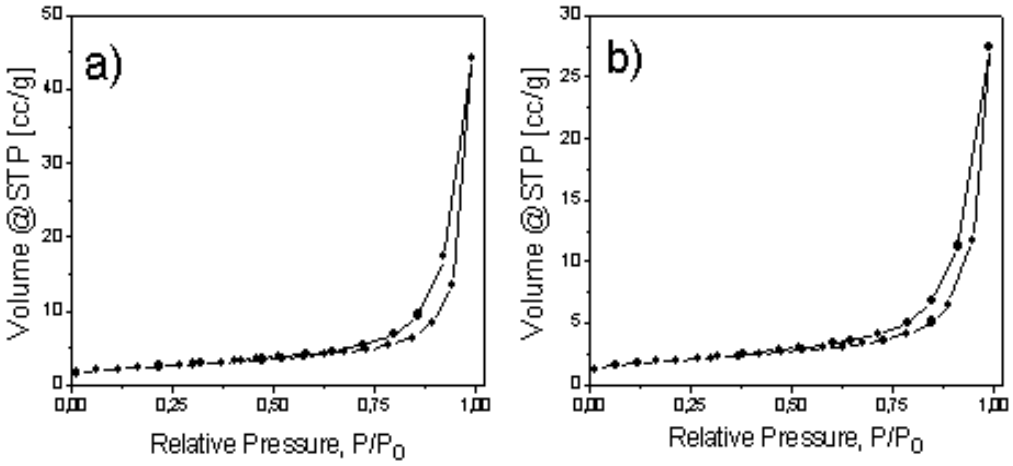

Figure 3.12 BET specific area, (a) before sonification, (b) after sonification.

In the present work, for the WO_3 nanocrystals synthesized by Pechini modified method the BET area measured was 8.643 m^2g^{-1}. N_2 gas adsorption/desorption isotherms were performed at 77 K and shown in figure 3.12.

The samples exhibit a type IV isotherm (following the IUPAC 1985 classification of physisorption isotherms), that indicates the presence of mesoporosity in the sample.

It can be observed a clearly adsorption hysteresis. The hysteresis loop, Type H3, is typical of aggregates of flat and broad particles or adsorbents containing slit-shaped pores [Rouquerol 2004]. In figure 3.13; it is reported the distribution of the size of the pores; as it can be observed the average is a value around 100 Å.

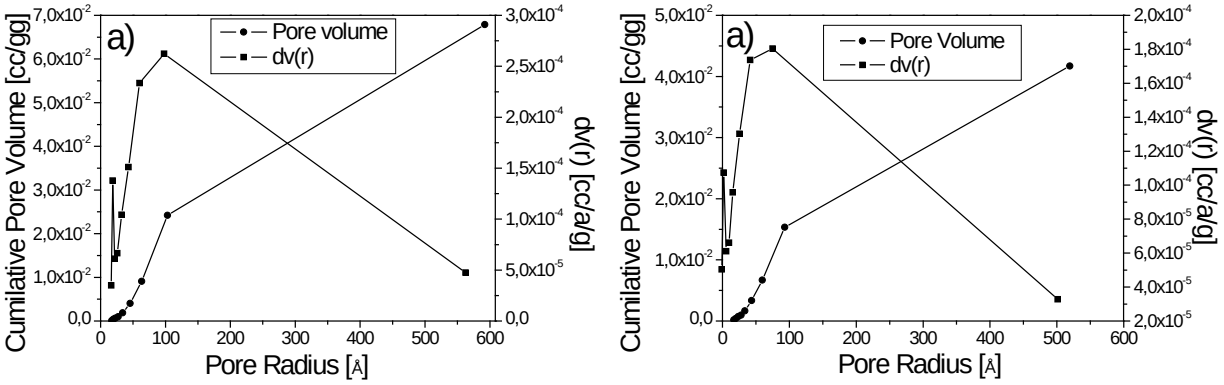

Figure 3.13 Pore size dispersion, (a) before sonification, (b) after sonification.

The measurement was repeated after the sample had underwent a process of sonification treatment, in order to break the possible agglomerates; but after this process the BET results were almost identical, there have been a slight reduction of specific area till 6.781 m²/g and the porosity is almost the same (figure 3.12 b and 3.13 b). Finally in both BET results, the C constant was higher than 80; assuring a good interaction of the N_2 with the material.

3.5 Growth of WO_3 nano-needles

We applied thin film deposition by aero sol-gel assisted chemical vapor deposition (AACVD) as a new method to deposit nano-needles of WO_3.

3.5.1 Growth of WO_3 nanoneedles on quartz substrate

We used AACVD for the deposition of WO_3 nano-needles a sensing layer on quartz substrate. Recently this method has been widely used in our department of Electrical and electronics engineering of URV to deposit WO_3 nano-needles on aluminium [Vallejos 2011]. In the series of our experiments to grow the nano-needles of WO_3, A piezoelectric ultrasonic atomizer was used to generate an aerosol (as mentioned above) from a precursor mixture (10 mg HAuCl4. $3H_2O$ (Sigma-Aldrich, 99.9%) in 5 cm^3 methanol (Sigma-Aldrich, Z99.6%) and 150 mg $W(OPh)_6$ (synthesized according to the literature [Cross 2003]) in 15 cm^3 acetone (Sigma-Aldrich, min. 99.8%) which was transported to the heated substrate by a nitrogen (Carburos Metàlicos, N_2 Premier) gas flow (0.5 $Lmin^{-1}$). Under these conditions the time taken to transport the entire volume of the solution, i.e. the deposition time, was typically 45 minutes to 60 minutes.

The typical experimental setup used is shown in the figure 2.6. The substrates were 10 mm x10 mm x 1 mm Quartz inter-digitated Pt electrodes (gap: 300 mm, thickness: 9 mm) on the surface and a Pt heater on the reverse we started with the experimental conditions used previously and described in the reference [Vallejos 2011]. This method requires precise control of the precursor super saturation to prevent formation of non-adherent powders or polycrystalline thin films. In this context the choice of precursors is crucial. This conventional method used by the department of Electrical and electronics engineering to grow nano-needles was on alumina substrate, so we have to precisely control the conditions and solvents, in order to obtain the nano-needles on quartz substrate. The different experiments done are shown in the table 3.4. We used different solvents and different substrate temperature.

Before every deposition the substrate was cleaned with ethanol (≥ 99.5 %, Scharlau) and then dried with synthetic air (≥ 99.99%, Premier). Subsequently, it was placed in the substrate holder into the reactor chamber, which was later securely closed. The deposition process was started after the reactor had reached the adjusted temperature. The nitrogen flow was introduced and then the atomizer was switched on. The aerosol was generated ultrasonically and nitrogen flow at constant rate of 0.5 l/min was used as a carrier gas. The intensity of the oscillations of the ultrasonic atomizer was set up only once and kept constant for all the depositions. By introducing nitrogen carrier gas to the atomized precursor solution the aerosol droplets were transported to the heated reaction zone, where the solution underwent evaporation and/or decomposition. The deposition of the active layer continued until all the precursor solution had passed through the reactor. After turning off the atomizer and the temperature process controller, the nitrogen carrier gas was allowed to flow until the deposited layer was cooled down to the room temperature and then the reactor chamber lid was taken off. The substrate was stored and handled in air before it was taken out for further analysis. The effectiveness of the deposition was tested under various conditions and changes in the solvents used, volume of the liquid precursor solution, deposition temperatures, rate of nitrogen flow and deposition time were investigated. The fused silica quartz substrate is used for all the depositions. Three types of organic solvents were tested (namely, acetone, toluene and methanol) in order to perform nano-needle-like deposition.

The influence of the different parameters involved (reactor temperature, gas flow, solvent, etc.) was systematically investigated. Therefore, one parameter was varied while keeping the other factors constant. This approach was repeated with all the

parameters, until the optimal conditions for the deposition were found. As a result, homogeneous and nano-needle-like structured films were deposited.

Tabla 2.4 The detailed list of the different samples gorwn by AACVD with the experimental values used during the growth

Samples	Temperature, °C	Precursor $W(OPh)_6$, mg	Solvent, mL	substrate	Deposition time minutes	Structure	N_2 flow, L/min
1	500	100	Acetone, 10 + Toluene, 10	Quartz	60	oriented Nano-grains	0.5
2	400	75 + Au(5)	Acetone, 12.5 + Methanol, 2.5		25	Nano-grains	
3	500	100	Acetone, 16 + Methanol, 4		50	Nanoneedles	
4	500	150	Acetone, 10 + Toluene, 10		60	oriented Nanoneedles	
5	400	100	Acetone, 10 + Toluene, 10		60	Nano-needles	
6	500	300	Acetone, 10 + Toluene, 10		60	oriented Nanoneedles	
7	350	150+Au10	Acetone, 16 + Methanol, 4		50	Nanoneedles	
8	500	300+Au 20	Acetone, 16 + Methanol, 4		60	Nanoneedles	
9	350	150+Pt	Acetone, 16 + Methanol, 4		60	Nanoneedles	

In order to deposit gold assisted nano-needles in the beginning a solution of noble metal precursors (gold (III) chloride trihydrate, [$HAuCl_4.3H_2O$], Sigma-Aldrich, 99.9 %) (0.67 mM) dissolved in methanol (2.5 mL) mixed with a solution of main precursor [$W(OPh)_6$] (0.67 mM) dissolved in acetone (12.5 mL). The quantity of this solution is then adjusted accordingly when the precursor is increased as can be seen in the table 3.4 for the samples 3, 7, 8 And 9.

These all films mentioned on the table 3.5 were annealed at 773 K temperature for 2 h, using a horizontal tube furnace (Carbolite model GHA, max.temp.1973 K). The temperature of the annealing process was slowly raising with a rate of 293 K/min until it reached the annealing temperature of 500 ºC. It was then slowly cooled down until reaching the room temperature with natural convection.

3.6 Structure, morphology and microscopic characterization of WO_3 nano-needles, Pt and Au nano-particles assisted WO_3 nano-needles

3.6.1 Crystalline structure of WO_3 nano-needles, Pt and Au nano-particles assisted WO_3 nano-needles

In order to identify the crystalline structure of the WO_3 nano-needles the XRPD measurements were made. A crystalline phase has been observed clearly for the pure WO_3 samples, with peaks assigned to the crystallographic planes of the $P2_1/n$ space group belonging to the monoclinic system referring to the ICDD card 083-0950. XRPD patterns are shown in figure 3.14 (a) and (b) for all the samples mentioned in the section 3.5.1. The grown structure is highly oriented in the (010) direction, when we have only nanograins. As we obtain nanoneedles, it shifts to the (001) orientation. This preferred orientation is similar to our previous results [F.E. Annanouch 2013, Vallejos 2013], also reported in a similar type of work done in a different lab [Palgrave2006]. Regarding to the XRPD of the Au nano particles assisted nano-needles, the XRPD patterns are shown in the figure 3.15 (a) and (b). The Au assisted nano-needles also belong to the monoclinic system with the space group $P2_1/n$ from the ICDD card 083-0950. The diffraction peak at 38.1841º 2θ was assigned to the (111) plane of Au.

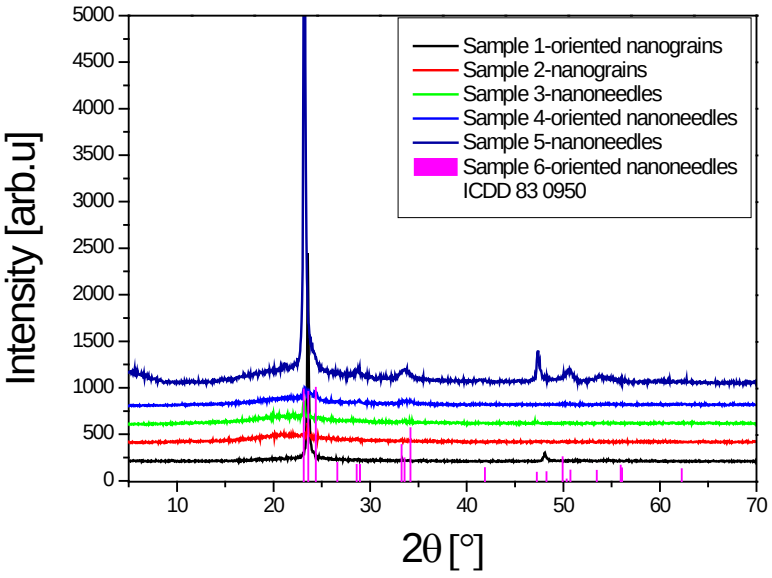

(a)

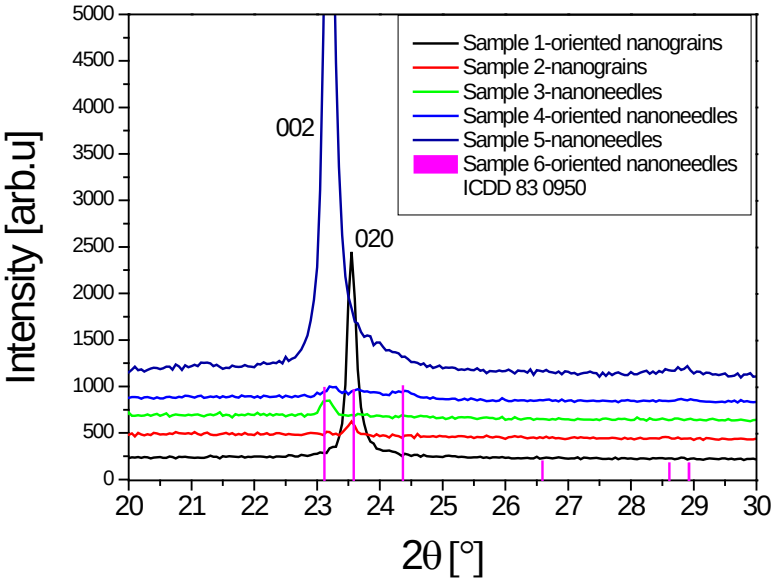

(b)

Figure 3.14 (a) X-Ray Powder diffraction graph of the different samples prepared by AACVD, (b)) zoom of XRPD to indentify orientations in the crystaline samples.

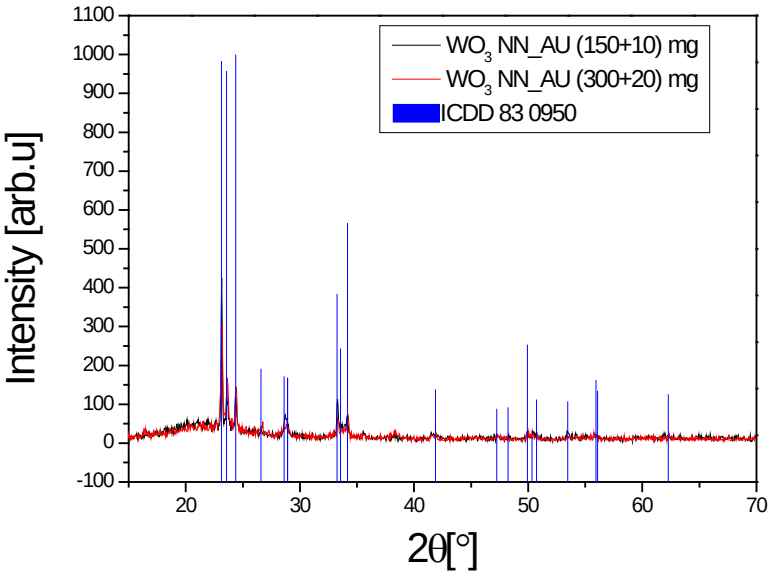

(a)

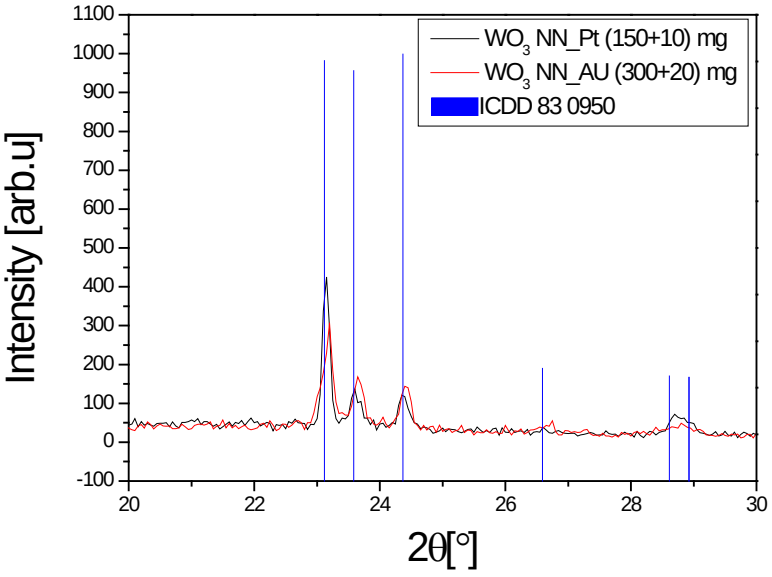

(b)

Figure 3.15 (a) and (b) X-Ray Powder diffraction graphs of the nano-needles decorated with Au nanoparticles

3.6.2 Surface morphological study of WO_3 nano-needles

We have investigated the structural morphology of WO_3 nano-needles using ESEM. The figures of the different samples described in table 3.4 of section 3.5.1 are shown in figure 3.16. In figure 3.16 a,b,c and d we showed the nano-needles obtained of the samples 3,4,5 and 6 mentioned in the table 3.4. In the second set of experiments described in detail in section 3.5.1 for the samples 7, 8 and 9 from table 3.4. The ESEM images are shown in the figure 3.16.

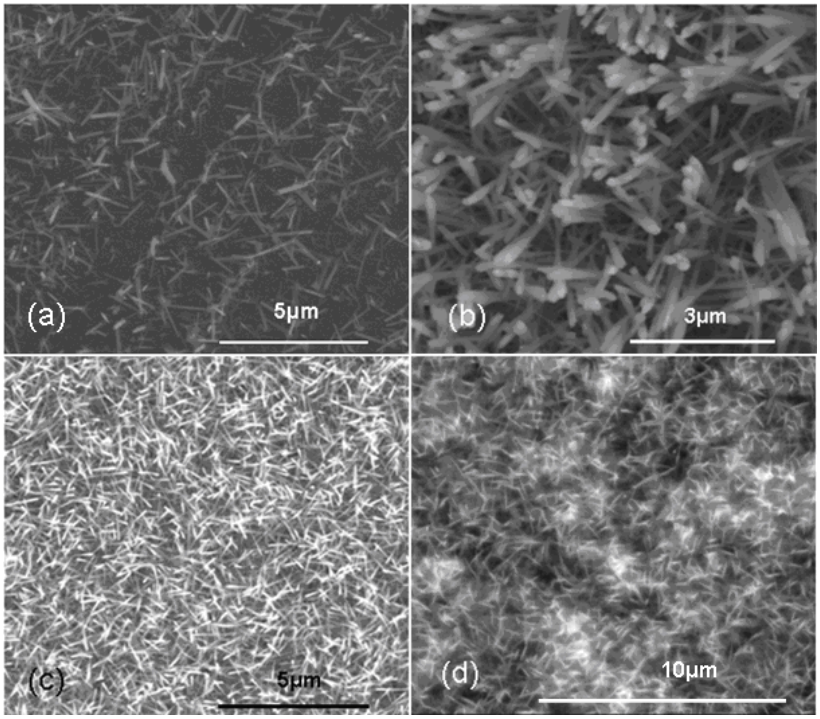

Figure 3.16 ESEM images of the nano-needles obtained in the different experiments as images a, b, c and d corresponds to the samples 3, 4, 5 and 6 respectively.

The highly dense non aligned nano-needles are present in all the shown images both bare and noble metal-decorated nano-needles have a uniform diameter as clearly shown in figure 3.17. This is consistent with our previous work on deposition of Au/WO_3 and Pt/WO_3 nano-needles [Vallejos 2013].

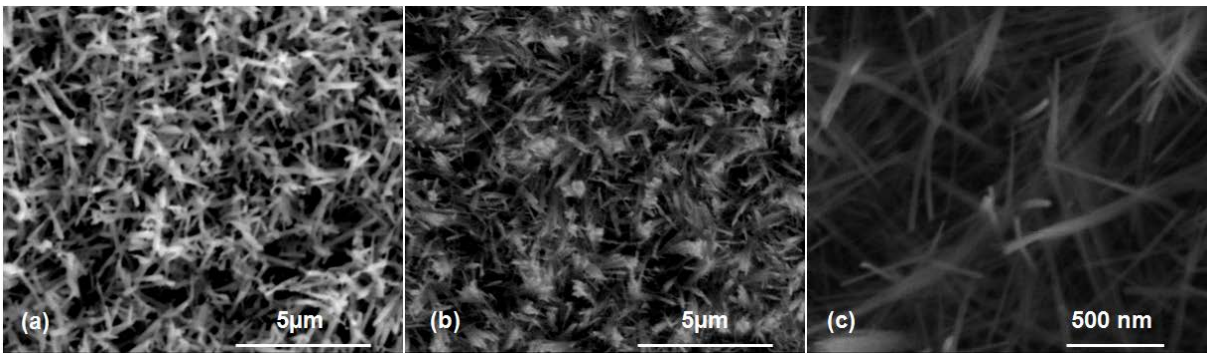

Figure 3.17 ESEM images of the sample 7,8 and 9.

In order to verify the presence of Au and Pt nanoparticles in WO_3 nanoneedles the EDX analysis of the WO_3 nano-needles on quartz substrates were conducted. The presences of the different elements on the films are verified. Strong peaks of W and O indicated the films are mainly consisted of WO_3. Low intensity peaks of Au nanoparticles are in agreement with their small amount deposited on the films shown in the figure 3.18 (a) and the presence of Pt nanoparticles in figure 3.18 (b). The presence of silicon (Si) is caused by the quartz (SiO_2) substrates. The EDX analysis also indicates the overlapping peaks for W and Si elements. These films contain 0.88% and 0.25% of Au and Pt nanoparticles as reported in our earlier work [F.E. Annanouch 2013].

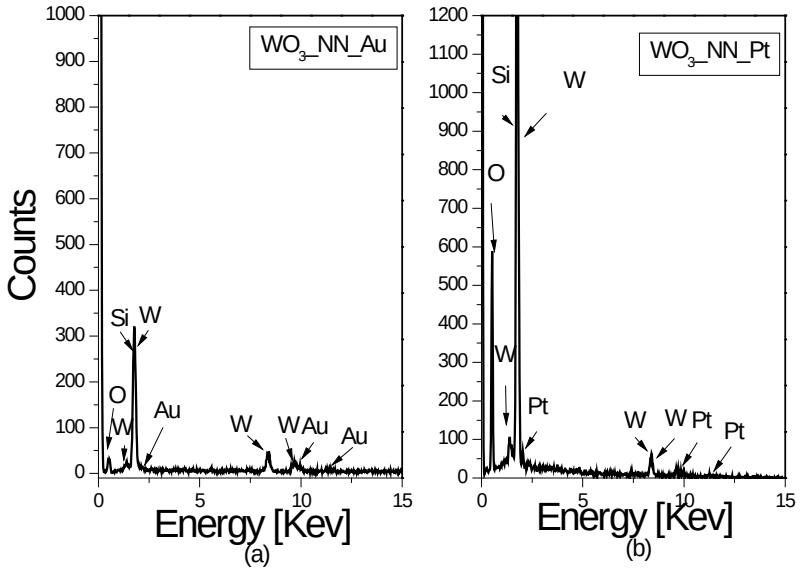

Figure 3.18 EDX spectrum of the WO_3 nano-needles, (a) assisted with Au, (b) assisted with Pt.

CHAPTER 4

OPTICAL CHARACTERIZATION AND GAS SENSING

4 Optical characterization and gas sensing

The micro-nano characterisation of the metal oxide nanostructures and thin films discussed in the previous chapter provides useful information in the understanding of the optical sensing performance of the materials. In this doctoral thesis, the nanostructured thin films were deposited on Quartz substrate. For optical gas sensing of the WO_3 deposited on transparent substrates, the optical gas sensing measurements are based on the absorbance spectroscopy.

4.1 Optical characterization of WO_3 thin films

In this doctoral thesis, the investigation of gasochromic behaviour of WO_3 are based on otical absorbance. The detail of the setup used is described in chapter 2. Herein, we start with optical characterization of WO_3 thin films prepared by RF sputtering discussed in detail in chapter 2. The thickness of the films of WO_3 was 550 nm for all the films. Also, as explaind in the section 3.2.2 the effect of smaller grain size improves the sensitivity. In figure 4.1 we can see the transmittance curves of WO_3 thin films annealed at different temperatures starting from 423 K to 973 K. Transmittance values in the visible- NIR region range in the interval 44% to 86%. The reflection losses (assuming an ideal flatness and not corrected in figure 4.1), calculated using a refractive index value of 2.25 are around 15%. The values of the transmittance at a specific wavelength of 700 nm, are summarized in Table 4.1 for better comparison.

The maxima and minima in the transmittance curve of these semitransparent films were ascribed to the optical interference that occurs in the sputtered WO_3, due to the multiple reflections of the light as it travels through the thin film. The disappearance of these maxima and minima for samples annealed at 973 K agrees with the increase in the roughness of the surface of the film by increasing the annealing temperature. As a result, the scattering increases in high temperature annealed samples and also, the interference process is less probable

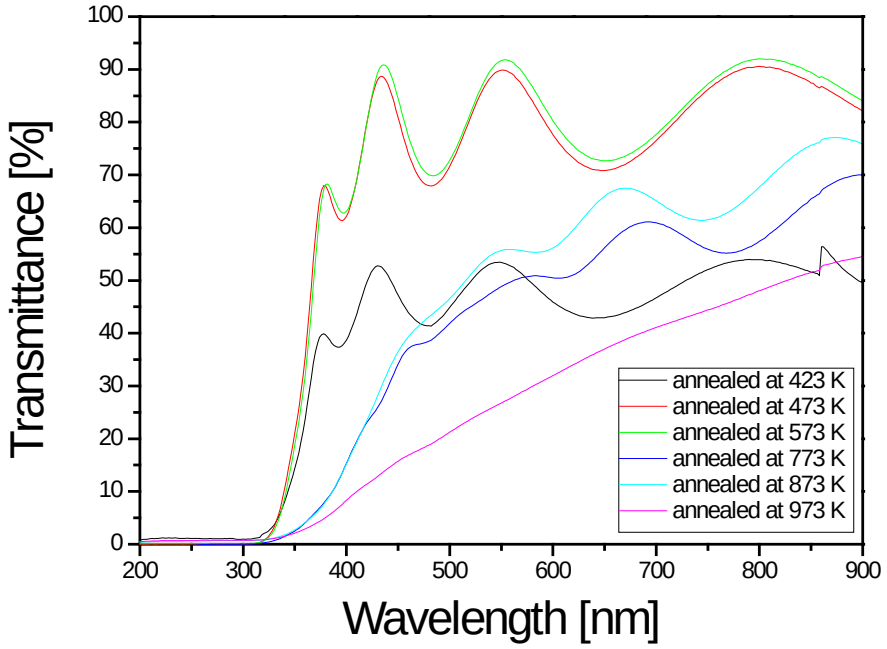

Figure 4.1 Transmittance measurements of the pure WO_3 films annealed in the range of temperatures from 423 K to 973 K.

Table 4.1 Transmittance values of the different WO_3 films annealed at different temperatures at 700 nm and at room temperature.

Sample	Annealing temperatures[K]	Transmittance[%] (at 700 nm)
III	773	61
II	873	65
I	973	41

The red-shift in the optical bandgap for the crystalline samples in relation to the amorphous ones is usually related to the increase of the oxygen vacancies in the crystalline phase [Migas 2010], Furthermore, the decrease in the transmittance is related to the increase in the roughness (increase of the nanocrystalline grain size) as evidenced from AFM measurements. As discussed in section 3.2.2 that icreasing the annealing temperature increases the surface roughnes, favouring the increases the sites for the gas adsorption ; and then improving the sensitivity for gas, however these

increase of roughness increases the difficulty in the optical measurements. So, the selection of the optimum annealing temperature is a compromise between these two contradictory behaviors.

4.2 Optical absorption of WO_3 thin films with H_2, NO_2 and CO gases

The undoped WO_3 thin films have been subjected to optical gas sensing tests by measuring the optical absorption of the thin films under the presence of the three different gases: H_2, CO and NO_x. Three different samples annealed at the temperatures of 773 K, 873 K and 973 K were tested. As the samples are homogenous (as observed by AFM), we expect that the measurement results are independent of the position of the optical spot at the surface of the sample. The films without noble metals were tested first at room temperature and at 423 K under the effect of gases. They did not show any detectable gas response at room temperature and at temperatures below 473 K. Thus, the operating temperature was set to 573 K.

Higher temperatures generate the appropriate oxygen surface species that will react with the gases, thus promoting an increase in sensitivity [Sahm 2006]. Examples of the measured absorbance spectra for WO_3 thin film samples with all the annealing temperatures and for the different gases are shown in figures A1.1 to A1.7 of Appendix A1. As it can be observed, very small difference in absorbance between the spectra can be recognized. The absorbance of a given sample exposed to the target gas and the absorbance of the sample exposed to air were compared to define response parameter as Optical Absorbance Change, ΔAbs:

$$\Delta Abs = Abs_{gas} - Abs_{Air},$$

The obtained ΔAbs for the undoped samples as mentioned above tested are shown in figure 4.2.

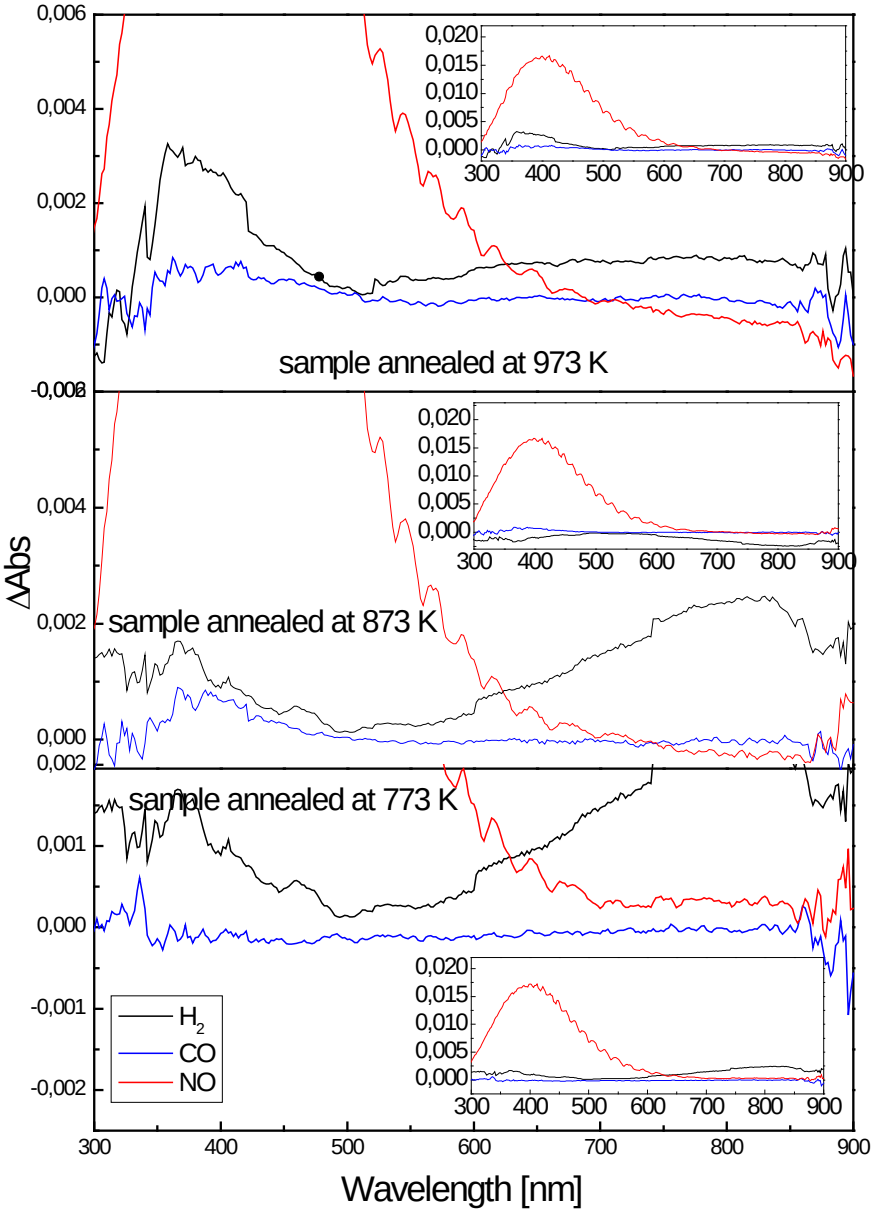

Figure 4.2 Optical Absorbance Change, ΔAbs = Abs $_{gas}$ – Abs $_{Air}$, curves of samples annealed at 773 K, 873 K and 973 K, for H_2, CO and NOx at operating temperature 573 K.

For the undoped samples, in all the ΔAbs spectra, a strong absorption peak appears near 400 nm for NO_x. This is due to residual presence of NO_2 in the test environment, which has a strong absorption in the range of 200 nm to 500 nm [Wojtas 2011]. As can be observed in figure 4.2, the maximum ΔAbs for each sample is in the presence H_2. The optical response of the samples to H_2 increased with the annealing temperature employed in their preparation. However, it can be observed that for each sample, the

optimum wavelength for detecting H_2 varies (around 800 nm, 550 nm and 400 nm for samples annealed at 773 K, 873 K and 973 K, respectively).

In the case of CO detection, the observed ΔAbs are small, but the tendency of an increase in the optical response with the increasing of the annealing temperature is maintained. Also, a blue shift of the wavelength value for optical detection is observed with the increasing of annealing temperature. The studied films show a notable change with NO_x, although it has to be taken into account the strong absorption of the non-adsorbed NO_2 in the chamber which may mask the optical properties change of the WO_3 in the range between 200 and 500 nm. Nevertheless, of a wavelength far from the absorption band of NO_2 is chosen, such as 700 nm, this effect is greatly reduced. At this wavelength the response to H_2 is noticeable while the response to CO is very small. It should be pointed out that the WO_3 films discussed here are undoped (i.e., not activated with any metal dopant) and working at 573 K. At such operating temperature they show an optical absorption change in the presence of H_2; which has not been observed in undoped TiO_2 at 673 K and 773 K operating temperatures [Nanba 1994].

In view of showing time resolved spectra as a way to analyze the dynamics of response and recovery cycles, and for the sake of simplicity, a single wavelength was chosen. The region of wavelengths ranging from 300 till 600 nm would not be valid to perform multiple gas sensing, due to the fact that the large absorption of NO_2 will mask the results. Instead, in the region of 700 to 800 nm, undoped materials show a significant response to H_2. Therefore, 700 nm was chosen for pure WO_3. This approach of using the same wavelength for detecting the presence of these gases; would lead to a response that is not specific for each gas, but could be used in to detect the presence of any of these gases in a mixture. So, this approach could be implemented in the future in a device for multiple gas detection. In the sub-plots of figure 4.3, the time resolved spectra fixed at 700 nm correspond to the dynamic responses of undoped WO_3 thin films under the presence of the three different gases studied. These subplots are for samples annealed at 773, 873 and 973 K respectively, all operated at 523K. The films respond with a square output signal to NO_x. The maximum change in the absorbance of the WO_3 films due to the presence of gas is near 3×10^{-4}, for the sample annealed at 973 K and for NO_x gas. This high sensitivity in this sample could be attributed to the higher roughness, increasing the specific area for the adsorption of the gas.

The initial air to NO_x transient was fast and in the range of 13 s till 25 s for the different samples studied; being the fastest for the sample annealed at 973 K. Shimizu et al. [Shimizu 1999] reported a response and recovery time of around 5-10 s when Pt-WO_3

was submitted to NO_x gas at 773 K, when performing impedance measurements. Also, it has to be highlighted that the baseline recovery time (when NO_x is replaced by air) is in the same range.

The observed drifting of the baseline observed in figure 4.3 (a) and figure 4.3 (c) could be related to the slow baseline recovery dynamics due to the also slow process of desorption of the reaction products formed at the active sites; the concentration of these active sites can be related to the amorphous/ crystalline structure of our samples [Sanders 1994,Buso 2008].

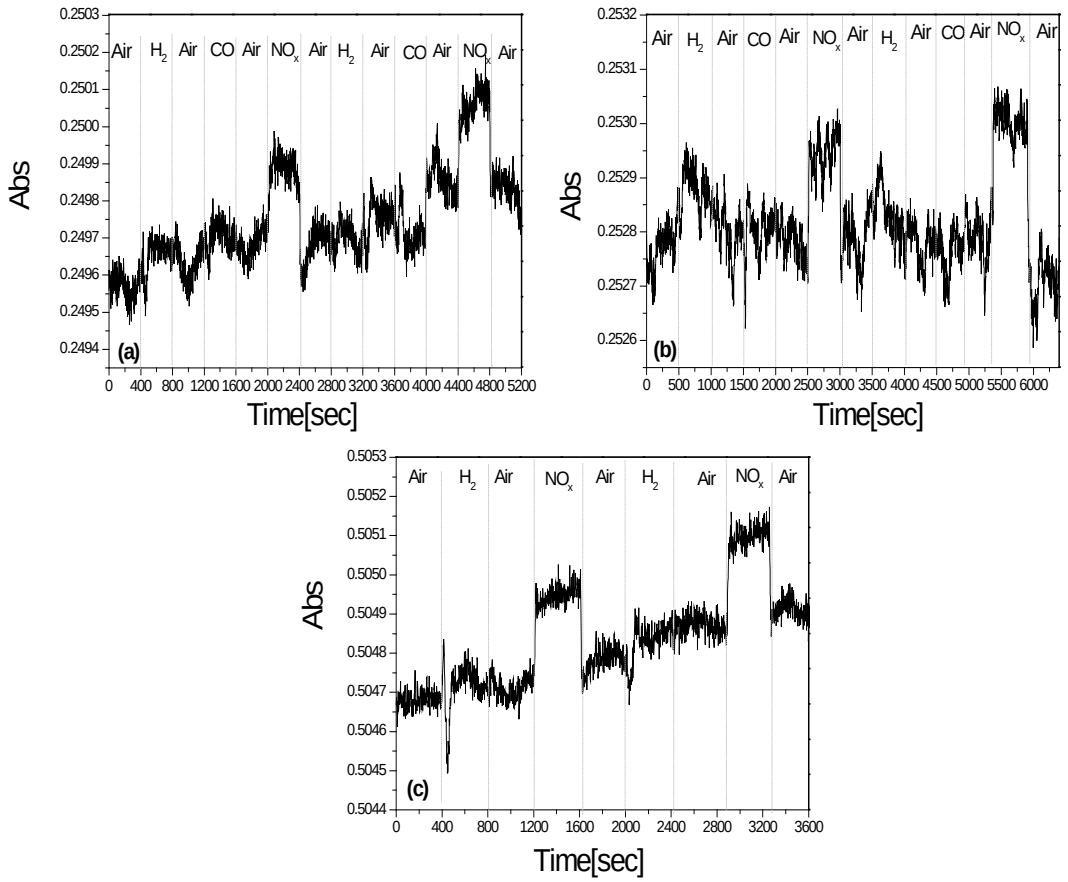

Figure 4.3 Time resolved test at 700 nm for TO unassited films at operating temperature 573 K(a) Sample annealed at 773 K, (b) Sample annealed at 873 K, (c) Sample annealed at 973 K.

The optical absorption measurements for Pt/WO_3 were tested at two different temperatures, first at room temperature and then at 423 K. The objective of this doctoral thesis was to work as closs as possible to room temperature fo rgas sensing, so for this reason we choose different temperatures. The ΔAbs at room temperature obtained for Platinum doped samples are shown in figure 4.4. In the measured

absorption spectra of the Pt-assisted WO_3 thin films under the different gases (Appendix A1, figures A 1.4 and A 1.5) absorption peaks at 760 and 850 nm were observed for H_2 The absorption change at room temperature by the effect of H_2 at 850 nm is found to be 0.006. The changes in the absorbance caused by CO are minimal as compared to H_2, and are about 2.54 $\times 10^{-4}$ at 760 nm. In a previously reported work, Ando et al [Ando 2001] did not report any response for Pt/WO_3 composite films after exposing them to H_2 at room temperature. At a working temperature of 423 K, the maximum response to H_2 recorded for our Pt doped WO_3 was close to 0.015 (at 870 nm) and 0.013 (at 350 nm). Unlike for H_2, when exposed to CO, there were not important changes in the response of Pt/WO_3 operated at 423K compared to those measured at RT.

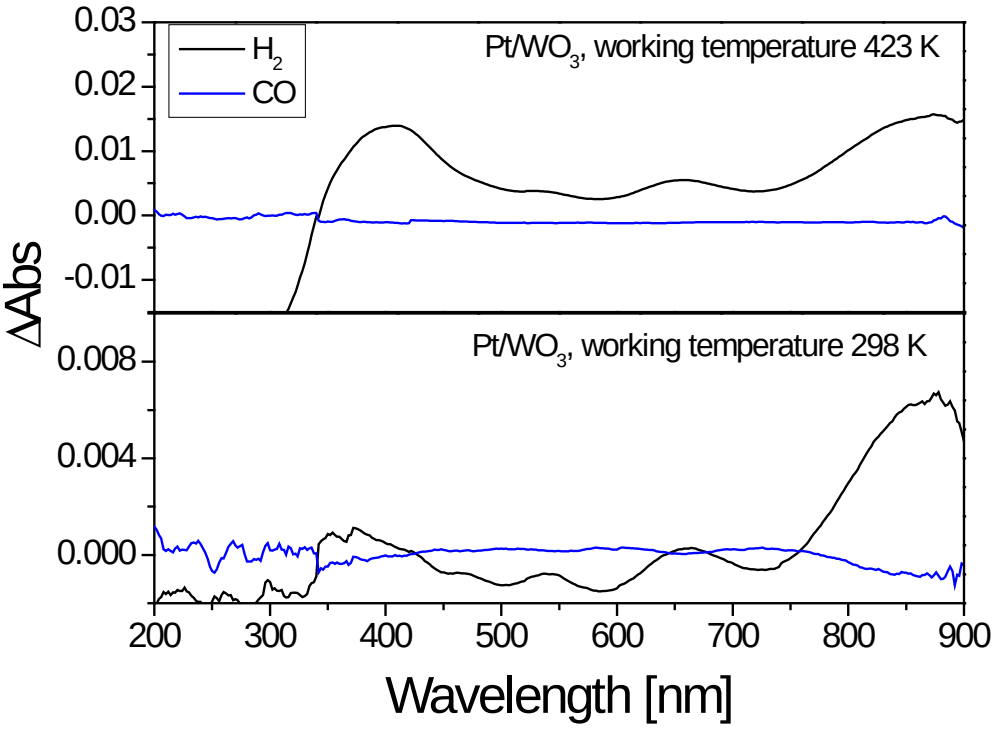

Figure 4.4 Optical Absorbance Change, $\Delta Abs = Abs_{gas} - Abs_{Air}$, curve of Pt assisted WO_3, for H_2 and CO at 423 K and room temperature.

For Pt doped samples, the absorption change observed for H_2, at 850 nm is high compared to the other gases tested. This could be foreseen since Pt is known to increase the H_2 sensitivity of metal oxides. Thus, the dynamic response of H_2 at 850 nm could be measured at RT (observed in figure 4.5 a). The response time induced by

a step change from air to H_2 is around 6 minutes. Also, as reported earlier for other noble metals, the baseline is not fully recovered due to the slow recovery from H_2 exposure at low operating temperatures [Bell 1991, Nanba 1994]. Shanak et al. [Shanak 2006] for Pt doped WO_3 films report slow recovery in the range of 50 minutes at room temperature. On the contrary, in our work, we have comparatively fast response in the range of few minutes at room temperature. Probably the size (in the range of nanometers) of our Pt nano-particles explains a high catalytic activity, even at room temperature. In that case, Pt nanoparticles either dissociate the hydrogen molecule and then hydrogen atoms spill over the metal oxide and diffuse until they reach a reaction site (active oxygen surface species) or promote the transfer of charge carriers between the gas molecule and the metal oxide via the Pt/WO_3 interface (Fermi level control) [Mizsei 1995]. Both these mechanisms eventually translate in changes in the optical properties of the material.

The dynamic responses at 650 nm for the CO gas and at 340 nm for H_2 and CO gases are plotted in figure 4.5 b and 4.5 c, respectively. The response time for CO at 650 nm is up to 300 s but at 340 nm is reduced down to 40 s. Dynamic resistance measurements of Fe activated WO_3 films for CO sensing also at 423 K, reported similar response times of about 64 s [Ahsan 2012]. The response time for H_2 is about 55 s at 340 nm. Longer response times of about 200 s have been obtained when using SnO_2 nanoparticle films as resistive gas sensors for detecting H_2 at 623 K [Kwak 2011].

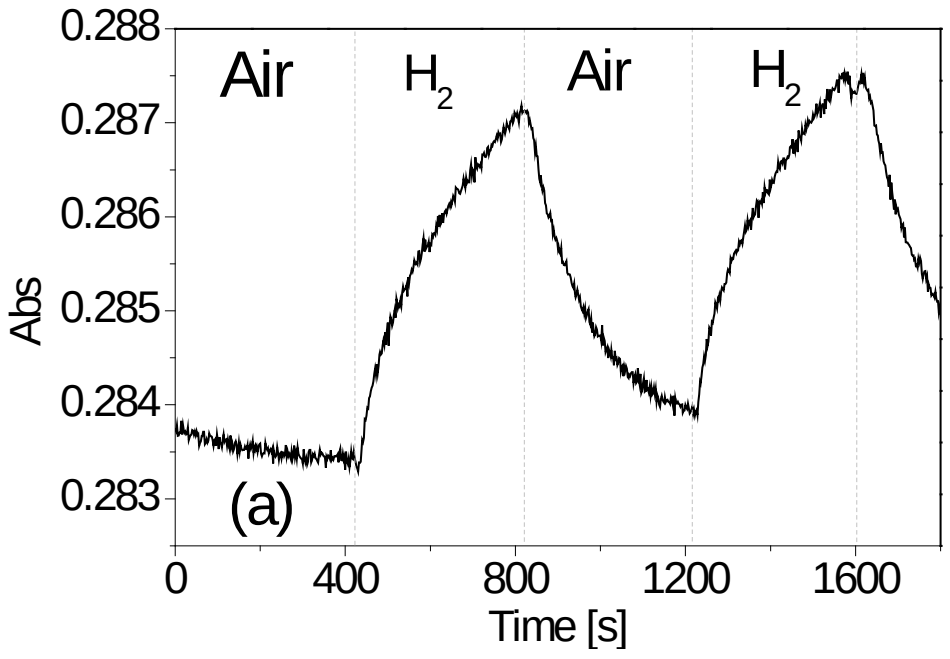

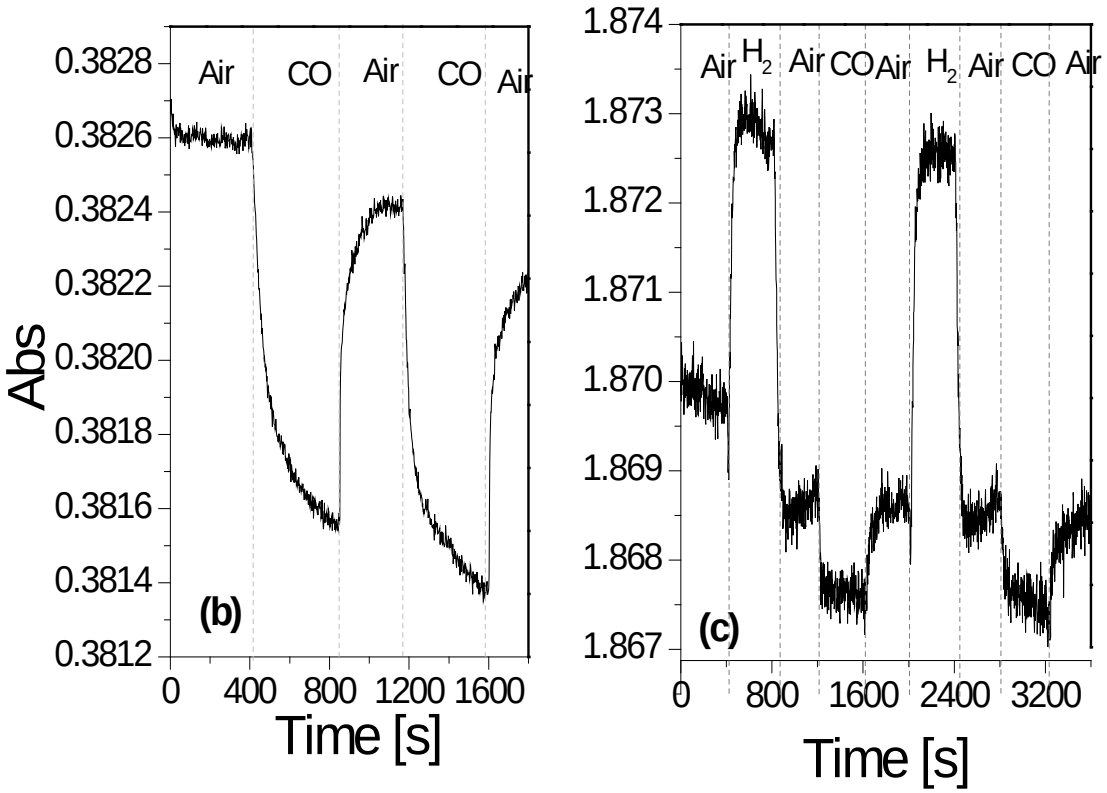

Figure 4.5 (a) Time resolved tests for the Pt assisted WO_3 at room temperature at 850 nm for H_2 gas (b) Time resolved tests for the Pt assisted WO_3 at 423 K at 650 nm for the CO gas (c) Time resolved tests for the Pt assisted WO_3 at 423 K at 340 nm for H_2 and CO gases.

The results for the gas sensing presented in the current work of WO_3 thin films doped with Pt nano-particles shows high stability, and fast recovery at room temperature and at 423 K. Ando et al. [Ando 2001] reported that their sputtered Pt/WO_3 composite films responded at a temperature of 473 K and found no response at room temperature. Shanak et al [shanak 2006] reported the colouration with undisclosed H_2 concentration at room temperature. Both of them reported issues of baseline recovery and slow recovery in the range of 50 minutes. Whereas, we have found faster response and recovery times. The response and recovery times for our samples are also found to be faster than those reported by Yaacob [Yaacob 2009]. Table 5.2 summarizes the details of the responses at the different operating temperatures and different wavelengths employed.

These results can be discussed in terms of the reaction mechanisms of H_2 and CO with the Pt-assisted WO_3 thin films. Although all the mechanisms are triggered by the chemisorption of oxygen onto the oxygen-defective WO_3 surface, [Yamazoe 1983, Shen 2009], the actual mechanisms for each gas are slightly different. In the case of CO, which is a reducing gas, it is well known that it reacts with the oxygen adsorbates

present on the WO_3 surface and generates CO_2 [Zhang 2010, Jiménez-Cadena 2007, Park2012]:

$$CO(g)+O^-(ad) \longrightarrow CO_2\,(g) + e^- \quad (1)$$

In the case of conductometric measurements, these released electrons, which are injected into the conduction band of WO_3, result in an increase of conductivity. On the other hand, for H_2 there exist two different reaction paths that induce changes in the surface of the WO_3 [Mozalev 2013, Huang 2007]. Part of the hydrogen in air reacts with the oxygen at the surface of the platinum nanoparticles and is oxidized to water:

$$2H_2(g) + O_2\,(Ad) \rightarrow 2H_2O\,(Ad) \quad (2)$$

The oxidation of H_2 molecules by O_2 molecules is an exothermic reaction that elevates the temperature, which allows the water to partly escape from the film surface [Yaacob 1998]. Another part of the molecular hydrogen dissociates on the surface of platinum, which acts as catalyst here, giving hydrogen ions and electrons:

$$H_2 \rightarrow 2H^+ + 2e^- \quad (3)$$

Atomic hydrogen readily diffuses in the WO_3 film and reduces W^{6+} centres in the WO_3 crystal lattice of the film surface to W^{5+} by the electrons generated in (3). These two gases (H_2 and CO) are reducing, and upon reaction on the WO_3 surface result in an injection of electrons that result in an increase of conductance. However, the optical measurements show two opposite trends in the change of optical absorption (an increase in the case of H_2 and a decrease for CO). This is an indication that the optical properties of the WO_3 do not only depend on the carrier concentrations and on the reducing or oxidizing nature of the detected species, but also depend of the crystal and the surface atomic structures, which are clearly different for each process.

Table 4.2 Table of the gas sensing and response time of WO_3 thin films doped with Pt on two different tmeperatures.

Sample	H_2		CO	
	Δabs	τ	Δabs	τ
WO_3-Pt 300K	0.006 (850nm)	360s (850nm)	2.54×10^{-4} (760 nm)	-
WO_3-Pt 423K	0.015 (870nm) and 0.013 (350nm)	40-45s (650nm) / 55s (340nm)	$\sim 2.54 \times 10^{-4}$ (650 nm)	300s (650nm) / 40s (340nm)

4.3 Optical absorption spectroscopy of WO_3 nanoneedles under the influence of NH_3 gas

The gasochromic behaviour of our grown nanoneedles were performed simmilarly as done for WO_3 thin films i.e. by measuring optical absorption spectra under the influence of NH_3 (100ppm) gas. All the tests were performed at room temperature, a reversible change has been recorded for the sample 7 and 9 from the table 3.4. All the spectra have been recorded in presence of gas at room temperature. The absorbance spectra are reported in figures A1.6 and A1.7 of Appendix A1. In contrast to previous works [Vallejos 2010, Vallejos 2013, Annanouch 2013] we see a detectable change. This is the first time ever in which an optical gas response of tungsten oxide nanoneedles operated at room temperature is reported. All the tests were repeated several times with and without gas in order to check the reproducibility. We did not see any change of the absorption by the effect of the NH_3 gas in samples without Au and Pt, at RT. For these optical gas sensing measurements for the nanoneedles we have used the home made gas cell, which hasn't the possibility to work at high temperatures, so we coudn't check the response at higher temperatures. Thus, as in the thin film samples, there's a change of absorption under the effect of gas for the samples with Au and Pt NPs, demonstrating that the Au and Pt NPs play an active role in the reaction process at the surface of the sensing layer.

The absorption of the Au assisted films suggests the presence of the surface plasmons at the wavelength 560 nm. The change induced due to the NH_3 gas in the absorbance is the change of absorbance of small Au particles. The observed absorbance change in the presence of NH_3 is probably related to a change in the plasmon resonant wavelength of the Au nano particles. This plasmon resonant frequency depends on both the optical properties of the Au and of the WO_3 nanoneedles. The optical properties of the Au change by the electron transfer between the adsorbed NH_3 and the metal, while the optical properties of the WO_3 change because of the formation of tungsten bronze in the presence of the NH_3 gas [Ando 2001]. The maximum change in the absorbance under the influence of gas was 0.0002 (shown in the figure 4.6). The initial air to NH_3 transient was fast and in the range of 4 s. The slow baseline recovery dynamics due is to the slow process of desorption of the reaction products formed at the active sites.

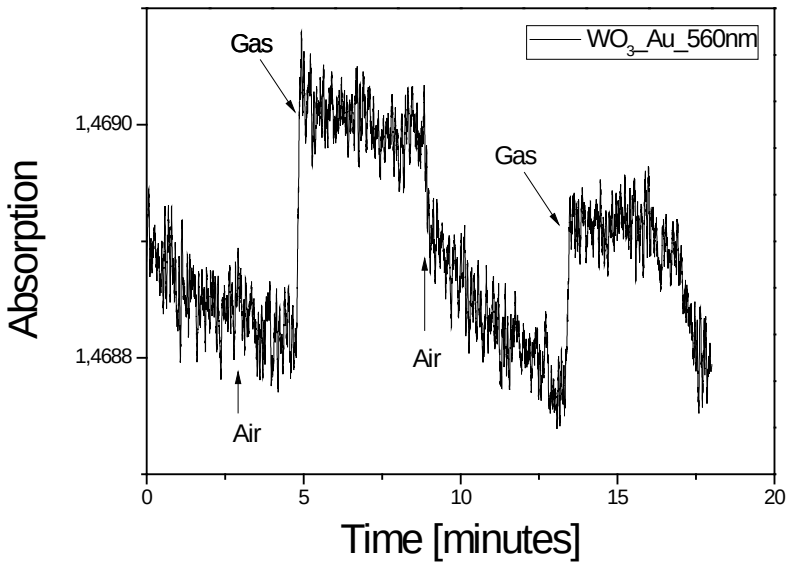

Figure 4.6 Dynamic response of the Au assisted WO_3 nanoneedles at 560 nm wavelength under the influence of NH_3 gas.

In the case of Pt-WO_3 nanoneedles we identified two wavelengths where the change of absorbance was 485 nm and 355 nm. The dynamic response of the Pt-WO_3 nanoneedles is shown in the figure 4.7 at 485 nm and at 355 in figure 4.8. The change of absorption due to the effect of gas is attributed to catalytic change in the case of Pt-WO_3 [Yaacob 2009, Ando 2001]. The maximum change in the absorption under the

influence of NH_3 recorded for Pt-WO_3 at 485 nm was 0.0013 and at wavelength 355 nm was 0.0023. The initial air to NH_3 transient was in the range of 8 s at 485 nm and 12 s for 355 nm. Also the change induced by Pt assisted WO_3 nanoneedles is better then Au assisted ones. The reason for better change with Pt assisted films is better catalytic activity of Pt towards reducing gases.

The sensing mechanism of NH_3 by the Pt-WO_3 nanoneedles, according to Bittencourt et al. [Bittencourt 2002] is also mediated by the adsorbed oxygen on the WO_3 surfaces:

$$3/2\ O_2\ (g) + 3/2e^- \text{—>}\ 3/2\ O_2^-\ (Ad)\ (4)$$

The NH_3 is detected in a two-step process. In the first step NH_3 is adsorbed onto the surface in the same way as O_2:

$$2\ NH_3\ (g) \text{—>}\ 2NH_3^{3/4+}(Ad)+3/2e^-\ (5),$$

then the surface adsorbed species undergo an oxidation-reduction process that produces N_2 and H_2O via the formation of a complex onto the WO_3 surface:

$$2NH_3(g) + 3/2\ O_2\ (g) = [(2NH_3(^{3/4+})(3/2\ O_2^-)]\ (Ad) = N_2\ (g) + 3H_2O\ (g)\ (6).$$

According to Gerblinger et al. [Gerblinger 1994], the creation of this surface complex, whether it is charged or not, changes the bonding relationships on the surface of the metal oxide, i.e., the coordination of the metal by oxygen ions or the bond lengths between the ions. This changes the electronegativity (bandgap) of the metal oxide. The narrowing of the bandgap creates an accumulation region, and increases both the space-charge region in n-type semiconductors such as WO3 , and conductivity. The

effects of changing the bandgap are reflected in the changes of absorbance of the material.

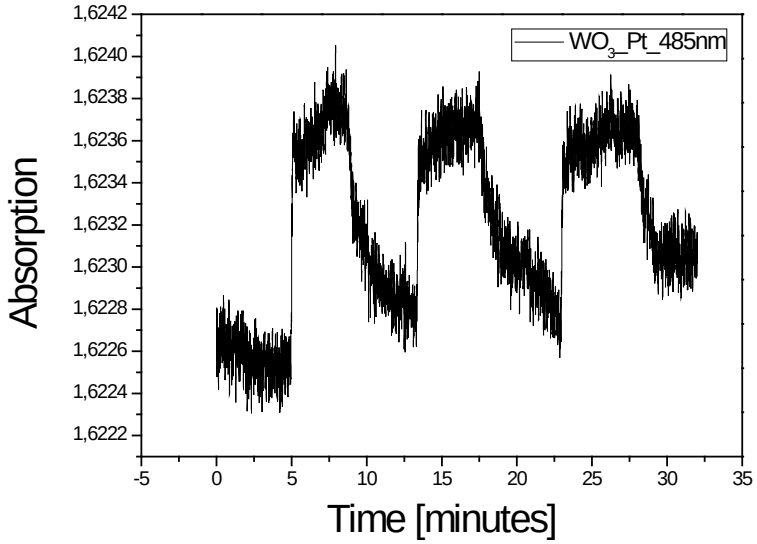

Figure 4.7 Dynamic response of the Ptassisted WO_3 nanoneedles at 485 nm wavelength under the influence of NH_3 gas.

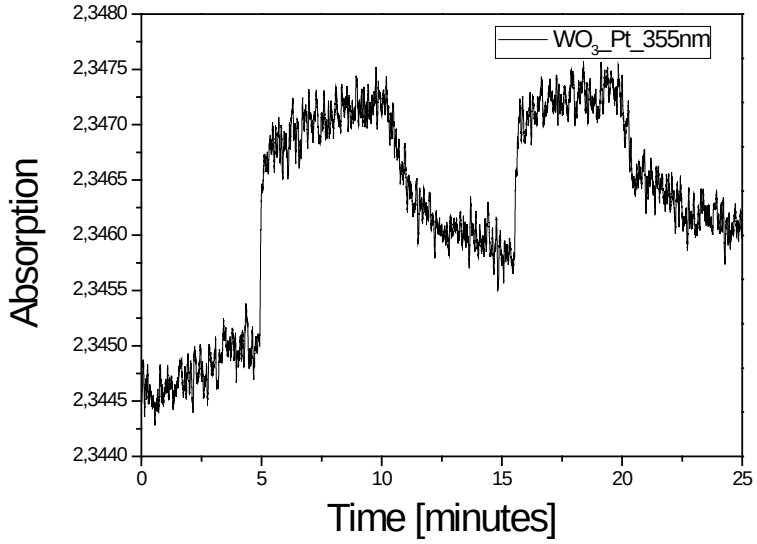

Figure 4.8 Dynamic response of the Ptassisted WO_3 nanoneedles at 355 nm wavelength under the influence of NH_3 gas.

4.4 Photoluminescence of WO_3 nano-crystals

The third method used in this doctoral thesis to grow WO_3 nanocrystals was the modified pechini sol-gel, described in detail in chapter 3. We discuss here its optical properties using photoluminescence. In figure 4.9 it is shown the photoluminescence of the WO_3 nanoparticles excited at 290 nm at room temperature. It can be observed a broad band located in the visible region, with a maximum around 450 nm.

It is believed that the particle size, morphology and quantum confinement effect play a role for the room temperature emission [Khold 2004]. The emission properties of WO_3 since it is an indirect-gap semiconductor will have low emission efficiency.

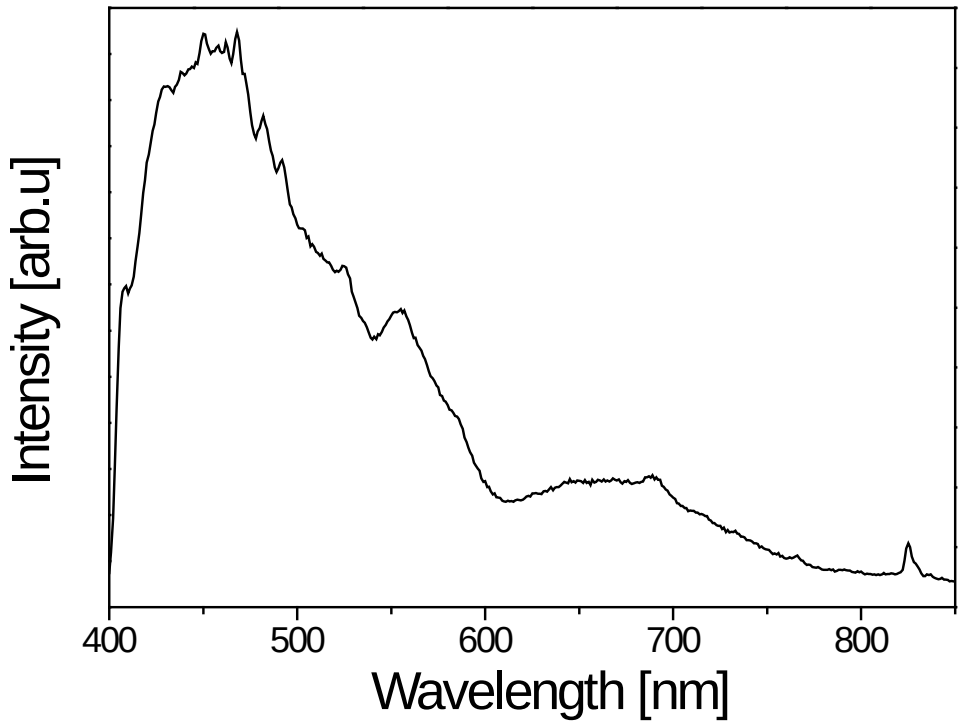

Figure 4.9 Photoluminiscence of the WO_3 nanocrystals grown by modified Pechini method.

In literature, it has been reported that WO_3 can show photoluminescence at low temperatures, around 4.2 K, getting weaker below 100 K. Already at 65 K, the

luminescent intensity decreases to 50%. It has an excitation maximum at 410 nm, and emission maximum at 700 nm (4.2K). This luminescence has been assigned to a charge transfer mechanism, originated by a self trapped exciton on the d^0-ion octahedron. The phenomena of the quenching at higher temperatures can be explained by the mobility of the exciton at these temperatures migrating to quenching centers [Blasse 1995]. WO_3 crystalline nanosheets exhibit blue emission at 431,486 and 497 nm, resulting from the band-band indirect transition (semiconductor band gap). Also, they show UV emission at 362 nm and 398 nm, attributed to defect states of WO_3 (excitation at 315 nm); the excitation in both cases was with Xe Lamp at room temperature [Wang 2009].

Chang et al. have reported in [Chang 2003], a broad emission centred at 470 nm excited by UV in WO_3 nanorods at room temperature. The authors exclude the quantum confinement as origin phenomena because the diameter of the WO_3 nanowires is larger than the critical radius. The emission is attributed to a trap state emission; the trap is assigned to an oxygen vacancy. Similar results attributed to oxygen related defects were reported for ZnO and Al_2O_3 nanowires [Peng 2002, Dai 2002]. In a similar way, Feng et al. [Feng 2005] reported that the two peaks observed in the photoluminescence of WO_3 films, were attributed the shorter wavelength one to the quantum confinement and the peak at longer wavelength, around the blue, to oxygen vacancies.

In our case, the photoluminescence must be also related to a trap defect; or surface defect, because the quantum confinement is also excluded due to the size of the nanoparticles.

Summary

In this chapter, we have explained in details the gasochromic sensing performance of the developed WO_3 nanostructures and thin films towards CO, NO_x, H_2 and NH_3. The investigation of the gasochromic sensing performances were carried out on the optical absorbance measurements. The WO_3 thin films and nanoneedles exhibit optical change when exposed to the gases mentioned above, also the doping of WO_3 nanostructures with different noble metals happened to increase the sensitivity of the material. In this doctoral thesis, the author have successfully shown the gasochromic behaviour of WO_3 assisted nanoneedles at room temperature towards NH_3.

CHAPTER 5

CONCLUSIONS

5 Conclusions

The investigation of the semiconductor metal oxides with gasochromic properties was amongst the main tasks of the present thesis. For that, WO_3 was chosen as a sensing material for the optical gas sensing due to its excellent optical and electrical properties reported already in the in the literature, and, discussed more specifically along this doctoral thesis.

The Department of Electrical and Electronics Engineering of the Universitat Rovira I Virgili (URV) has been focusing on the development of semiconductor gas sensors during the last years.This includes the development of new semiconductor materials, their characterization, as well as the testing behavior of the gas sensor devices. Their experience in WO_3 for more than one decade also suggests that this is good future candidate for gasochromic applications.

Three different WO3 morphologies have been studied in this doctoral thesis. They are as follows:

WO_3 thin films obtained by RF magnetron sputtering Using RF magnetron sputtering nanotextured thin films of thickness around 550 nm were grown on quartz (fused silica) substrate; the films were transparent enough for optical absorption spectroscopy. Their optical properties as well as gasochromic behavior has been evaluated as they were subjected to gas sensing tests under the effect of H_2, CO and NO_x. Their micro-nano characterization reveals that the surface of the thin films is composed of nano-sized voids and grains; also the roughness of these films subjected to an annealing after their growth increases hence the grain size increases, and this enhances the sensing behavior of the material.

These films show a reversible change of the optical absorption in the presence of gas and the transient time (air to gas and gas to air) is in the range of seconds, which is excellent as compared to the times reported in previous works. Further, these films were doped with Pt nanoparticles in order to enhance the sensitivity and transient time. These Pt/WO_3 films show much faster response and recovery time than the undoped samples. Also, they response at room temperature, which is the first time reported for Pt/WO_3 thin films using optical absorption spectroscopy. The Pt/WO_3 films were found highly sensitive to H_2 gas..

The results obtained for the gasochromic behaviour of the WO3 thin films suggest the possibility for developing a device for detecting multiple gases employing nanotextured WO_3 thin films.

WO_3 nanoneedles grown by AACVD WO_3 nano-needles have been grown on quartz substrate by Aerosol Assisted chemical vapor deposition (AACVD). The conditions of the growth have been adjusted in order to have a transparency enough for the absorption measurements. The grown nanoneedles have highly oriented crystalline structure. The length of the needles is in the range of few microns and the diameter in the range of nanometers. These nanoneedles were doped with Au and Pt nanoparticles in a single step of growth. The gaschromic response of these films was investigated upon the exposure to NH_3. We demonstrate for the first time the optical gas sensing results obtained using these functionalised nanoneedles at room temperature under the influence of NH_3 gas. They show fast response and recovery time as low as 4 seconds. Gas sensors employing AA-CVD grown tungsten oxide nanoneedles show enhanced performance in comparison to standard polycrystalline tungsten oxide films. This is possibly due to the former having higher surface-to-volume ratio and better stability (e.g. they are single crystalline) than the latter. However, more studies are needed to better control both the size of metal particles decorating the surface of nanoneedles and the surface coverage.

WO_3 nanocrystals obtained by sol-gel Pechini method Monoclinic WO_3 nanocrystalline powder was obtained by a simple route of modified Pechini method. DTA and X-ray measurements were used to refine the appropriate calcination temperature. The particle size and its dispersion have been analyzed by electron microscopy, obtaining an average size of the crystallite near 20 nm. Their optical properties were evaluated using PL measurements,but still the gasochromic behavior of these nanocrystals has not been evaluated.

In summary, this PhD thesis successfully fulfilled its objectives to investigate novel WO_3 optical sensors based on nanostructures and thin films. During the work, the author had successfully implanted this material for optical sensing of NH_3, CO, NO_x, and H_2 gases. The evaluation based on these results make WO_3 a good candidate for future optical gas sensing devices.

.

References

[Akedo 1999] J. Akedo and M. Lebedev, “Microstructure and electrical properties of lead zirconate titanate ($Pb(Zr_{52}/Ti_{48})O_3$) thick films deposited by aerosol deposition method”, Japanese Journal of Applied Physics, Part 1: Regular Papers and Short Notes and Review Papers, vol. 38, pp. 5397-5401, 1999.

[Ashraf 2008] S. Ashraf, C.S. Blackman, R. Binions and I.P. Parkin, “The APCVD of tungsten oxide thin films from reaction of WCl_6 with ethanol and results on their gas-sensing properties”, Polyhedron, vol 26, pp. 1493-1498, 2008.

[Bendahen 2004] M. Bendahan, R. Boulmani, J. L. Seguin, and K. Aguir, "Characterization of ozone sensors based on WO_3 reactively sputtered films: influence of O_2 concetration in the sputtering gas and working temperature," Sens. Actuators B, vol. 100, pp. 320-324, 2004.

[Bittencourt 2002] C. Bittencourt, R. Landers, E. Llobet, G. Molas, X. Correig, M. A. P. Silva, J. E. Sueiras and J. Calderere “Effects of Oxygen Partial Pressure and Annealing Temperature on the Formation of Sputtered Tungsten Oxide Films”, Electrochemical Society, Vol. 149, Issue 3, pp. H81-H86, 2002.

[Blackman 2005] C. S. Blackman and I. P. Parkin, “Atmospheric pressure chemical vapor deposition of crystalline monoclinic WO_3 and WO_{3-x} thin films from reaction of WCl_6 with O-containing solvents and their photochromic and electrochromic propertie, Chemical Material, vol 17, pp. 1583-1590, 2005.

[Bnage 1999] K. Bange, “Colouration of tungsten oxide films: A model for optically active coatings”, Sol. Ener. Mater. and Sol. Cell, vol 58, pp. 1-131, 1999.

[Brattain 1952] J.B.W.H. Brattain, The Bell System Technical Journal, 32, 1, 1952.

[Brinker 1990] C. J. Brinker and G.W. Scherrer, Sol-Gel Science. The physics and chemistry of Sol-Gel processing; Academic Press, San Diego: 1990.

[Cao 2004] G. Cao, Nanostructures and Nanomaterials: Synthesis, Properties and Applications. London: Imperial College Press, 2004.

[Cazzanelli 1999] E. Cazzanelli, Mariotto, C. Vinegoni, A. Kuzmin and J. Purans, Low temperature polymorphism in tungsten trioxide powders and its dependence on mechanical treatments, J. Solid state chemistry, vol 143, pp. 24,1999.

[Cerqueira 1995] M. Cerqueira, R. S. Nasar, E. Longo, E. R. Leite and J. A. Varela, “Synthesis of ultra-fine crystalline $Zr_xTi_{1-x}O_4$ powder by polymeric precursor method,” Materials Letters, vol 22, pp. 181-185, 1995.

[Chattopadhyay 2010] S. Chattopadhyay, Y. F. Huang, Y. J. Jen, A. Ganguly, K. H. Chen, and L. C. Chen, "Anti- Reflecting and Photonic Nanostructures," Materials Science and Engineering: R: Reports, vol. 69, pp. 1-35, 2010.

[Chen 2008]. D. Chen, L. Gao, A. Yasumori, K. Kuroda and Y. Sugahara, “Size- and Shape-Controlled Conversion of Tungstate-Based Inorganic–Organic Hybrid Belts to WO_3 Nanoplates with High specific surface areas”, small, vol 4, No. 10, pp. 1813–1822, 2008

[Choy 2003] K. L. Choy, “Chemical vapour deposition of coatings”, Progress in Materials Science, vol. 48, pp. 57-170, 2003.

[Cross 2003] W. B. Cross, I. P. Parkin and S. A. O’Neill, ”Tungsten Oxide Coatings from the Aerosol-Assisted Chemical Vapor Deposition of $W(OAr)_6$ (Ar) C_6H_5, C_6H_4F-4, $C_6H_3F_2$-3,4); Photocatalytically Active γ-WO_3 Films”, Chemistry of materials, vol 15, pp. 2786-2796, 2003.

[Cullity 1978] B. D. Cullity, “Element of X-Ray diffraction”, Addison-Wesley, 1978.

[Daniel 1987] B. D. Daniel, J. C. Lassegues, B. Gerand and M. Figlarz, “Infrared Raman Study of WO_3 Tungsten Trioxide and WO_3,xH_2O Tungsten Trioxide Hydrates”, J. Solid State Chem, vol 67, pp. 235-247, 1987.

[Deb 1992] S. K. Deb, Opportunities and Challenges of Electrochromic Phenomena in Transition- Metal Oxides, Solar Energy Materials and Solar Cells, vol. 25, pp. 327-338, 1992.

[Deb 2008] S. K. Deb, "Opportunities and Challenges in Science and Technology of WO_3 for Electrochromic and Related Applications," Solar Energy Materials and Solar Cells, vol. 92, pp. 245-258, 2008.

[Depero 1996] L. E. Depero, S. Groppelli, I. Natali-Sora, L. Sangaletti, G. Sberveglieri and E. Tondello, “Structural Studies of Tungsten–Titanium Oxide Thin Films” J. Solid State Chem.,vol 121, pp.379 387, 1996.

[Depero 1996] L.E. Depero, S. Groppelli, I. Natali-Sora, L. Sangaletti, G. Sberveglieri and E.Tondello, ”Structural studies of tungsten-titanium oxide thin tilms”, Solid state chemistry, vol 121, pp. 379-387, 1996.

[Faughnan 1975] B. W. Faughnan, R. S. Crandall, and P. M. Heyman, "Electrochromism in WO_3 Amorphous Films," RCA Review, vol. 36, pp. 179-197, 1975.

[Fernandes 2002] J. D.G. Fernandes, D. M. A. Melo, L. B. Zinner, C. M. Salustiano, Z. R. Silva, A.E. Martinelli, M. Cerqueira, J. C. Alves, E. Longo and M.I.Benardi, “Low-temperature synthesis of single-phase crystalline $LaNiO_3$ perovskite via Pechini method,” Materials Letters, vol 53, pp. 122-125, 2002.

[Ferraro 2003] J. R. Ferraro, K. Nakamoto and C. W. Brown, “Introductory Raman spectroscopy”, second edition Academic press, 2003.

[Fieller 1992] N. R. J. Fieller, E. C. Flenley and W. Olbricht, “Statictics of particle size data” J. Appl. Stat. vol 41, pp. 127-146, 1992.

[Galceran 2011] M. Galceran, Synthesis and characterization of optical nanocrystals and nanostructures an approach to transparent laser nanoceramics, Doctoral Thesis, UniversitatRovira I virgili, ISBN:978-84-693-1534-7, 2011.

[Gopel 1990] W. Gopel, J. Hesse, and J. N. Zemel, Sensors: A Comprehensive Survey: VCH, 1990.

[Gorokh 2006] G. Gorokh, A. Mozalev, D. Solovei, V. Khatko, E. Llobet and X. Correig, ”Anodic formation of low-aspect-ratio porous alumina films for metal-oxide sensor application”, Electrochimica Acta, vol 52, pp. 1771–1780, 2006.

[Gorokh 2006] G.Gorokh , A. Mozalev , D. Solovei , V. Khatko , E. Llobet and X. Correig “Anodic formation of low aspect-ratio porous alumina films for metal-oxide sensor application” Electrochimica Acta, vol.52, pp.1771–1780, 2006.

[Granqvist 1976] C.G. Granqvist and R.A. Buhrman, “Ultrafine metal particles” J. Appl. Phys, *vol* 47, pp. 2200, 1976.

[Granqvist 2000] C.G. Granqvist, “Electrochromic tungsten oxide, Review of progress” 1993-1998, Solar Energy Materials & Solar Cells, vol 60, pp. 201-262, 2000.

[Granqvist 2003] C. G. Granqvist, "Solar Energy Materials," Advanced Materials, vol. 15, pp. 1789-1803, 2003.

[Hamagami 1993] J.-i. Hamagami, Y.-s. Oh, Y. Watanabe, and M. Takata, "Preparation and Characterization of an Optically Detectable H_2 Gas Sensor consisting of Pd/MoO_3 Thin Films," Sensors and Actuators B: Chemical, vol. 13, pp. 281-283, 1993.

[Hellegouarc'h 2001] F. Hellegouarc'h, F. Arefi-Konsari, R. Planade, and J. Amouroux, “PECVD prepared SnO_2 thin films for ethanol sensors,” Sensors and Actuators B, vol. 73, pp. 27-34, 2001.

[Herricks 2004] T. Herricks, J.Chen and Y. Xia, ”Polyol synthesis of platinum nanoparticles: control of morphology with sodium nitrate”, Nano Lett.,vol 4,pp. 2367, 2004.

[Hjelm 1996] A. Hjelm, C. G. Granqvist, and J. M. Wills, “Electronic Structure and Optical Properties of WO_3, $LiWO_3$, $NaWO_3$, and HWO_3,” Physical Review B - Condensed Matter and Materials Physics, vol. 54, pp. 2436-2445, 1996.

[Hubert-Pfalzgraf 1998] L. G. Hubert-Pfalzgraf and H. Guillon, "Trends in precursor design for conventional and aerosol-assisted CVD of high-Tc superconductors," Applied Organometallic Chemistry, vol. 12, pp. 221-236, 1998.

[Interrante 1998] L. V. Interrante, Z. Jiang and D. J. Larkin, ”Preparation of the high-temperature superconductor $YBa_2Cu_3O_{7-x}$”, ACS Symposium Series, vol 77, pp. 168-180, 1998.

[Ito 1992] K. Ito and T. Ohgami, "Hydrogen Detection based on Coloration of Anodic Tungsten-Oxide Film," Applied Physics Letters, vol. 60, pp. 938-940, Feb 24 1992.

[Ivanov 2004] PhD thesis by P. T. Ivanov, “Design, fabrication and characterization of thick film gas sensors,” 2004.

[Joraid 2007] A. A. Joraid and S.N. Alamri, “Effect of annealing on structural and optical properties of WO_3 thin films prepared by electron-beam coating”, Physica B, vol 391, pp.199–205, 2007.

[Joshi 2011]. U. A. Joshi, J. R. Darwent, H. P. Yiu and M. J. Rosseinsky “The effect of platinum on the performanceof WO_3 nanocrystal photocatalystsfor the oxidation of Methyl Orange and iso-propanol” J Chem Technol Biotechnol, vol 86, pp. 1018–1023, 2011.

[Kakihama 1996] M. Kakihama, “Invited review sol-gel preparation of high temperature superconducting oxides”, Journal of Sol-Gel Science and Technology, vol 6, pp. 7-55,1996.

[Kim 2000] T. S. Kim, Y. B. Kim, K. S. Yoo, G. S. Sung, and H. J. Jung, "Sensing characteristics of dc reactive sputtered WO_3 thin films as an NO_x gas sensor," Sens. Actuators B, vol. 62, pp. 102- 108, 2000.

[Korotcenkov 2007] G. Korotcenkov,Metal oxides for solid-state gas sensors: What determines our choice Materials Science and Engineering: B Volume 139, Pages 1–23, 2007.

[Kuzmin 1998] A. Kuzmin, J. Purans, E. Cazzanelli, C. Vinegoni, and G. Marioto, "X-ray diffraction, extended x-ray absorption fine structure and raman spectroscopy studies of WO_3 powders and (1-x)WO_{3-y} .xReO_2 mixtures," J. Appl. Phys., vol. 84, pp. 5515-5523, 1998.

[Kwon 1998] S. W. Kwon, S.B. Park, G. Seo and S.T. Hwang, “Preparation of lithium aluminate via polymeric precursor routes,” Journal of Nuclear Materials, vol 257,pp. 172-179, 1998.

[Lassner 1999] E. Lassner and W.D. Schubert, Tungsten: properties, chemistry, technology of the element, alloys, and chemical compounds: Plenum Publishers, New York, 1999.

[Lee 2000] D. S. Lee, K. H. Nam, and D. D. Lee, "Effect of substrate on NO_2 -sensing properties of WO_3 thin film gas sensors," Thin Solid Films, vol. 375, pp. 142-146, 2000.

[Lessing 1989] P. A. Lessing, “Mixed-cation oxide powders via polymeric precursors”, American Ceramic Society Bulletin,vol 68, pp. 1002-1007, 1989.

[Macleod 2001] H. A. Macleod, “Thin-film optical filters”, Institute of physics publishing, ISBN: 0750306882, 2001.

[Mattox 2010] D. M. Mattox “Handbook of Physical Vapor Deposition (PVD) Processing (Second Edition)”, Elsevier Applied science Publishers, ISBN: 978-0-8155-2037-5, 2010.

[Moseley 1987] P. T. Moseley and C. Tofield,, "Conduction and gas response of semiconductor gas sensors," in Solid state gas sensors, Eds. Bristol: Adam Hilger, pp. 71-123, 1987.

[Nishide 1995] T. Nishide and F. Mizukami, “Crystal structures and optical properties of tungsten prepared by a complexing-agent-assisted sol- gel processes”, Thin Solid Films,vol 259, pp. 212-217, 1995.

[Patel 2009] K. J. Patel et al. “Growth, structural, electrical and optical properties of the thermally evaporated tungsten trioxide (WO_3) thin films, ” Materials Chemistry and Physics, vol 114, pp.475–478, 2009.

[Patterson 1939] A.L Patterson, The scherrer formula for X-ray particle size determination” Physical review, vol 56, pp. 477-482, 1939.

[Pechini 1967] M.P.Pechini, “Method of preparing lead and alkaline earth titanates and niobates and coating method using the same to form capacitor”, 1967.

[Pelgrave 2006] R. G. Palgrave and I. P. Parkin, “Aerosol Assisted Chemical Vapor Deposition Using Nanoparticle Precursors: A Route to Nanocomposite Thin Films” J. AM. CHEM. SOC, vol 128, pp. 1587-1597, 2006.

[Pierson 1999] H. O. Pierson, “Handbook of chemical vapor depostion (CVD) principles, technology, and applications”, Noyes Publications/William Andrew Pub., 1999, ISBN: 978-0-8155-1432-9.

[Quinelato 2000] A. L. Quinelato, E. Longo, L. A. Perazolli and J. A. Varela, “Effect of ceria content on the sintering of ZrO_2 based ceramics synthesized from a polymeric precursor,” Journal of the European Ceramic Society, vol 20, pp. 1077-1084, 2000.

[Rodriguez-Carvajal 1998] J. Rodriguez-Carvajal,Short reference guide for the computer program FULLPROF Laboratorie Leon Brilluin, CEA-CNRS, Gif sur Yvette, 1998.

[Rouquerol 2004] J. Rouquerol and K. Sing, “Adsorption by Powders and Porous Solids”, Academic Press, London, 1999.

[Roy 1955] D.M. Roy and R. Roy, Synthesis and stability of minerals in the system MgO-Al_2O_3-SiO_2-H_2O, American Mineralogist,vol 40, pp. 147, 1955.

[Salje 1975] E. Salje and K. Viswanathan, “Physical properties and phase transitions in WO_3”, Acta Cryst. A, vol 31, pp. 356-361,1975.

[Seiyama 1962] T. Seiyama, A. Kato, K. Fujushi and M. Nagatani, Analytical Chemistry, 34, 1502f, 1962.

[Shaver 1967] P. J. Shaver, "Activated tungsten oxide gas detectors," Applied Physics Letters, vol. 11, pp. 255, 1967.

[Shigesato 1991] Y. Shigesato, Y. Hayashi, A. Masui and T. Haranou, “The structural changes of indium-tin and α-WO_3 films by introducing water deposition process,” Jpn. J. Appl. Phys. vol 30, pp. 814-819, 1991.

[Shimizu 1999] Y. Shimizu and M. Egashira, "Basic aspects and challenges of semiconductor gas sensors" MRS Bulletin, vol. 24, no. 6, pp. 18-24, 1999.

[Sing 2004] Sing, S.W. Kenneth, Williams and T. Ruth, Physisorption hysteresis loops and the characterization of nanoporous materials Adsorption Science and Technology, vol 22(10), pp. 773–782, 2004.

[Söderlund 1998] J. Söderlund, L. B. Kiss, G. A. Niklasson and C. G. Granqvist, “Lognormal Size Distributions in Particle Growth Processes without Coagulation”, Phys. Rev. Lett. vol 80, pp. 2386, 1998.

[Souza-Filho 2000] A. G. Souza-Filho, V. N. Freire, J. M. Sasaki, J. Mendes Filho, J. F. Julĩao and U. U. Gomes, “Coexistence of triclinic and monoclinic phases in WO_3 ceramics”, J. of raman spectroscopy,J. Raman Spectrosc, vol 31, pp. 451–454, 2000.

[Stoycheva 2011] T. Stoycheva, “Fabrication and gas sensing properties of pure and Au-functionalised WO_3 nanoneedle-like structures, synthesised via Aerosol Assisted Chemical Vapour Deposition method”, doctoral thesis UniversitatRovira I virgili, Dipòsit Legal: T-1803-2011.

[Sumida 2005] S. Sumida, S. Okazaki, S. Asakura, H. Nakagawa, H. Murayama, and T. Hasegawa, "Distributed Hydrogen Determination with Fiber Optic Sensor," Sensors and Actuators B: Chemical, vol. 108, pp. 508-514, 2005.

[Tabib-Azar 1995] M. Tabib-Azar, Integrated Optics, Microstructures, and Sensors. Massachusettes: Kluwer Academic Publishers, 1995.

[Tagtstrom 1999] P. Tagtstrom and U. Jansson, “Chemical vapour deposition of epitaxial WO_3 films” Thin Solid Films, vol 352, pp. 107, 1999.

[Taguchi 1972] N. Taguchi, Gas detecting element and methods of making it, 1972, US Patent 3644795.

[Vallejos 2007] S. Vallejos, V. Khatko, K. Aguir, K.A. Nago, J. Caladerer, I. Garcia, C. Cane, E. Llobet and X. Correig, “Ozone monitoring by micro-machined sensors with WO_3 sensing films” Sensors and Actuators B, vol. 126, pp. 573–578, 2007.

[Vallejos 2011] Stella Vallejos, Toni Stoycheva, Polona Umek, Cristina Navio, Rony Snyders, Carla Bittencourt, Eduard Llobet, Christopher Blackman, Savio Moniz and Xavier Correig “Au nanoparticle-functionalised WO_3 nanoneedles and their application in high sensitivity gas sensor devices”, Chemical Communications The Royal Society of Chemistry, vol 47, pp. 565-567, 2011.

[Vallejos 2013] S. Vallejos , P. Umek , T. Stoycheva , F. Annanouch , E. Llobet , X. Correig , P. D. Marco , C. Bittencourt and C. Blackman, “Single-Step Deposition of Au- and Pt-Nanoparticle-Functionalized Tungsten Oxide Nanoneedles Synthesized Via Aerosol-Assisted CVD, and Used for Fabrication of Selective Gas Microsensor Arrays”, Advanced Functional Materials, vol 23, pp. 1313–1322, 2013.

[Washizu 2003] E. Washizu, A. Yamamoto, Y. Abe, M. Kawamura and K. Sasaki, ”Optical and electrochromic properties of RF reactively sputtered WO_3 films”, Solid State Ionics, vol 165, pp.175– 180, 2003.

[Washizu 2003] E. Washizu, A. Yamamoto, Y. Abe, M. Kawamura and K. Sasaki, “Optical and electrochromic properties of RF reactively sputtered WO_3 films”, Solid State Ionics, vol 165, pp. 175– 180, 2003.

[Weckhuysen 2000] B. M. Weckhuysen, J.-M. Jehng and I. E. Wachs, “In Situ Raman Spectroscopy of Supported Transition Metal Oxide Catalysts: $^{18}O_2$-$^{16}O_2$ Isotopic Labeling Studies” J. Phys. Chem. B, vol 104, pp. 7382-7387, 2000.

[Wright 1877] A. W. Wright, The use of electrical deposition apparatus to form mirrors and study their properties, American journal of science and arts, 1877.

[Yaacob 2009] M. H. Yaacob, M. Breedon, K. Kalantar-zadeh, and W. Wlodarski, "Absorption Spectral Response of Nanotextured WO_3 Thin Films with Pt Catalyst Towards H_2," Sensors and Actuators B: Chemical, vol. 137, pp. 115-120, 2009.

[Yamazoe 2005] N. Yamazoe, Toward Innovations of Gas Sensor Technology," Sensors and Actuators, B: Chemical, vol. 108, pp. 2-14, 2005.

[Young 1995] R. A. Young, “The Rietveld method” Internacional union of crystallography, monographs on crystallography 5. Oxford University Press. Oxford. 1995.

[Zheng 2011] H. Zheng, J. Z. Ou, M. S. Strano, R. B. Kaner, A. Mitchell, and K. Kalantar-zadeh, "Nanostructured Tungsten Oxide – Properties, Synthesis, and Applications," Advanced Functional Materials,vol. 21, pp. 2175-2196, 2011.

[Zribi 2009] A. Zribi and J. Fortin, "Functional Thin Films and Nanostructures for Sensors: Synthesis, Physics and Applications," New York: Springer, 2009.

APPENDIX A1

COMPLETE ABSORPTION SPECTRA OF THE WO_3 NANOSTRUCTURES AND THIN FILMS

A1. Complete absorption spectra of the WO_3 nanostructures and thin films

In this appendix, the complete absorption spectra of the different WO_3 thin films and nanostructures studied in this thesis are presented. Since the differences between the spectra of a given thin film or nanostructure for the different gases are very small, the actual sensing is performed on the basis of differential absorption values, taking as reference spectrum that corresponding to Air. However, and for the sake of completeness, the complete absorption spectra are reported here

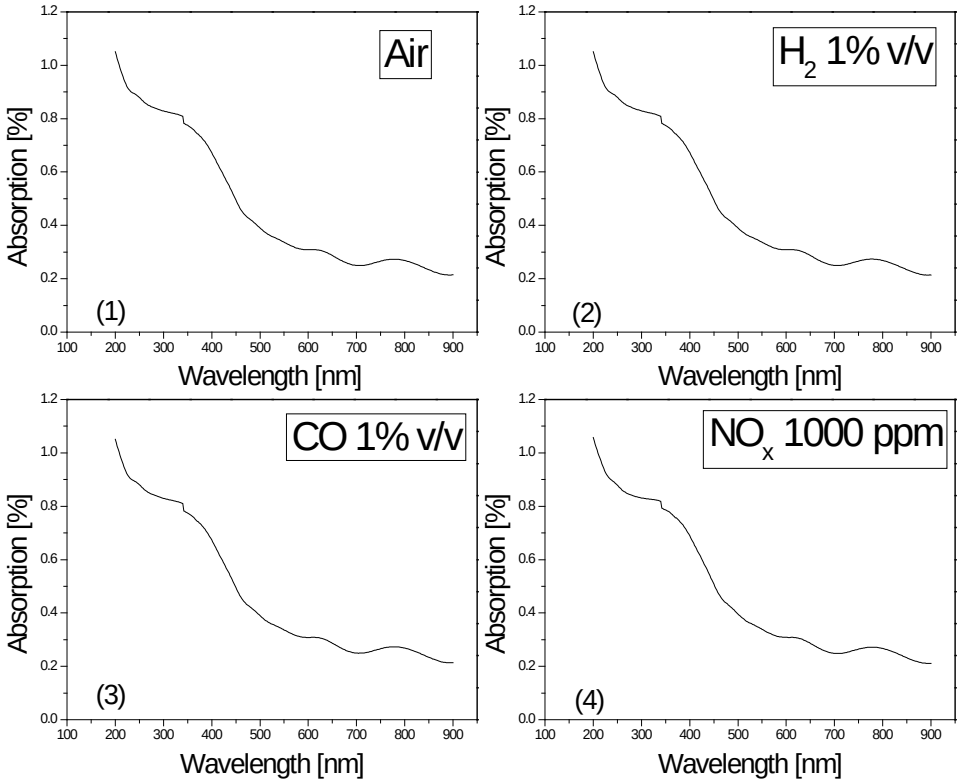

Figure A1.1 Complete absorption spectra of WO_3 thin film samples annealed at 773K for the different gases specified in the graphs and at the operating temperature of 573K.

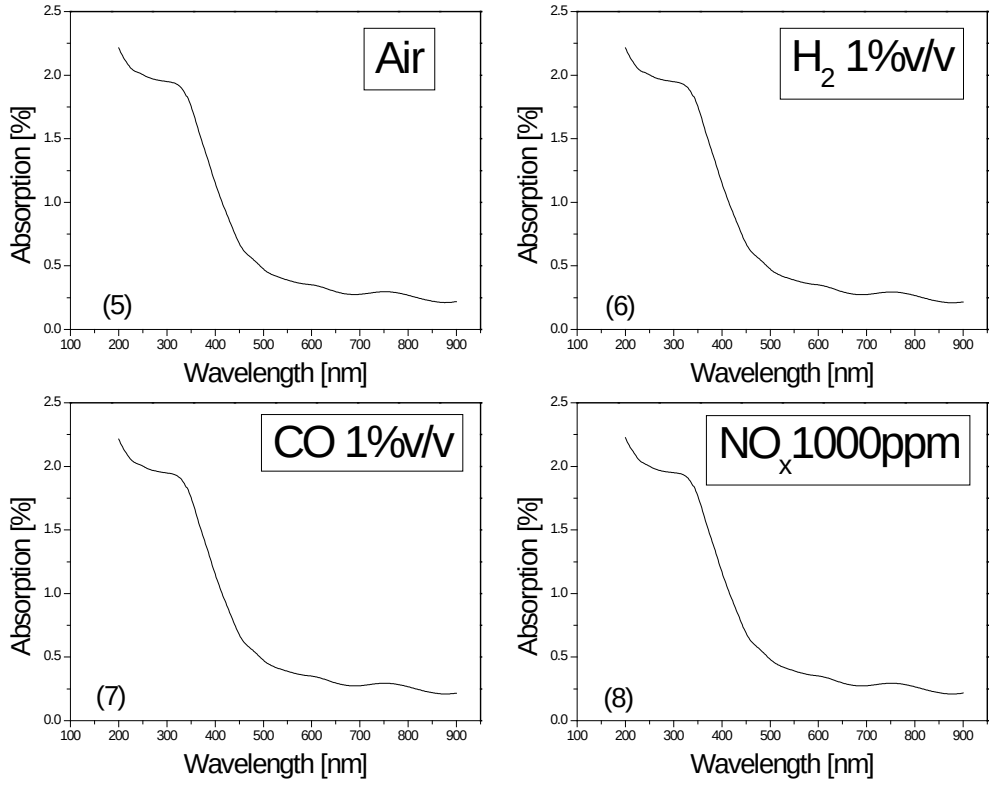

Figure A1.2 Complete absorption spectra of WO_3 thin film samples annealed at 873K for the different gases specified in the graphs and at the operating temperature of 573K.

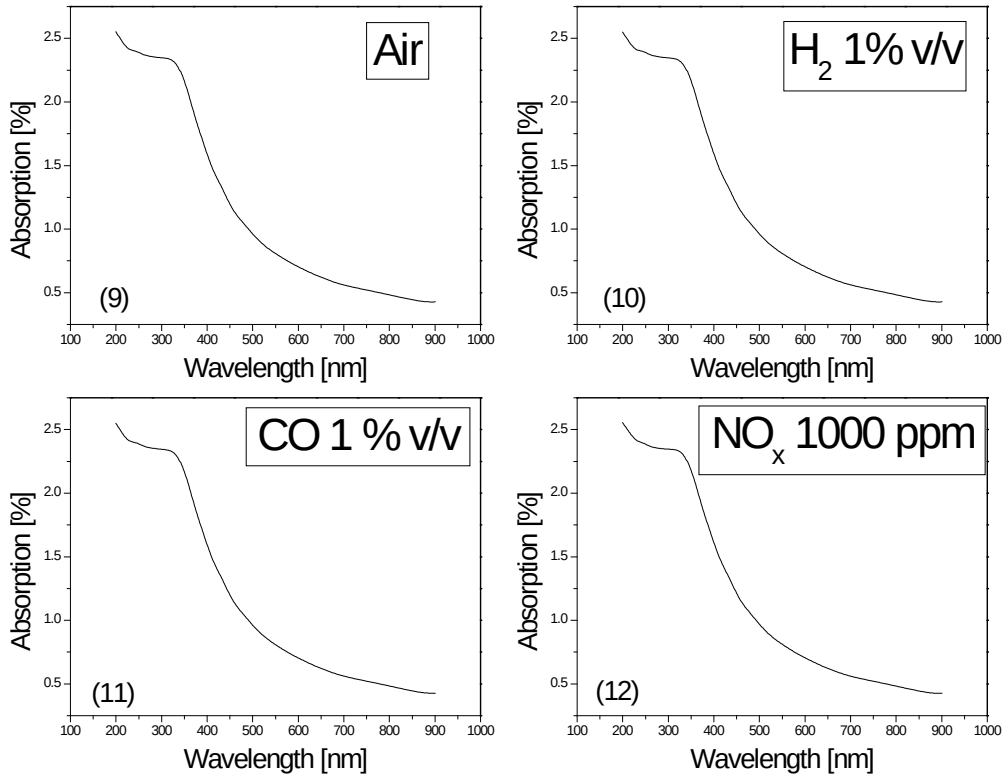

Figure A1.3 Complete absorption spectra of WO_3 thin film samples annealed at 973K for the different gases specified in the graphs.and at the operating temperature of 573K

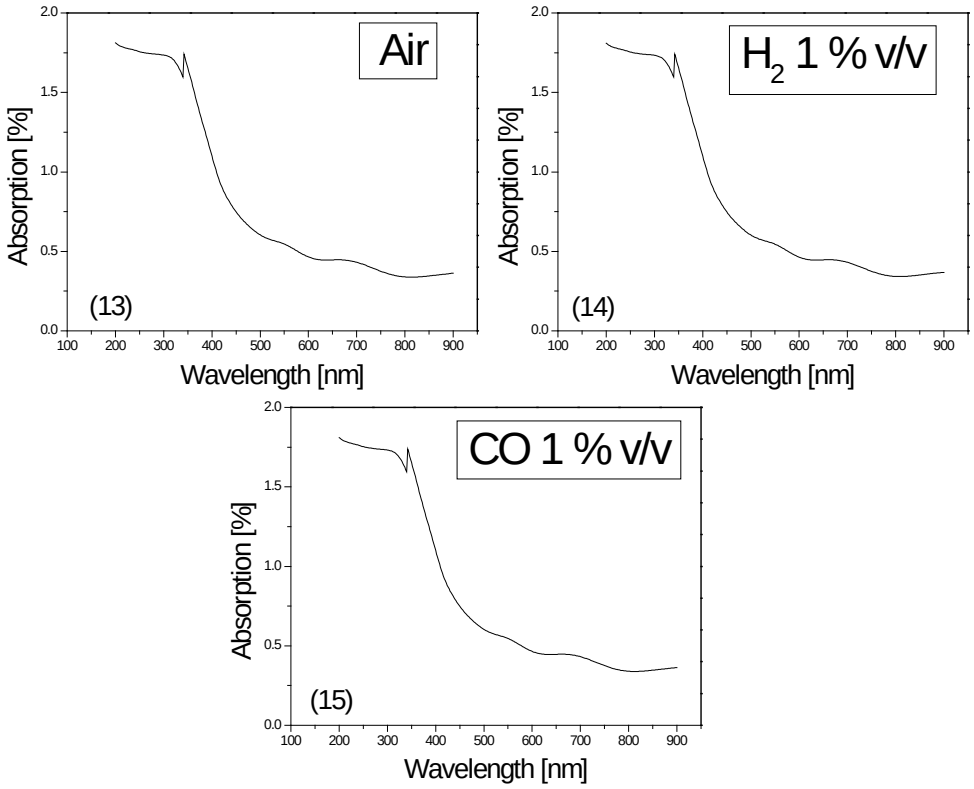

Figure A1.4 Complete absorption spectra Pt/ WO_3 thin films at room temperature for the gases specified in the graphs and operating at room temperature.

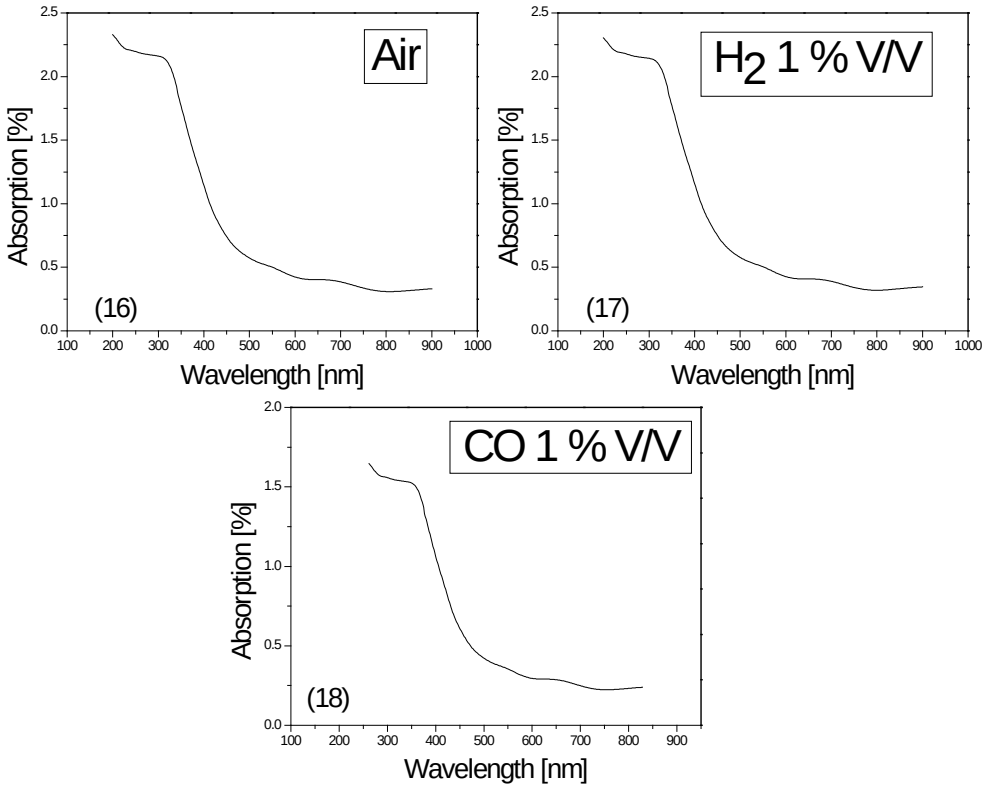

Figure A1.5 Complete absorption spectra Pt/ WO_3 thin films at the operating temperature of 423 K for the gases specified in the graphs.

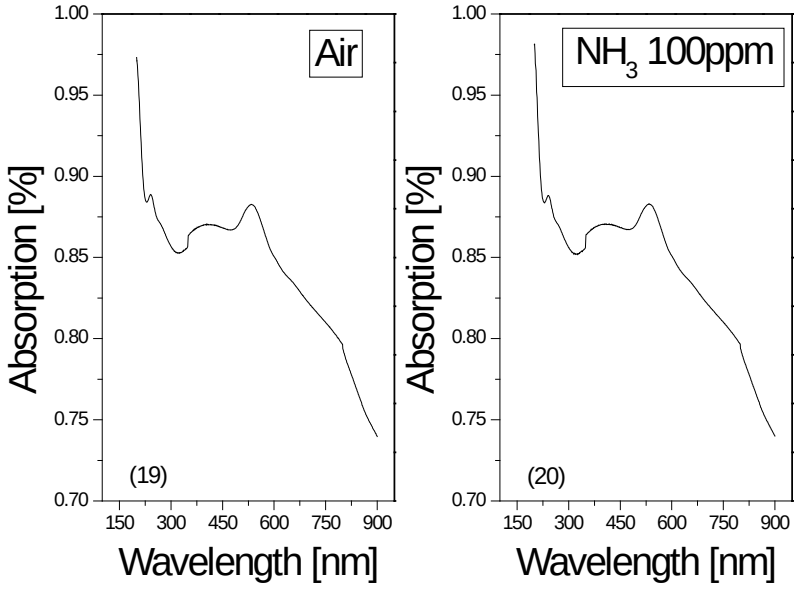

Figure A1.6 Complete absorption spectra of Au/ WO_3 nanoneedles measured at room temperature for the gases specified in the graphs.

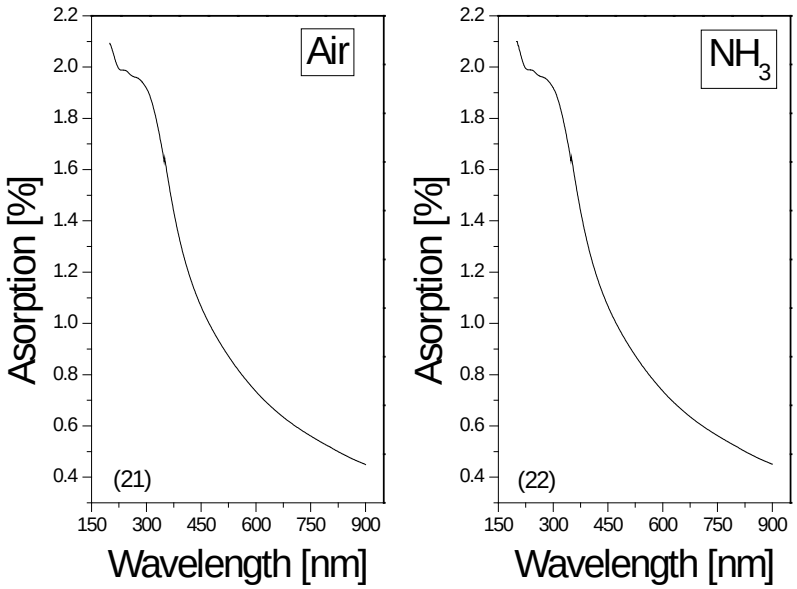

Figure A1.7 Complete absorption spectra Pt/ WO_3 nanoneedles measured at room temperature for the gases specified in the graphs.